IEET
International Electrical Engineering Transactions

Vol. 2 No. 2 (3)
July-December, 2016
ISSN 2465-4256

An online publication of the EEAAT
Electrical Engineering Academic Association (Thailand)
www.journal.eeaat.or.th

IEET – International Electrical Engineering Transactions

This journal is an online publication of the EEAAT, Electrical Engineering Academic Association (Thailand). IEET is published twice a year, ie., the first issue is for January – June and the second issue is for July – December.

IEET (International Electrical Engineering Transactions) is published twice a year. Original contributions covering work in all aspects of electrical science, technology, engineering, and applications will be peer-reviewed by experts before publication. Topics of interest include the following: electrical power, electronics, telecommunication, control and system, sensor and measurement, optical technology, computer, information and communication technology (ICT), signal processing, social network tools and applications (apps), engineering education and other related fields.

For online submission of all manuscripts, correspondences, and letters, please visit
www.journal.eeaat.or.th

IEET Editorial Office

EEAAT - Electrical Engineering Academic Association (Thailand)
Room 409, F-Building,140 Cheum-Sampan Rd.
Nong Chok, Bangkok, Thailand 10530
Tel: +662-988-3655 ext 2216 Fax: +662-988-4026

IEET - International Electrical Engineering Transactions
Volume 2
Number 2 (3)
July – December 2016

PAPERS

A Wideband Printed Log Periodic Dipole Antenna With Series 3/2 Curve Fractal Elements For Wireless Communication System

N. Srisoontorn, C. Mahatthanajatuphat and P. Akkaraekthalin

Manuscript received August, 2016
Revised November, 2016

ABSTRACT

A printed wideband log periodic dipole antenna with series 3/2 curve fractal element is presented, which is responsible to reduce size and wider operating frequency bands. A 3/2 curve fractal geometry has been generated on the dipole element of a log periodic dipole antenna (LPDA) for reducing the electrical length. The antenna dimension is about 127 x 183.29 mm^2 reducing approximately 20% compared with the conventional LPDA. Additionally, the antenna has a wide impedance bandwidth about 135.97%. The radiation patterns are directional at all of operating frequencies and the average peak gain of the antenna is about 4.47 dBi supporting the operating frequency range of 810 MHz - 2690 MHz. The antenna covers the standard of GSM 850, GSM 900, DCS 1800, PCS 1900, UMTS, WLAN IEEE802.11b/g, and 4G (4th Generation Mobile), consequently.

Keywords: *wideband, 3/2 curve fractal element, log - periodic dipole antenna*

1. INTRODUCTION

The front-ends are needed for all mobile communication systems. The antenna is a key part of any front-end of communication systems. It is designed with various shapes or structures. The requirements of antenna design are low profile, low cost, compact size, multiband operation, and etc [1]-[3]. Furthermore, wideband antennas are created for many applications on communication systems using multi-resonance techniques to support the high impedance bandwidth.

There are many antenna types supporting the characteristic of wideband antennas, for instance, wideband slot antennas, wideband monopole antennas, log periodic antennas, and etc. In the literature review [4,5], the wideband slot antennas were achieved by increasing the number of single resonant antennas. The antennas were produced by distributing the magnetic current and electric field along the slot creating nulls closed the feed point and middle-top slot to operate at the first and second resonant frequencies, respectively. Then, the wideband monopole antenna in [6] was designed as the frequency reconfigurable antenna with miniaturized structure achieving multiband operation. This antenna created the dual widebands for LTE/GSM/UMTS standards by combining the spiral monopole and inductive strip line to improve the higher and lower frequency bands, respectively. As the previous reviews, the disadvantage of wideband slot antennas and monopole antennas is low gain characteristic, normally lower than 3 dBi.

The log periodic antennas with directional patterns responding for wide frequency bands were proposed [7]-[9]. The advantages of these antennas were that the numbers of antennas and combiners were reduced as using in the multiple operating frequency bands and the characteristic of high gain was obtained. Several antennas were designed using microstrip and co-planar waveguide structures on a printed circuit board (PCB). A novel wideband log-periodic dipole antenna (LPDA) in [10] was also designed on a printed antenna structure with elliptical dipole for the first element to operate at the lower frequency. Then, the small wideband antenna was proposed by combining the structure of LPDA with the Koch fractal geometry to response wide frequency band [11]. Nevertheless, the antenna sizes of these LPDAs were still large and the frequency bands did not support all wireless communication applications.

In this paper, the printed wideband log periodic dipole antenna with series 3/2 curve fractal elements is presented to operate at the frequency range of 800-4000 MHz covering in many communication systems for instant, GSM 850 (Global system for mobile communication) 824-894 MHz, GSM 900 890-960 MHz, DCS (Digital Communication System) 1710-1880 MHz, PCS (Personal Communication System) 1850-1990 MHz, UMTS (Universal Mobile Telecommunication System) 1920-2170 MHz, WLAN (Wireless Local-Area Network) 2400-2484 MHz, and 4G (4th Generation Mobile) 2500-2690 MHz. Moreover, the proposed antenna is designed using fractal technique and log-periodic antenna structure getting the performance improvement. Therefore, the size of the proposed antenna is reduced by generating the series 3/2 curve fractal geometry based on a typical log periodic

N. Srisoontorn, C. Mahatthanajatuphat and P. Akkaraekthalin are with the Department of Electrical and Computer Engineering, Faculty of Engineering, King Mongkut's Institute of Technology North Bangkok (KMITNB), 1518 Pracharat 1 Rd.,Wongsawang, Bangsue, Bangkok 10520, Thailand.

dipole antenna compared with conventional log periodic dipole antenna.

The antenna parameters will be investigated by using the CST microwave studio. The proposed antenna prototype will be experimented and evaluated. Additionally, the organization of this paper is comprised of the antenna design in section II. Then, the simulation and experiment of the antenna characteristics will be verified in section III. Finally, the results and conclusions for the proposed antenna are discussed in section IV.

directivity as presented in [12]. In this case, the frequency bandwidth from 800 MHz to 2600 MHz and directivity of 7.5 dB are required to design the proposed LPDA.

To determine the frequency bandwidth and directivity, the scaling factor (τ) is a significant parameter relating to the relative spacing (σ) for designing the log periodic antenna [12]. In this paper, the scaling factor (τ) and the relative spacing (σ) are decided to be approximately 0.822 and 0.148, respectively. Also, the dielectric substrate of FR4 with a thickness (*h*) of 1.6 mm, relative permittivity (ε_r) of 4.1, loss tangent of 0.019.

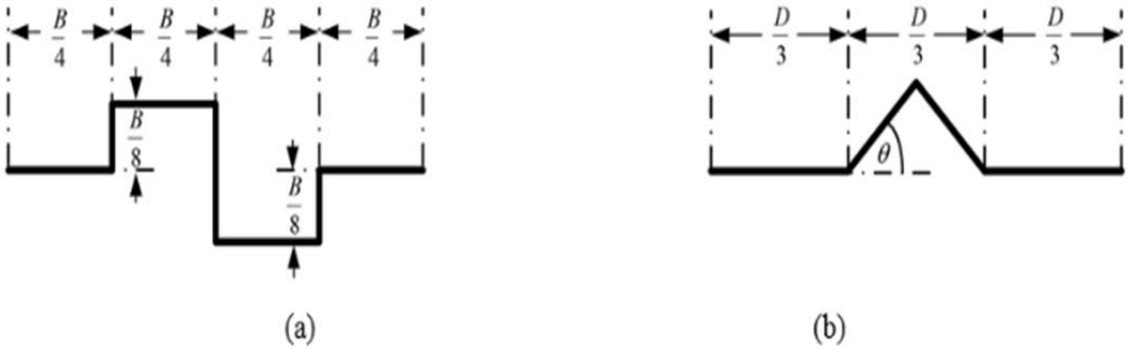

Fig. .1 *The generator models of (a) 2/3curve fractal and (b) Koch fractal geometries.*

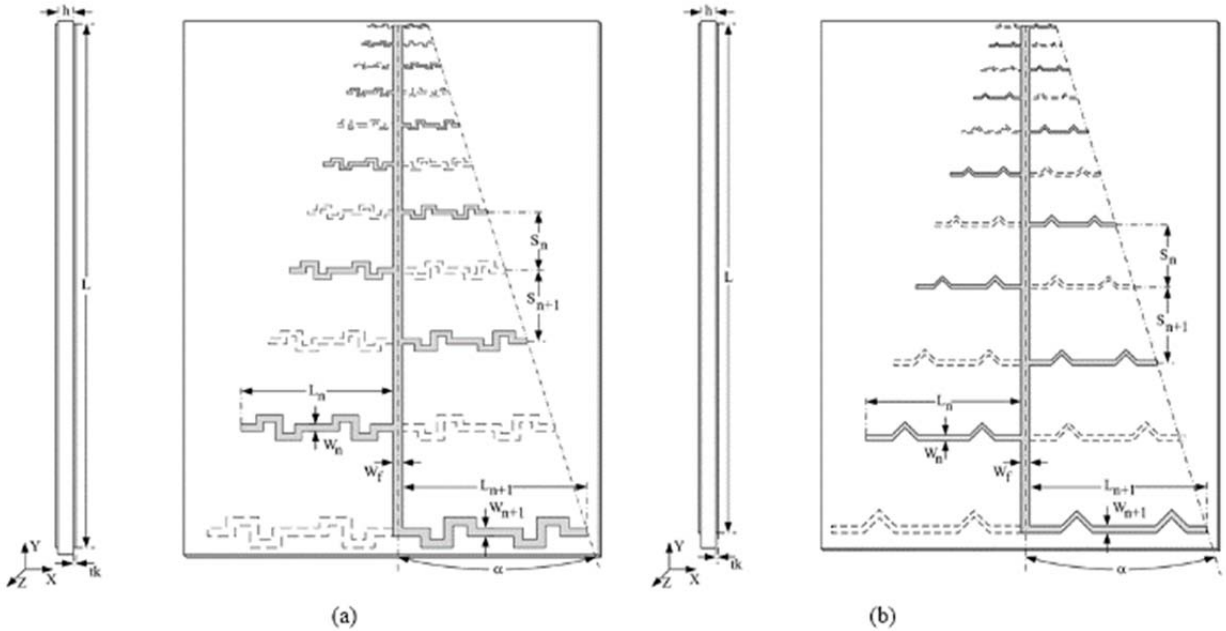

Fig. 2. *Configurations of the LPDA with series of (a) 3/2 curve fractal and (b) Koch fractal geometries.*

2. ANTENNA DESIGN

In this section, design of a wideband printed log periodic dipole array (LPDA) is presented and discussed. The log periodic dipole array composes of several dipole elements, which each one responds to each resonant frequency. The number of dipole elements is defined by the specification of frequency bandwidth and the

Copper thickness of 0.035 mm is used. Additionally, the parallel feeding line has a characteristic impedance Z_0 approximately 50 ohm, which obtains the width W_f = 3 mm.

The number of dipole element is calculated by using the expressions presented in [12]. From the scaling factor (τ) and the relative spacing (σ) as previous selected, the number of dipole elements of N = 11 and the aperture

angle (α) of 16.73º are chosen. The initial length L_n can be obtained by using $L_n = \lambda_g/4 = 70.31$ mm and the width W_n is chosen to be 3 mm. Also, the log period length L_{n+1} can be calculated by

$$L_{n+1} = \tau L_n \quad ; N = 1,..., 11. \tag{1}$$

Moreover, the space Sn = 4σ$Ln+1$ = 41.63 mm is obtained and the log period space S_{n+1} can be calculated by

$$S_{n+1} = \tau S_n \quad ; N = 1,..., 11. \tag{2}$$

Table 1 Geometry of the designed printed LPDA

Dipole elements	Conventional			3/2 curve fractal			Kock fractal		
	L_n [mm]	W_n [mm]	S_n [mm]	L_n [mm]	W_n [mm]	S_n [mm]	L_n [mm]	W_n [mm]	S_n [mm]
1	70.31	3	-	62	3	-	66	2.47	-
2	57.8	2.47	41.63	50.94	2.47	36.97	52.25	2.03	32.33
3	47.51	2.03	34.22	41.89	2.03	30.39	36.66	1.67	26.58
4	39.05	1.67	28.13	34.44	1.67	24.98	44.56	1.37	26.55
5	32.1	1.37	23.12	28.3	1.37	20.53	30.13	1.13	21.82
6	26.39	1.13	19	23.27	1.13	16.88	24.77	0.93	17.94
7	21.69	0.93	15.62	19.13	0.93	13.87	20.36	0.76	14.75
8	17.83	0.76	12.84	15.72	0.76	11.4	16.74	0.63	12.12
9	14.66	0.63	10.55	12.92	0.63	9.37	13.76	0.51	9.96
10	12.05	0.51	8.68	10.62	0.51	7.7	11.3	0.42	8.19
11	9.9	0.42	7.13	8.73	0.42	6.33	9.3	0.35	6.73

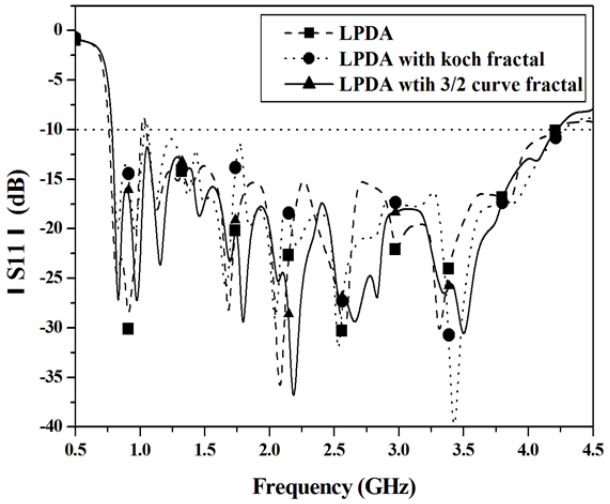

Fig. 3. *Comparison of simulated return losses.*

Furthermore, the parameters of the conventional LPDA are obtained as given in Table 1 for covering the operating frequency between 800 MHz and 2600 MHz. The element number of LPDA is eleven. Therefore, the typical dimension of LPDA is about 143.63 x 202.62 mm^2. Additionally, the typical LPDA will be applied by generating the 3/2 curve model [13] and Koch fractal model [11], as illustrated in Figs.1a and 1b, respectively, on each dipole element of the log periodic antenna. In Fig.1a, the generator model having a length of B is separated into four parts. The height of generator model is approximately 50 percent of a quarter of length B while the length B is a half of L_n. Then, the model will be connected series together to generate on each dipole element of LPDA as called the series 1st iteration of 3/2 curve model and depicted in Fig.2a. Also, in Fig.1b the Koch model having a length of D is divided in 3 parts while the height of Koch model is a half of one-third of length D getting the flare angle θ about 45 degree.

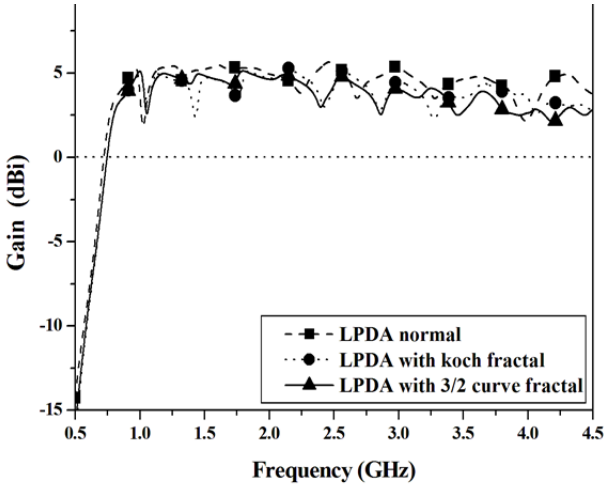

Fig. 4. *Comparison of simulated peak gains at 0 degree.*

Then, the Koch model will be connected in series also as pervious process and shown in Fig.2b.

Especially, the antenna characteristic of the presented antenna will be investigated and compared to the LPDA with series Koch fractal model as proposed in [14]. In this paper, the LDPA with series Koch fractal having the typically 45 degree flare angle and the LDPA with series 1st iteration of 3/2 curve fractal are designed to support the frequency bandwidth of 800 - 2600 MHz. The

characteristics of impedance bandwidth and gain will be simulated and measured.

Two antennas, the LPDA with series Koch fractal and LPDA with series 3/2 curve fractal, are designed on an FR4 substrate with a thickness (h) of 1.6 mm, relative permittivity (ε_r) of 4.1, loss tangent of 0.019, copper thickness of 0.035 mm. These antennas have dimensions of 135x178.17 mm^2 and 127x183.29 mm^2, respectively. All parameter details are illustrated in Fig. 2 and Table 1.

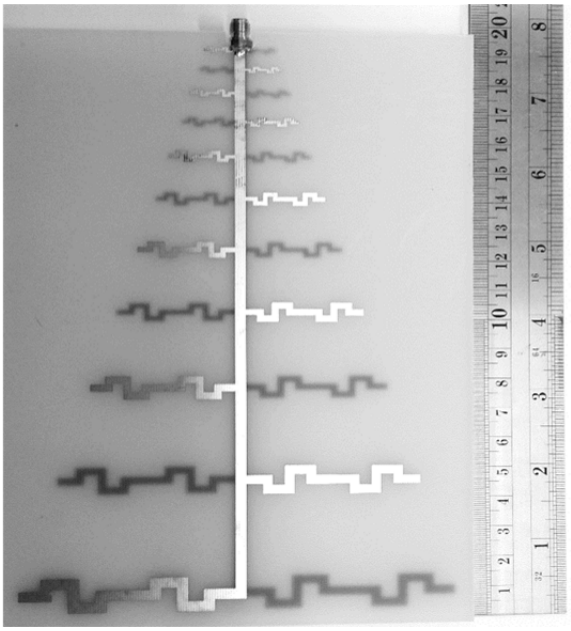

Fig. 5. *Prototype of the fabricated antenna.*

3. SIMULATION AND EXPERIMENTAL RESULTS

The simulated return losses and gains of the conventional LPDA, LPDA with series 3/2 curve fractal, and LPDA with series Koch fractal are compared as depicted in Figs. 3 and 4, respectively. In Fig. 3, it can be clearly seen that the S_{11} level of LPDA with series 3/2 curve fractal is less than -10 dB in the operating frequency band between 785 MHz to 4221 MHz as the other antennas have the S_{11} level higher than -10 dB at the neighborhood frequency of 1.1 GHz. As the results, the dimension of LPDA with series 3/2 curve fractal geometry has been reduced about 20% as compared with the conventional LPDA. Also, the dimension of the LPDA with series Koch fractal geometry can be reduced about 17% as compared with the conventional LPDA. As shown in Fig.4, it has been found that the simulated gains of the LPDA, LPDA with 3/2 curve fractal geometry and LPDA with Koch fractal geometry are approximately 5 dBi at the operating frequency band. The simulated and measured results of presented antenna will be investigated and discussed in the next section.

Because of its more compact size, only the LPDA with series of 3/2 curve fractal was fabricated by chemical process as shown in Fig. 5. As the results in Fig. 6, the simulated and measured S11 results of the proposed antenna are agree well. Obviously, the return loss of measured result is more than -10 dB and can cover the impedance bandwidth between 810 MHz to 4250 MHz to support the applications of wireless mobile communication systems. Additionally, the measured impedance bandwidth of the antenna is 135.97%. However, the dissimilar results between simulation and measurement are caused by the coupling between the SMA connector at the fed port and the radiated element of antenna, affecting to the electromagnetic field of the antenna.

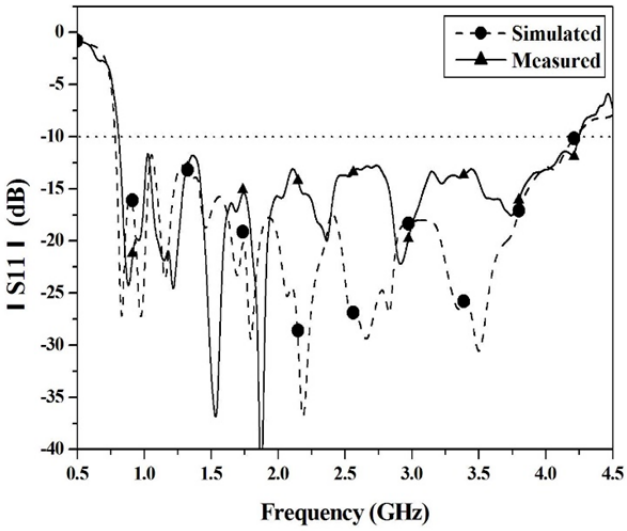

Fig. 6*. Simulated and measured return losses of the proposed antenna.*

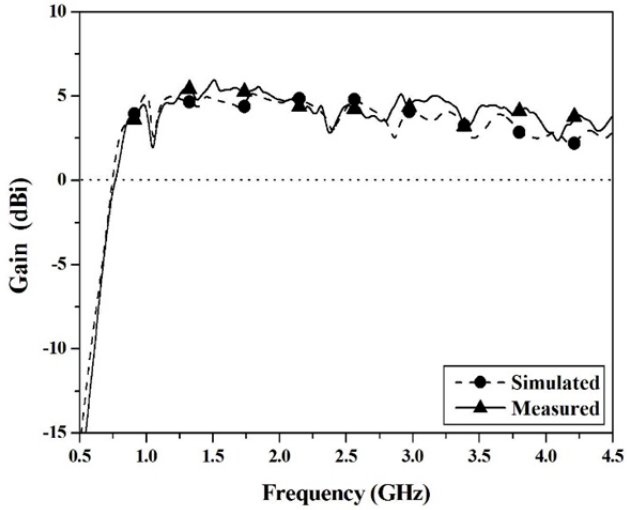

Fig. 7. *Simulated and measured peak gains at 0 degrees of the proposed antenna.*

Also, the antenna gains of simulated and measured results are slightly different due to the previous reasons. Furthermore, the average of measured antenna gain is approximately 5 dBi, as shown in Fig. 7. Moreover, the current distribution has been evaluated as shown in Fig. 8. It can be clearly seen that the 1st and 2nd elements are the main elements to radiate electromagnetic field at the operating frequency of 850 MHz and 900 MHz, respectively. However, the 5th to 11th elements

significantly radiate electromagnetic field at the operating frequency from 1800 MHz to 2600 MHz. Additionally, the radiation patterns of the proposed antenna are directional in XY-planes and YZ-planes at all operating frequencies with F/B ratio above 10 dB, as illustrated in Fig. 9. The peak gains at all of operating frequencies of the antenna are at about 0 degree.

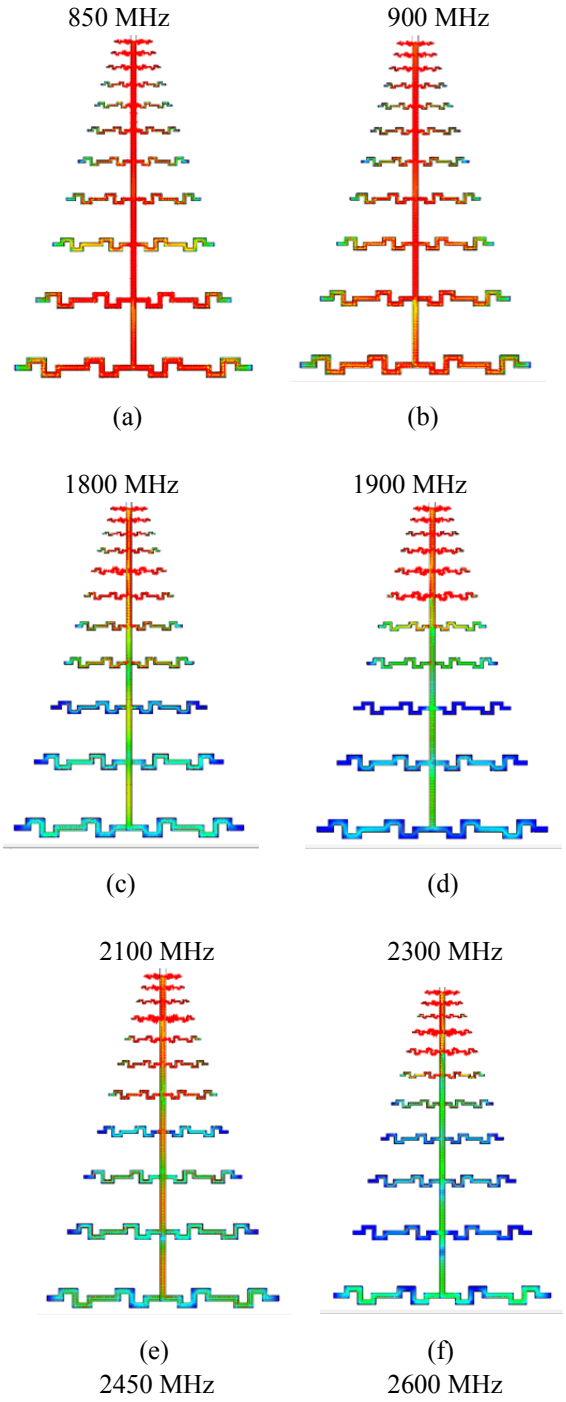

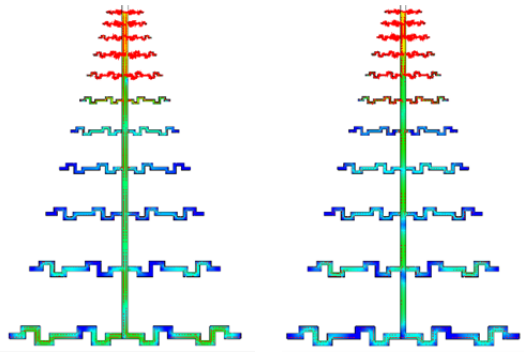

Fig. 8 *Simulated results of the surface current distribution on the LPDA with series 3/2 curve fractal at (a) 850 MHz, (b) 900 MHz, (c) 1800 MHz, (d) 1900 MHz, (e) 2100 MHz, (f) 2300 MHz, (g) 2450 MHz, and (h) 2600 MHz.*

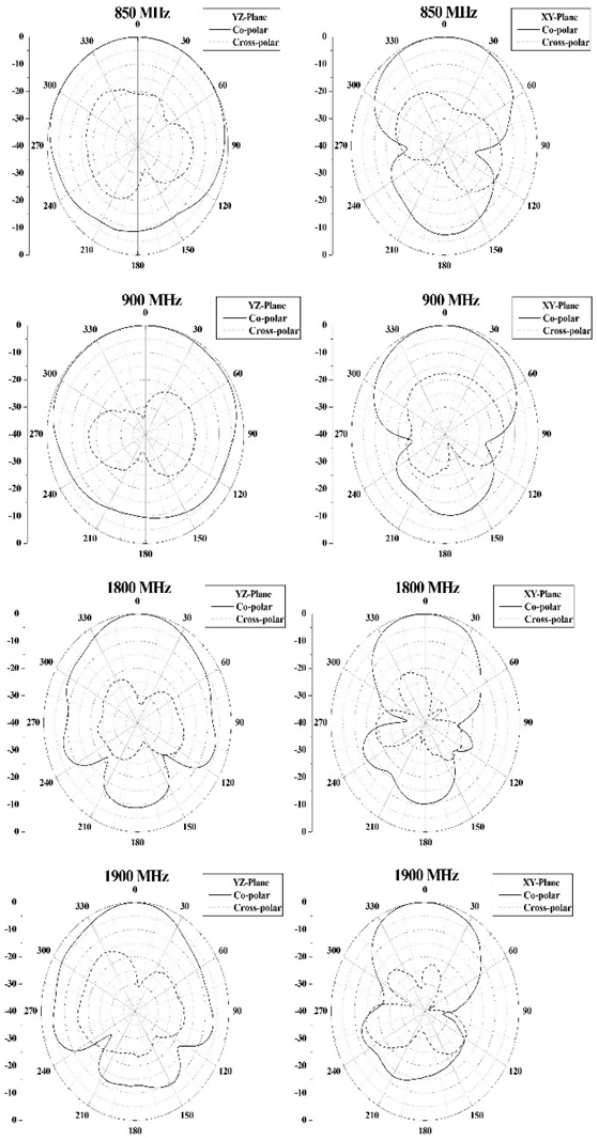

Fig. 9 *Measured radiation patterns of the presented antenna at the resonant frequencies of 850 MHz, 900 MHz, 1800 MHz, 1900 MHz, 2100 MHz, 2300 MHz, 2450 MHz, and 2600 MHz in YZ-planes and XY-planes.*

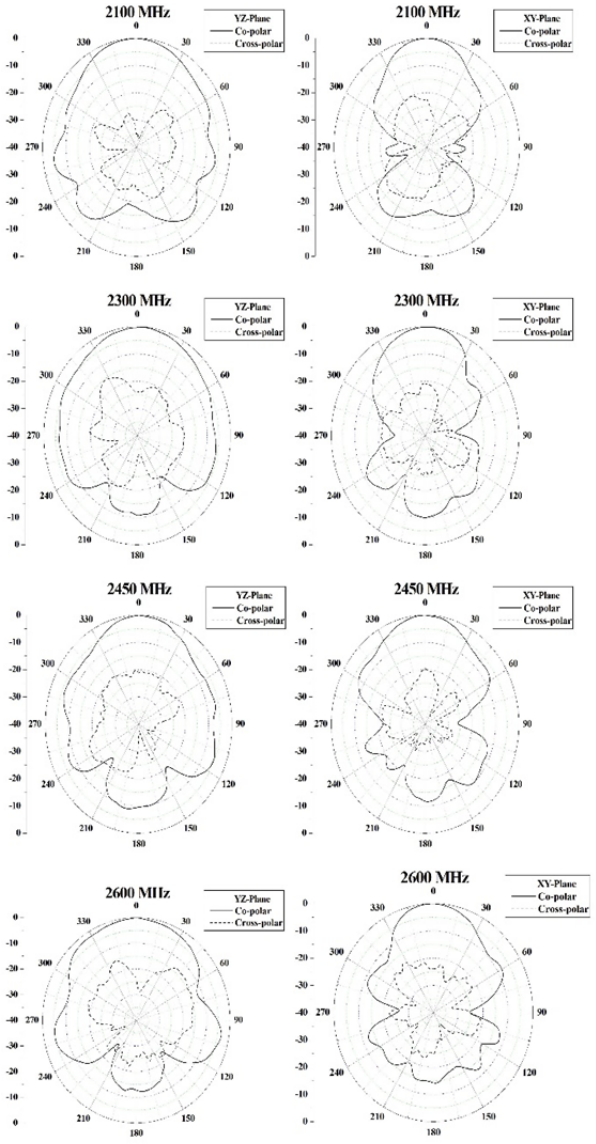

Fig. 9(Cont.) *Measured radiation patterns of the presented antenna at the resonant frequencies of 850 MHz, 900 MHz, 1800 MHz, 1900 MHz, 2100 MHz, 2300 MHz, 2450 MHz, and 2600 MHz in YZ-planes and XY-planes.*

4. CONCLUSION

The printed wideband log periodic dipole antenna with series 3/2 curve fractal elements has been presented. It is accomplished wider impedance bandwidth supporting the operation frequencies for applications in GSM 850 (Global system for mobile communication) 824-894 MHz, GSM 900 890-960 MHz, DCS (Digital Communication System) 1710-1880 MHz, PCS (Personal Communication System) 1850-1990 MHz, UMTS (Universal Mobile Telecommunication System) 1920-2170 MHz, WLAN (Wireless Local-Area Network) 2400-2484 MHz, and 4G (4th Generation Mobile) 2500-2690 MHz. Additionally, the antenna with series 3/2 curve fracatal geometry has a very compact size which the dimension can be reduced about 20% compared with the conventional log periodic dipole antenna (LPDA). Moreover, the operating bands have independent radiations concerned by the each fractal dipole element of the LPDA. Furthermore, the radiation patterns are directional at all operating frequency bands. The average gain of the proposed antenna is approximately 5 dBi.

ACKNOWLEDGMENT

The authors would like to thank the Thailand Research Fund (TRF) under senior research fund (RTA-5780010) for the research grant support.

REFERENCES

[1]. Cecep G. P., Achmad M. : " Printed Multiband Antenna for Mobile and Wireless Communications", International Conference on Telecommunication Systems, Services, and Applications (6th TSSA 2011), Vol. 14, pp. 236-240 (2011).

[2]. Sheng-Bing C., Yong-Chang J., Wei W., Fu-Shun Z. : "Modified T-Shaped Planar Monopole Antennas for Multiband Opertion", IEEE Transactions on Microwave Theory and Techniques, Vol. 54, No.8, pp. 3267-3230 (2006).

[3]. Chatree M., Norakamon W., Prayoot A. : "A Multiband Monopole Antenna with Modified Fractal Loop Parasitic for DCS 1800, WLAN, WiMAX and IMT Advanced Systems", IEICE Transactions on Communications, Vol. e95-B, No. 1, pp. 27 - 33 (2012).

[4]. Bhobe, A.U.; Holloway, C.L.; Piket-May, M.; Hall, R. : "Coplanar waveguide fed wideband slot antenna", Electronics Letters, Vol. 36 , No. 16, pp. 1340-1342 (2000).

[5]. Behdad, N.; Sarabandi, K. : "A multiresonant single-element wideband slot antenna", IEEE Antennas and Wireless Propagation Letters, Vol. 3 , No. 1, pp. 5-8 (2004).

[6]. Gyeong-Ho K., Tac-Yeoul Y. : "Small Wideband Monopole Antenna With a Distributed Inductive Strip for LTE/GSM/UMTS", IEEE Transactions Antennas and Propagation, Vol.63, No. 3, pp. 901 – 908 (2015).

[7]. Barbano N. : "Log periodic Yagi-Uda array", IEEE Transactions Antennas and Propagation, Vol. 14, No. 2, pp. 235-238 (1966).

[8]. Mruk J.R., Kefauver W.N., Filipovic D.S. : "Band Rejection Methods for Planar Log-Periodic Antennas", IEEE Transactions Antennas and Propagation, Vol. 58, No. 7, pp. 2288-2294 (2010).

[9]. Abdo-Sanchez E., Esteban J., Martin-Guerrero T.M., Camacho-Penalosa C., Hall P.S. : "A Novel Planar Log-Periodic Array Based on the Wideband Complementary Strip-Slot Element", IEEE Transactions Antennas and Propagation, Vol. 62, No. 11, pp. 5572-5580 (2014).

[10]. Yuanqing Z., Jinghui Q. : "A Novel Wide Band Log-Periodic Dipole Antenna", International Conference Signal Processing, Communication and Computing (ICSPCC), Vol. 2, pp: 1- 3 (2013).

[11]. Dimitris E. A., John P., Manos M. T., Christos G. C. : "A Printed Log-Periodic Koch-Dipole Array

(LPKDA)", IEEE Antennas and Wireless Propagation Letters, Vol.7, pp : 456 - 460 (2008).
[12]. Balanis, C. A. : Antenna Theory: Analysis and Design, 2nd edition, John Wiley and Sons, New York (1997).
[13]. Sadat S., Fardis M., Dadashzadeh G.-H., Baee R.K. : "Proximity-Coupled Microstrip Patch Antenna Miniaturization Using New Fractal Geometry", Antennas and Propagation Society International Symposium, Vol. 3A, pp: 262 – 265 (2005).
[14]. M. N. A. Karim, M. K. A. Rahim, H. A. Majid, O. Ayop M. Abu and F. Zubir : "Log Periodic Fractal Koch Antenna for UHF Band Applications", Progress In Electromagnetics Research, Vol. 100, pp : 201 - 218 (2010).

DC Fault Analysis and Protection in MTDC Grid-based Hybrid AC/DC Networks

A. Musa, A. Monti and M. Uzair Khurshid

Manuscript received August, 2016
Revised November, 2016

ABSTRACT

As DC faults represent the main obstacle in multi-terminal DC (MTDC) grids, effective protection scheme is proposed for MTDC grid connected within hybrid AC/DC network. This scheme uses fast commutation DC breaker, which is placed on the terminals of each line within MTDC grid, and operates based on local information from the respective converter station. The aim is to provide a selective DC protection scheme that isolates the faulted section and maintain uninterruptable operation in the healthy parts, thus avoid de-energize and energize the entire MTDC grid. Fault analysis is performed under different scenarios. This in turn, serves to validate system capabilities in terms of secure and reliable operation, and study AC- DC fault propagation and influence on overall hybrid AC/DC network dynamic behavior and performance. To this aim, the system model is tested and simulated in real time digital simulator (RTDS).

Keywords: *DC fault protection, fault analysis, MTDC grid, offshore wind farm.*

1. INTRODUCTION

The rapid increase in electricity consumption all over the world is pushing the high voltage alternating current (HVAC) grid to operate close to its limits. In addition to that, the incessant increase in wind energy penetration is presenting new challenges with the presence of HVAC grid. In this new scenario, the idea of high voltage direct current (HVDC) grid is emerging to provide a backbone to the existing AC networks and to facilitate the integration of bulk amount of on-offshore renewable energy. Furthermore, HVDC systems firewall the offshore energy sources from the mainland AC network, and have efficient power delivery due to lower energy losses comparing with HVAC systems. All these advantages have led HVDC systems undergo to significant developments in grid configuration and its switchgear [1].

Among the recent technologies used in HVDC systems, modular multi-level converter (MMC) has received the major attention due to its advantages represented by: modular design, low-frequency modulation, low total harmonic distortion, excellent output waveform and high efficiency and scalability [2].

The majority of the presently operational HVDC links are point to point with two points of connection with AC networks. However, it is envisaged that HVDC network embedding more than two terminal converter stations, which are commonly referred to as multi terminal direct current (MTDC) grids, would offer the possibility of meshed subsea interconnections between countries and continents to share the diversity in renewable energy portfolio for better supply reliability. MTCD grids have several advantages over a multiple point to point DC links, such as: a failure in point to point HVDC link would lead to power outage that supposed to be delivered to AC grid, which might have a significant impact on system stability depending on the amount of power loss, while in case of MTDC grids, power delivery to AC grid is not effected as the former has other alternative paths which improve system reliability and operation performance. Another advantage is the grid maintenance becomes easier for system operators since MTDC grids allow power flow among different converters [3].

However, the transition from point-to-point DC links to MTDC transmission grid for offshore wind farms (OWFs) applications requires proper analysis and investigation under normal and fault conditions to study grid capability in terms of efficient power delivery as well as fault clearance, and to reveal the dynamic influence, under fault conditions, from AC to DC side and vice versa. There are several works have been done in this direction. In [4], the authors target MTDC grid with three terminals to study its dynamic performance under different AC fault conditions. Whereas, three temporary AC fault scenarios was considered and simulated for 5 cycles to study the resulting influence to the MTDC grid. The results concluded that the proposed MTDC grid was able to recover stable operation after fault clearance. The authors proposed for future work to integrate their proposed system for wind power delivery. While, in [5] the authors proposed DC fault management scheme called Delayed Auto-Re-Configuration (DARC) for fault isolation and system recovery in MTDC grid including four MMC stations connecting four ideal sources as AC grids. The proposed DARC scheme uses AC breakers and DC isolation switches and operates as follow: in case of DC fault condition, all the converters will block their operation and a trip signal will be sent to all the AC breakers to isolate the entire MTDC grid, then the relevant DC switches will isolate the faulted section. For system recovery, AC breakers will close for standby status, then a sequential de-blocking process for the

A. Musa, A. Monti is with the Institute for Automation of Complex Power System RWTH Aachen University
Aachen, Germany. Mail: amusa,amonti@eonerc.rwth-aachen.de
M. Uzair Khurshid is with the Sirindhorn International Thai-German Graduate School of Engineering (TGGS) King Mongkut's University of Technology North Bangkok Bangkok, Thailand. Mail : muhammad-u-epe2013@tggs-bangkok.org

converters will be done based on each converter's control mode to achieve stable system energizing. Another work has used electromechanical transient MMC-MTDC grid models with two control strategies, DC voltage margin control and DC voltage droop control. Then, stability analysis of two asynchronous AC systems interfaced with MTDC grid has been studied to investigate AC fault propagation between the AC grids. The results demonstrate that both control strategies are able to control DC voltage during transients, and AC fault is well isolated in the MTDC grid connected-asynchronous AC systems [6].

In this work, hybrid AC/DC system has been modelled and studied to include MMC-MTDC grid connecting two onshore AC grids with two offshore wind farms (OWFs). Besides, effective protection scheme is used based on force current commutation DC breakers with over current and under voltage protection relays, which is able to isolate the faulted section within few milliseconds and maintain uninterruptible operation in the rest of the system, thus achieve optimal operation of MTDC grid under fault conditions. A realistic model of onshore AC grids is used to include synchronous generators and dynamic loads to study their dynamic behavior and how they react according to AC and DC fault propagation. Extensive fault analysis is performed including AC and DC fault scenarios to test and validate the MTDC grid dynamic performance with its control and protection capabilities in terms of stable and secure operation, and to study fault propagation influence on the synchronous generations, loads and overall system power flow. The objective of this work is to provide an effective protection scheme that contribute with secure and reliable operation of MTDC grid, under different fault conditions, for offshore wind power delivery. Also, it gives an effective framework to study fault analysis and management in hybrid AC/DC network in real-time platform.

This paper has been organized as follow: Section I gives an introduction with literature review on the challenges and state of the art solutions for MTDC grids protection. Section II define hybrid AC/DC network configuration, including MTDC grid. In section III, the proposed protection scheme is provided. Fault analysis and test scenarios are conducted in Section IV. Discussion and conclusion are provided in Section V and VI, respectively.

2 SYSTEM CONFIGURATION

Hybrid AC/DC system has been modeled to include OWFs, MT-HVDC and AC grids and modelled as follow:

A. Multi-Terminal HVDC Grid

Meshed monopolar MTDC grid topology is modeled to include four terminals with four converter stations. In this work, half bridge-MMC is used due to its significant advantages represented by: high efficiency, power quality, redundancy and failure management. The converter comprises of IGBT modules with anti-parallel diodes, facilitating the two-way exchange of power. Further details about MMC characteristics and performance are provided in [7],[8]. As shown in Figure 1, each converter station has the following main components:

1. Converter transformer
2. Start-up current limiting resistor (bypass resistor)
3. Phase reactor
4. Modular Multilevel Converter (MMC)
5. DC line

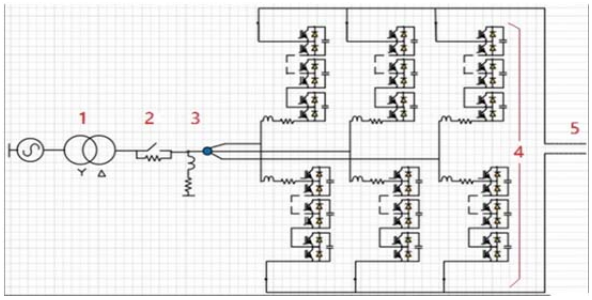

Fig. 1 *Main components of HVDC converter station*

B. MTDC Grid Control

The DC voltage control is important to maintain stable and reliable operation with balance power share. However, the control structure of MMC is composed of three levels: station control which defines the set points and reference values of overall system, and pole control which constitutes upper and lower level controls

1) Station Control: It functions to optimize overall MTDC grid performance by managing the operating set points, e.g. V_{dc} and V_{ac}, and converters control modes to meet both AC and DC system requirements.

2) Upper Level Control: it includes inner current controller (ICC) and outer controller. The first evaluates the voltage drop across the phase reactor to produce the necessary AC current within the converter rating limits. While, the outer controller is based on active and reactive power control categories. Note that every converter can operate with only one category, P and V_{dc} or Q and V_{ac}, depending on grid configuration and system specifications. Also, all of the implemented controllers employ a proportional-integral (*PI*) regulator to achieve zero steady-state error as shown in Figure 2-a.

3) Lower level control: it comprises modulation technique, current suppression and voltage capacitance balancing. Nearest Level Modulation (NLC) technique has been used in this model [2], [9]. More details of MMC control structure is provided in [2].

Note that different DC voltage control schemes could be used in the upper level control. In this work, voltage droop control is used, which represents an effective control strategy used to stabilize DC grid voltage, through a distributed V_{dc} control in several converters. The VDC acts to adapt power injection of converters and regulate their V_{dc} based on droop characteristic shown in Figure 2-b [10].

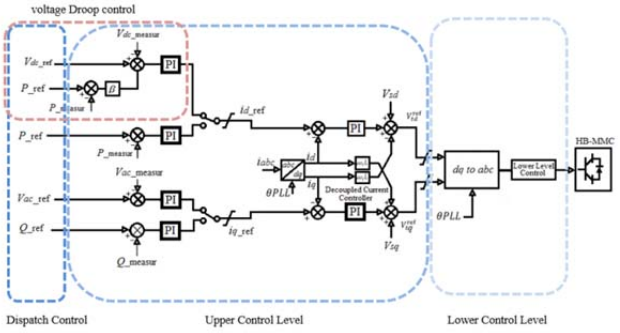

(a)

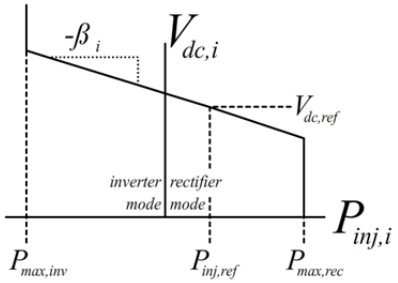

(b)

Fig. 2 *a) MMC control structure. b) voltage droop control*

C. AC grids and Offshore wind farms

Western Systems Coordinating Council (WSCC) power system is used for both AC grid 1&2. Each one composed of 3 generators and 9-buses. Note that both WFs are modelled as a power injection, and are considered delivering their rated power generation. Overall hybrid AC/DC network is modelled as shown in figure 3.

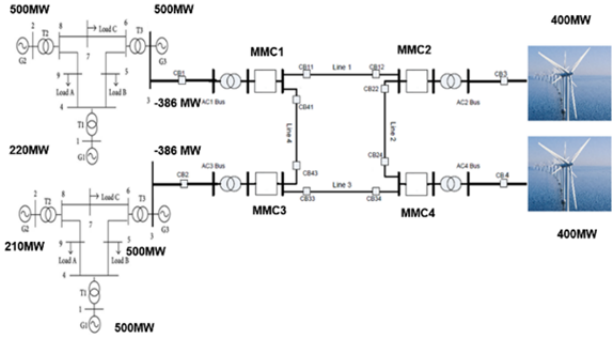

Fig. 3 *MTDC grid-based hybrid AC/DC network*

3 DC FAULT PROTECTION IN MTDC GRID

Reliable operation of the MTDC grids requires effective dc fault protection that able to interrupt dc fault current within few milliseconds and maintain secure operation in the healthy part of the system. The faster fault current interruption the more stable operation and less fault propagation influence to the interconnected AC and DC systems. Another challenge to be discussed in hybrid AC/DC system is fault propagation from AC to DC side and vice versa, that needs to be clarified before discussing the protection scheme.

A. Fault Propagation in AC/DC System

In case of DC fault, large current, *Ic*, will propagate from AC to DC side to feed the fault, resulting high current value lead to block the converter IGBTs due to its internal protection. Nevertheless, this will stop feeding the fault with *Ic*, the AC side is still feeding the fault with *Id* through the freewheeling diodes as depict in Figure 4. This will affect the AC and DC sides and may lead to overall system outage, in case of permanent DC fault, unless protection devices are used.

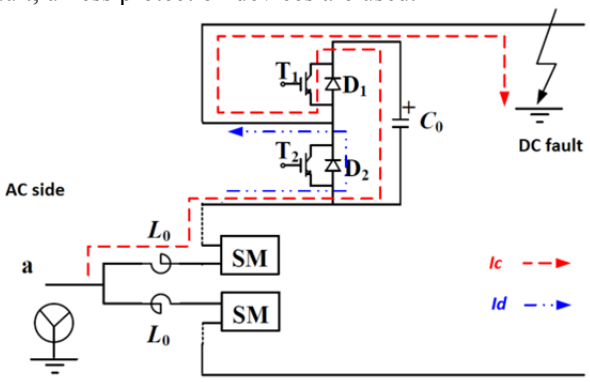

Fig. 4 *Fault propagation from AC to DC side in case of DC fault*

The use of AC breakers by an approach called handshaking method could protect the AC system from DC fault, but will cause complete de-energization of MTDC grid which leads to a temporary loss of bulk power transfer [5]. However, this is not recommended for HVDC systems as they are integrated to realise a reliable and uninterruptable power delivery to the AC systems. Thus, DC fault must be locally isolated to maintain power flow in the rest of MTDC grid. This is achieved by using DC breakers as shown later.

B. Proposed Protection Scheme

An effective scheme has been used for DC fault protection. This scheme uses local measurements at each station terminal. Thus, no communication means are necessary, which avoid communication failure, uncertainties and reduces overall setup cost. Forced current commutation DC breaker is used to be connected at both ends of each DC line. Also, AC breakers are used to achieve AC fault protection and they are connected on the AC sides of MTDC grid as shown in Figure 3. Note that the operating time of both AC and DC breakers is used based on their practical operation to have 5*msec* and 40*msec*, respectively [2], [11].

The protection scheme is described as follow: each converter monitors the current and voltage at its terminals. The identification of the faulty line is based on the difference between pre-fault and the post fault measurements at each station. When a fault occurs, the currents from each station are redirected towards the fault point. Based on this observation, the selection of the DC breaker that need to be opened will be determined. As soon as fault is detected, the relevant

converters will be blocked due to their internal protection.

Based on the comparison of MMCs measurements, each of them need to select a DC breaker to switch off and isolate the fault, which corresponds to the potential faulty line. The selection principle is that the DC breaker at each converter terminal which carries the largest positive current is selected to be opened. As soon as the DC breakers open, the fault currents will extinguish from the grid. The faulty section gets de-energized and the rest of MTDC grid will continue with uninterruptable power flow. It is worth to mention that this protection scheme has a fast, selective and accurate DC fault clearance with maintaining uninterruptable operation in other healthy parts in the system. This is in contrast with the aforementioned methods utilized in the literature. The protection capabilities and performance are tested and validated in the next Section.

4 SIMULATION RESULTS

The overall AC/DC system including MTDC grid has been modelled in real time digital simulator (RTDS) using its graphical user interface RSCAD. The model requires four racks, and each rack consists of 2 GPC cards with four 750GX RISC processors. All MMCs stations are modelled inside a four separate small time-step sub-networks with a time step of 1.4μsec. All small time step sub-networks are interfaced with the large time step interconnected AC system through a small dt /large dt interface block. On the DC side of the MMCs stations, the small time-step sub-networks are connected to each other through travelling wave models of transmission lines. As shown in Figure 4, MMC1 and MMC3 are operate as inverters and connected to both onshore AC grids, while MMC2 and MMC4 are operate as rectifier and connected to both OWFs side. Note that MMC1 and MMC3 operate to maintain DC voltage to a reference value, while MMC 2 and MMC4 operate in power control mode. In this system, AC grid1 and AC grid2 have total generation of 1320MW and 1280MW with load demand equal 1600MW and 1650MW, respectively. The rated capacity of OWF1 and OWF2 are 300 and 400 MW, respectively. The DC cables used are XLPE with 200 km for each line. The AC voltage level for AC grids and OWFs are 380 KV and 145 KV respectively, and the DC links voltage is +/- 200 KV. In this study, the time frame is chosen in second, and two different time spans have been used to capture clearly post-fault system transient behavior in both AC and DC sides.

A. Three phase AC fault scenario

Three phase temporary fault has been applied at 1.6 sec on the AC side of MMC1. In this scenario, the fault is propagating for a short time to the neighbour onshore grids as well as MTDC grid causing power oscillation as shown in Figure 5.

The sequence of each figure is kept in all the fault scenarios, in which: a. active power of synchronous machines in both AC grids, b. loads active power in each AC grid, c. frequency response in AC grids and OWFs, d. shows the active power in each converter, e and f are the DC voltage and current of each converter.

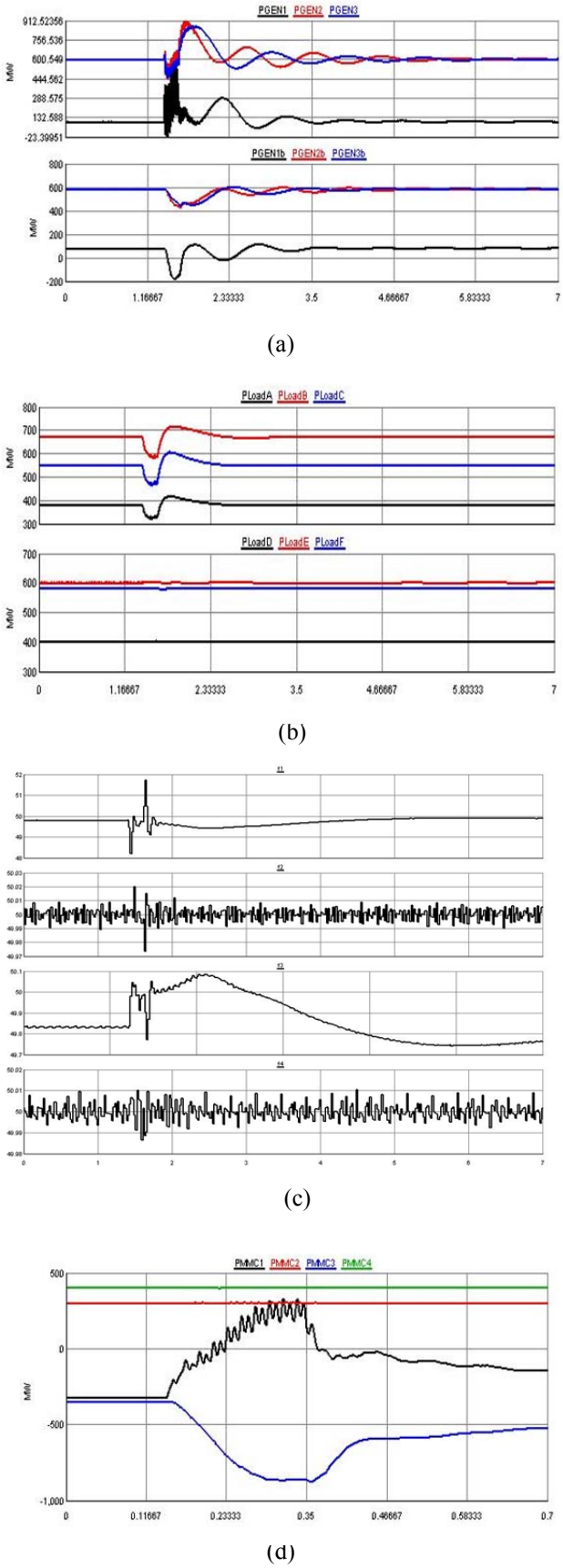

Fig. 5 *Three phase fault at MMC1 AC side*

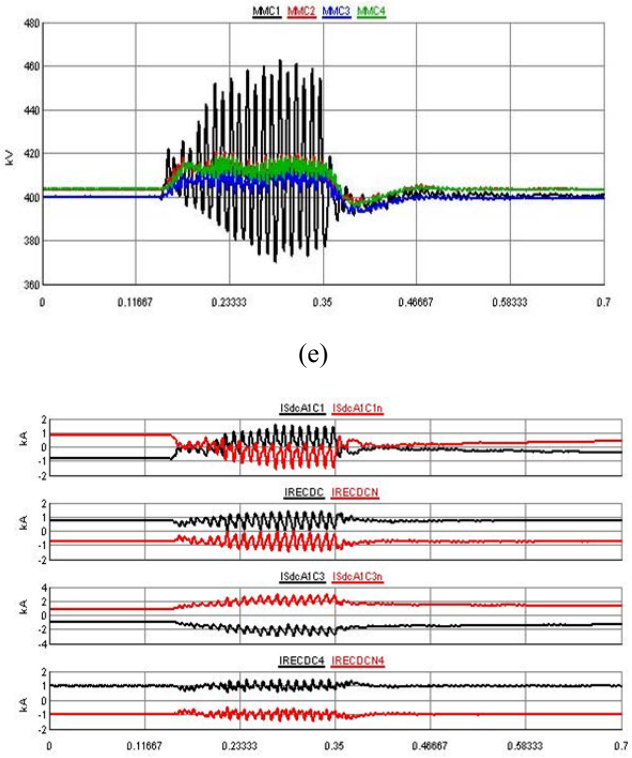

(e)

(f)

Fig. 5 *Three phase fault at MMC1 AC side (cont.)*

B. Pole to ground DC fault

Unlike AC faults, DC faults are almost always permanent and are caused by failure of cable insulation or damaged cable due to another source, e.g. ship anchors for undersea cables or fallen trees in case of overhead lines [12]. Thus, permanent DC fault has been considered in this study to include pole to ground and pole to pole fault scenarios. However, this scenario considers permanent pole to ground fault, which is applied at 1.60 *sec* at line 1 close to MMC1. The DC link voltage of MMC1&2 suddenly drops due to the positive pole capacitor voltage that starts drop till reaching zero as shown in Figure6-e. Here, the voltage drop of MMC2 takes a longer time compared with MMC1 due to fault location which is closed to MMC1.

When a drop in V_{dc} is monitored, MMC 1&2 reacts by supplying more current to the DC grid in order to compensate for the voltage drop. In this case, MMC 1 and 2 have the largest positive current values which lead to block MMC1 & MMC2 due to their internal protection scheme.

Nevertheless, MMC1 & MMC2 blocked their operation; the stored energy in the capacitors together with AC grid still feeds the fault. Consequently, CB12 and CB21 will meet the opening criteria, and a trip signal is sent to the DC breakers, CB12 & CB21, to open and isolate the faulty line. As soon as the DC breakers open which takes time of 5ms, the fault currents are extinguished from the MTDC grid.

In the meanwhile, MMC 3 and MMC4 terminals currents rise for few milliseconds but remain within the threshold range, resulting a temporary oscillation in their power flow due to fault propagation, then will continue their stable and healthy operation with the aim of grid controller. Note that both AC breakers, CB1 &CB2, are opened to enable next step of system restoration as discussed previously.

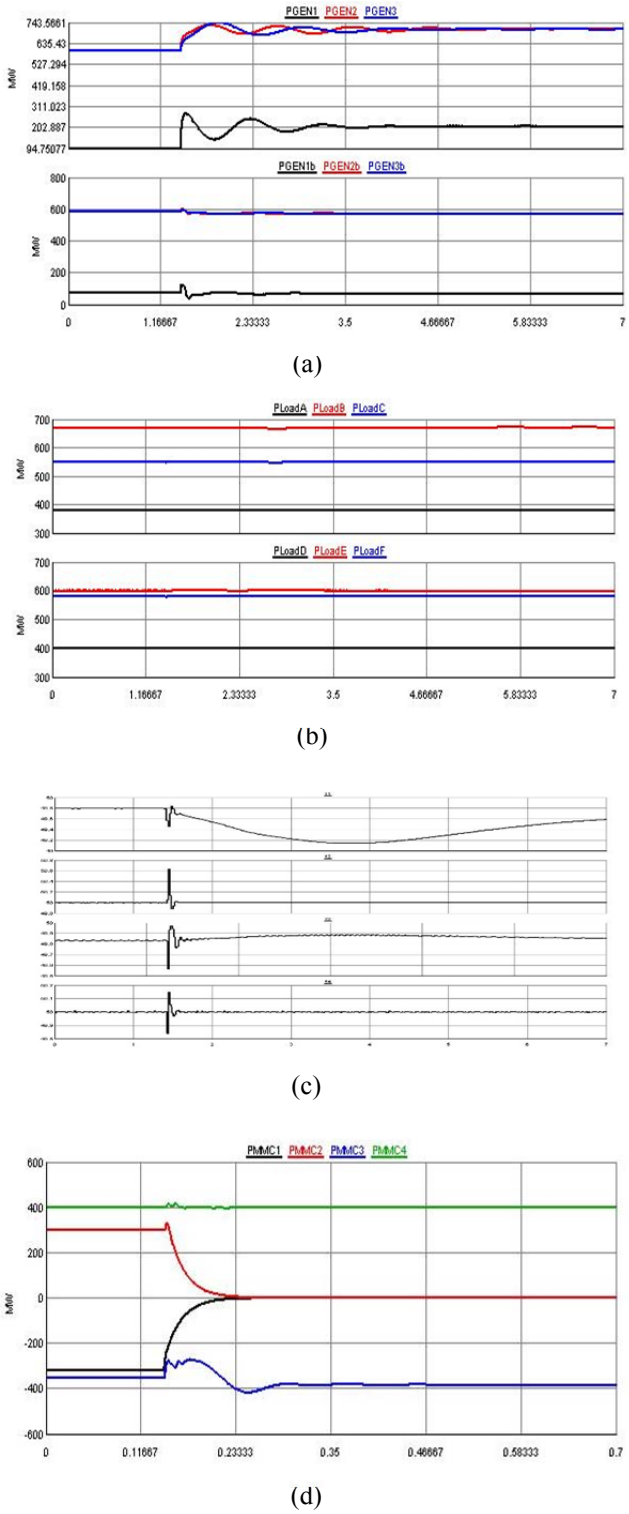

(a)

(b)

(c)

(d)

Fig. 6 *Permanent pole to ground DC fault at line 1.*

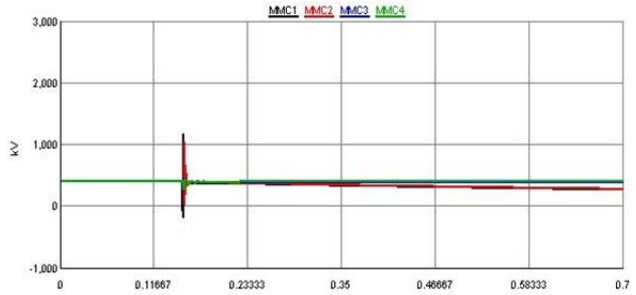

(e)

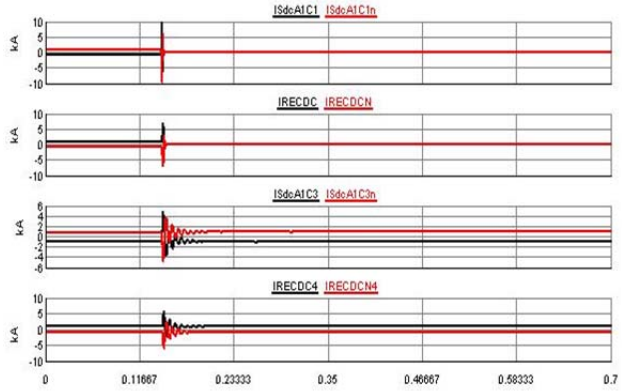

(f)

Fig. 6 *Permanent pole to ground DC fault at line 1 (cont.)*

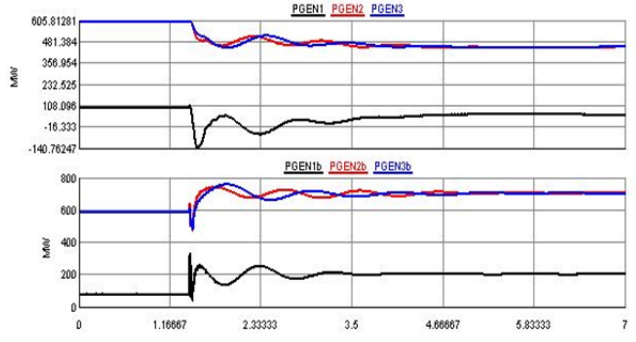

(a)

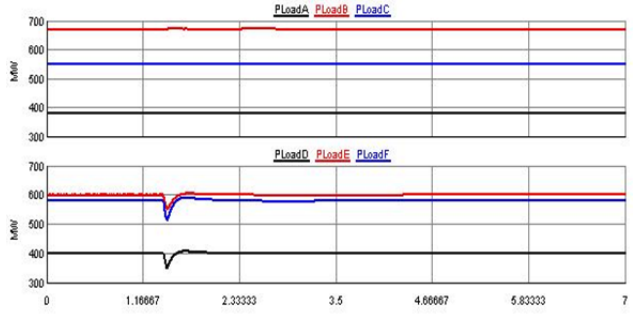

(b)

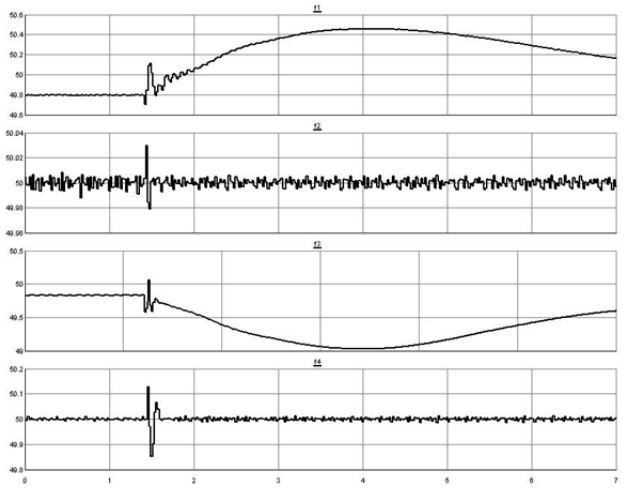

(c)

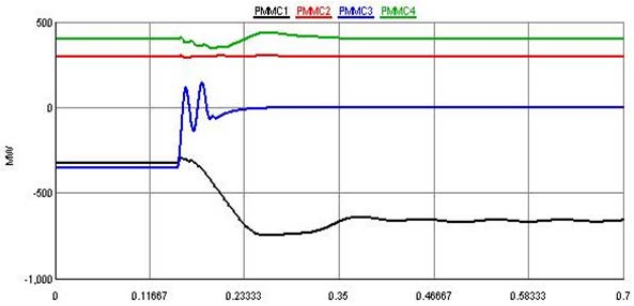

(d)

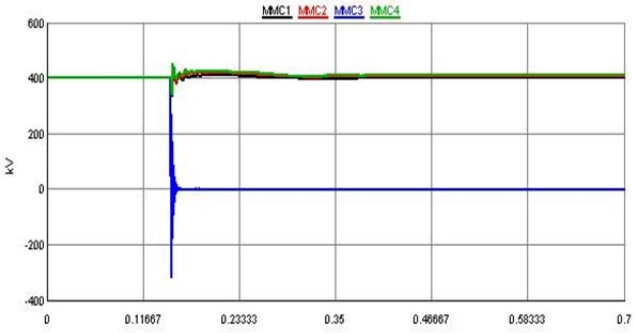

(e)

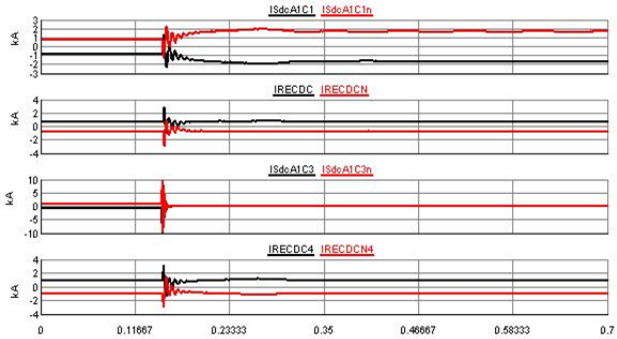

(f)

Figure 7. *Permanent Pole to pole fault at MMC3 side*

C. Pole to pole DC fault

Pole to pole DC fault is applied closed to MMC3, between converter terminal and the closest DC breakers, CB33 and CB34. In this case, MMC3 blocked its operation and a trip signal is sent by overcurrent protection relays to the closest DC breakers, CB33 & CB34, to open. In the meanwhile, a trip signal is sent to the relevant AC breaker CB3 to open and stop feeding the fault from the AC grid side and to preserve stable and secure AC grid operation as depict in Figure7.

5. DISCUSSION

As shown in the results, MTDC grid was able to preserve a stable and uninterruptable operation to deliver offshore wind power in different fault conditions. In case of three phase AC fault at AC grid1 which is the most severe condition, a large current is drawn to feed the fault from both AC and DC sides, resulting considerable power oscillation with a frequency deviation to reach 51.75 and 48.2 in AC grid1, which may triggers overfrequency and underfrequency protection relays that is not included in this work. While, less effect is observed in opther parts of hybrid AC/DC network.

In case of pole to ground permanent DC fault in DC line1, large current is induced to feed the fault and both MMC1 and MMC2 blocked their operation by blocking their respective IGBTs. The DC link voltage of both MMC1 and MMC2 gradually drops due to the drop in positive pole capacitor voltage, and both converters reacts by supplying more current to the DC grid inorder to compensate the voltage drop. Based on protection scheme selectivity, the overcurrent protection relays belongs to MMC1 and MMC2 are experienced to send a trip signal to the relevant DC breakers, CB11 and CB12, to fast isolate the faulted line. In the meanwhile, fault is propagated to other parts of the hybrid AC/DC system causing acceptable temporary oscillations. While, in case of pole to pole fault close to MMC3, only MMC3 blocked its operation and sudden voltage drop is observed. A trip signal is sent to both AC,CB4 , and DC breakers, CB33 and CB43, to open and isolate the faulted section from AC grid2 as well as MTDC grid.

6. CONCLUSION

Fast and selective protection shceme has been used with local measurements from each station terminals to achieve DC fault clearing capability. The results show that the proposed protection scheme is able to fast isolate the DC faulted section without the need of de-energizing the whole MTDC grid, thus achieve secure and reliable operation for wind power delivery. The fault analysis has revealed the significant advantage of MTDC grid with its control and protection to limit AC and DC fault propagation influence on other connected healthy systems. This paper provides a real-time platform to understand and tackle DC fault dynamics in MTDC grids, and study fault propagation influence on overall hybrid AC/DC network dynamic behavior and performance.

REFERENCES

[1] K. Meah, S. Ula, "Comparative evaluation of HVDC and HVAC transmission systems," *IEEE Power and Energy Society General Meeting conf.,* pp.1-5, 2007.

[2] Guide for the Development of Models for HVDC Converters in a HVDC Grid, CIGRE Std. B4.57, Dec. 2014.

[3] N. R. Chaudhuri, B. R. Majumder, A. Yazdani, Multi-terminal Direct-Current Grids Modeling, Analysis and Control, p 153-159, 2014.

[4] V. Preethi, P. Usha and J. Sreedevi, "Simulation of voltage source converter based multi-terminal HVDC system using RTDS," in *Proc*. *IRAJ International Conf*., Pune, India, 2013.

[5] P. Wang, Z. Li, X. Zhang, P. Zhang amd P.F. Coventry "DC fault management for VSC MTDC system using delyed-auto-reconfiguration scheme," *IEEE Int. Conf. on AC and DC Power Transmission.,* pp.1-7, 2015.

[6] S. Liu, Z. Xu, W. Hua, G. Tang and Y. Yue, "Electromechanical transient modeling of modular multi-level converter based multi-terminal HVDC system," IEEE Trans. Power Systems, vol. 29, pp.72-83, 2014.

[7] A. Artjoms, D. Gamboa, "Control of MMC in HVDC application," M.Sc. thesis, Dept. Energy Tech., Univ. Aalborg, Denmark, 2013.

[8] N. Serbia, "Modular multilevel converter for HVDC power," PhD. dissertation, INP Toulouse, Univ. Toulouse, France, 2014.

[9] M. Guan, Z. Xu, H. Chen, "Control and modulation strategies for modular multilevel converter based HVDC system," *IEEE Industrial Electronic Society Conf*., pp.849-854, 2011.

[10] N. Chaudhri, B. Chaudhuri, R. Majumder, "Multi-Terminal Direct- Current Grids: Modeling, Analysis, and Control", Wiley, 2014.

[11] K. Kadriu, A. Gashi, I. Gashi, A. Hamiti amd G. Kabashi, "Influence of dc component during inadvertent operation of the high voltage generator circuit breaker during mis-synchronization," *Energy and Power Engineering conf*., pp.225-235, 2013.

[12] Björn Jacobson, ABB Power Systems-HVDC, "Developments in Multiterminal HVDC," *IEEE EPEC*, Manitoba, 2011.

Modelling of a Supply Task of German High Voltage Network Based on Public Sources

K. Sangay

Manuscript received September, 2016
Revised November, 2016

ABSTRACT

The proliferation and integration of renewable energy sources to the electrical networks are rapidly growing in Germany. This has resulted into formation of complex electrical network systems in Germany. In this paper, an alternative modelling technique is explored to estimate a supply task for 110 kV high voltage substation by augmenting the existing method with mapping solution to model loads and feed-ins from renewable energy source using crowdsourced data and statistical data available in the public domain. The result derived illustrates static loads in megawatt (MW) and available photovoltaic feed-ins in MW to the high voltage substation.

Keywords: *high voltage network, renewable energy source, modelling, supply task*

1 INTRODUCTION

The proliferation of renewable energy sources (RES) and its integration to the network are increasing rapidly in Germany. There are more RES integration to distribution networks (high voltage, medium voltage and low voltage) than to the transmission network (extra high voltage) in Germany [1]. The combined generation from RES made up around 35% of net power supply [2]. The increasing of feed-ins from RES to the distribution networks have led to formation of complex electrical network systems in Germany and also complex modelling methods.

The combined loads and feed-ins from RES in the underlying medium voltage (MV) and low voltage (LV) networks are ultimately connected to the upstream high voltage (HV) network. Only large industrial power plants, large loads and large RES generating plants are directly connected HV network. Therefore, based on the existing loads and feed-ins from RES, HV/MV substation (primary substation) supply task must be evaluated. To quantify the loads and feed-ins from RES acting to the primary substation. Also the demand on the HV network influences extra high voltage network requirements.

Deriving an appropriate model of an electrical network is important for network analysis. To define primary substation supply task an adequate data on loads and underlying networks are required. Without these information, it is difficult to calculate supply task of primary substation or to any other substations. Therefore, a model to evaluate primary substation supply task is required to assess the distribution of loads and presence of feed-ins from RES and to evaluate the supply task of primary substation.

K. Sangay is with the Sirindhorn International Thai-German Graduate School of Engineering, King Mongkut\'s University of Technology North Bangkok, 1518 Pracharat 1 Road, Bangsue, Bangkok 10800, Thailand. Email: karma.s-epe2014@tggs-bangkok.org

2 GERMANY HIGH VOLTAGE NETWORK

The HV distribution network is meshed and only large industrial customers are connected directly to this network.

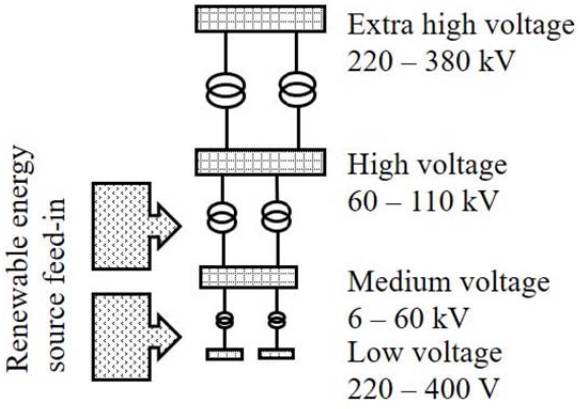

Fig. 1 *Germany electrical networks and renewable energy source feed-ins*

The underlying MV and LV distribution networks are fed from upstream HV network. The HV distribution network is operated at 110 kV with (n-1) contingency [3] and constitute more than 96 thousand kilometres in length and 100 separate networks in Germany [4].

In Germany, about 97% of all RES are installed to distribution networks [1]. Legacy method of treating distributed network as an equivalent load is no more valid in transmission system analysis [5]. Hence, the whole electrical network must be taken into consideration [1].

In order to define the supply task of primary substation, loads and RES plants directly connected to HV network, and loads and RES plants in underlying network MV and LV must be aggregated. The layout of underlying distribution network (MV and LV) are not examined in this paper. Figure 1 illustrates German's electrical networks and RES feed-ins. The feed-ins from

RES to extra high voltage (EHV) are omitted from the diagram.

3 Modelling Approach to Define the Primary Substation Supply Task

To calculate the supply task of primary substation, an integrated model of the feed-ins from RES, loads and primary substation must be developed.

3.1 Representation of Renewable Feed-ins and Loads

In this paper two loads (residential and industrial) and PV feed-ins in the postal region (PR) are considered. The data on number of households in a PR is from public website maintained by Statistical Federal Bureau Germany [6] and PV feed-ins are from energy map public website [7]. The residential load is calculated based on the strandard load profile (SLP) [8] of 1.83 kW peak demand per household in a PR and the industrial loads are derived from the residential load based on the load profile in the PR.

The loads and PV feed-ins are considered static and uniformly distributed. Later is also considered to be distributed on every household rooftop.

3.2 Topographical data

To reproduce the fractal map of the load distribution (load area) in PRs topographical data are required. These topographical data are from the openstreetmap (OSM) built by enthusiastic community of mappers. The fractal maps are reproduced from the OSM are complex polygons and Gaussian trapeze-formula is used to calculate the area As.

$$A_s = \frac{1}{2} \cdot \left| \sum_{s=1}^{n} (y_s + y_{s+1}) \cdot (x_s - x_{s-1}) \right| \quad (1)$$

where xs and ys are nth edges of the polygon line [1].

The OSM extensible mark-up language (XML) map files of PRs were downloaded using OSM Extended Application Programming Interface (API)[9]. The topographical data of the load areas are sorted by *tag*describing OSM data elements.

3.3 Allocation of PV feed-ins and loads to the network

To deduce primary substation supply task, primary substation supply area must be defined to allocate loads and PV feed-ins from the postal region. Since, the primary substation supply task is defined by aggregating all loads in the underlying MV network and those directly connected to the HV network. The supply area is defined by the MV regions. The MV regions are generated by Voronoi diagram (VD) around the predetermined 110 kV primary substation location. The generated MV region is superimposed on the geographical plane based on the location of the primary substation to list the intersection of postal region with MV region.

This paper applies VD methods and calculation of overlapping areas – correction factor – described in [1] to calculate loads and PV feed-ins in MV region according to equation (2).

$$p_{ij} = \frac{A_{s,ij}}{A_{s,i}} \cdot 100\% \quad (2)$$

Where, $p_{ij}$is the overlap of a postal region ith to MV region jth. $A_{s,}$ is the overlapping load area of PR i in MV region, and $A_{s,}$ is the total area of load area. This is illustrated in the figure 2, for clarity primary substation inside the MV region has been omitted.

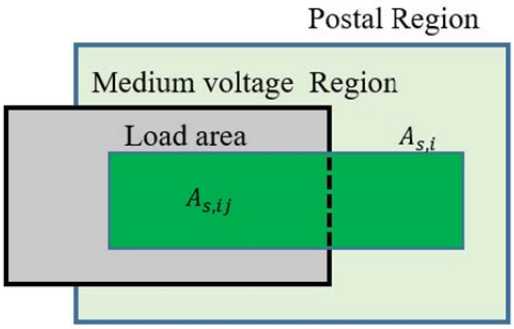

Fig. 2 *Overlapping of load area from postal region to MV region*

Since, the loads and the PV feed-ins are considered uniformly distributed in each postal region. Loads and PV feed-ins per primary substation is obtained using equation (3) [1].

$$p_j = p_{ij} \cdot P_i \quad (3)$$

where p_j is either load or PV feed-in, in the MV region and P_i is either load or PV feed-in in ith postal region. The primary substation supply task is therefore calculated by aggregating all the loads and PV plant inside the MV region.

4 Results

The result based on the model developed is presented here.

4.1 HV supply task modelling for sub-urban region

The method described has been implemented in Matlab program. The program through iterative process calculates loads, load areas in every PRs and fractionalizes to estimate MV region loads and PV feed-ins.

Figure 3, represents fractal map of the loads in the PRs and MV region in the state of Lower Saxony, Germany. The residential load areas are shaded in blue, industrial load areas are shaded in red, postal region delimitation boundary are indicated in thin solid black line, MV region is indicated in thick solid black line and the primary substation is indicated by square with dark blue outline and yellow fill.

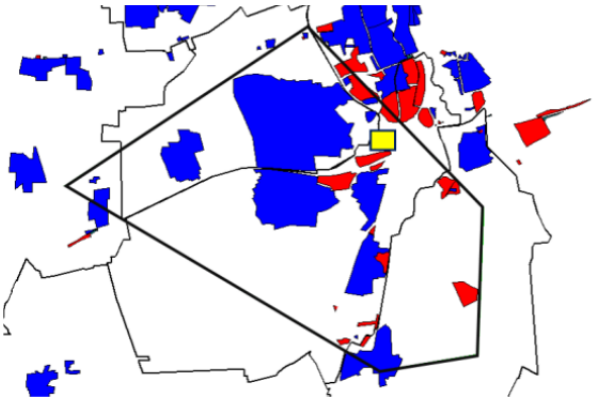

Fig. 3 *Fractal map of load areas in PRs and MV region*

The MV region under investigation spreads to 5 PRs which forms part of the MV region. From the plot major portion of the area within the MV region constitutes mostly residential loads and marginal industrial loads.

The primary substation supply task in the figure 3 has been investigated and the results are graphically represented in figure 4.

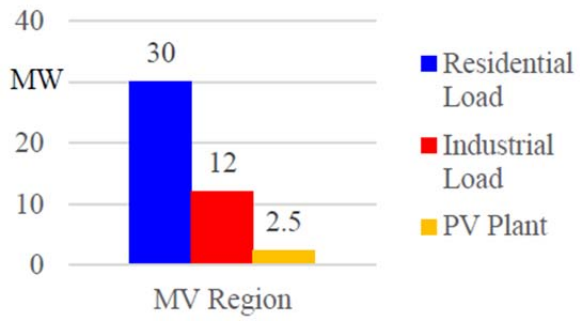

Fig. 4 *Sub-urban MV region supply task*

The primary substation supply task is aggregated to 42 MW with 30 MW residential load and 12 MW industrial load, and 2.5 MW of PV plant.

5 CONCLUSION

The modelling technique to define primary substation supply task using method described in [1] with mapping solution was presented in this paper. The exemplary results obtained, confirms the possibilities of determining the supply task of a primary substation explicitly using public data and OSM. However, in the exemplary investigation other loads and RES feed-ins were omitted. This omission can potentially lead to underestimation of the HV supply task. Therefore, all loads and RES feed-ins in the MV region must be accounted for proper estimation of primary substation supply task.

6 ACKNOWLEDGMENT

The authors of the paper would like to sincerely extend appreciation to Univ.-Prof. Dr.-Ing. Albert Moser and Dipl.-Ing. Lukas Verheggen for an overarching guidance and for accepting me to carry out research work IAEW, RWTH Aachen University.

REFERENCES

[1]. S. Dierkes, F. Bennewitz, M. Maercks, L. Verheggen and A. Moser, "Impact of Distributed Reactive Power Control of Renewable Energy Sources in Smart Grids on Voltage Stability of the Power System," in *2014 Electric Power Quality and Supply Reliability Conference (PQ)* , Rakvere, June 2014.

[2]. "OpenStreetMap," Wikimedia Foundation Inc. , 11 April 2016. [Online]. Available: https://en.wikipedia.org/wiki/OpenStreetMap. [Accessed 12 April 2016].

[3]. P. D. B. Burger, "Power generation from Renewable Energy in Germany– Assessment of 2015," Fraunhofer Institute for Solar Energy Systems ISE, Freiburg, January, 2016.

[4]. T. Connor, A. Ettinger and C. Boese, "Planning Approach for Evolution of Grown Medium Voltage Distribution Networks," in *IEEE*, Guangzhou, China, December 2008.

[5]. F. M. f. E. A. a. Energy, "Electricity Grids of the Future," [Online]. Available: http://www.bmwi.de/EN/Topics/Energy/Grids-and-grid-expansion/electricity-grids-of-the-future.html. [Accessed 17 06 2016].

[6]. H. Jia, W. Qi, Z. Liu, B. Wang, Y. Zeng and T. Xu, "Hierarchical Risk Assessment of Transmission System Considering the Influence of Active Distribution Network," *IEEE Transactions on Power Systems,* vol. 30, no. 2, pp. 1084 - 1093, October 2014.

[7]. "Statitstisches Bundesamt," 2013. [Online]. Available: http://www.destatis.de. [Accessed 10 May 2016].

[8]. "Die Karte Der Erneuerbaren Energien," Deutsche Gesellschaft für Sonnenenergie e.V., [Online]. Available: http://www.energymap.info/. [Accessed 10 May 2016].

[9]. V. B. W. F. Marian Hayn, "Electricity Load Profiles in Europe: The Importance of Household," *Energy Research & Social Science,* vol. 30, pp. 30-45, 2014.

Modeling and Analysis of Temporary Fault Simulation in Self-Excited Induction Generator System Applied for Fixed-Speed Wind Turbin

J. Saijai[1] M. Krueger[2] N. Thanomsat[1] and B. Plangklang[3]

Manuscript received October, 2016
Revised December, 2016

ABSTRACT

In this paper, a Self-Excited Induction Generator (SEIG) applied for a Fixed-Speed wind turbine system is modeled and simulated by using PSCAD/EMTDC program in order to analyze various transient phenomena from the transmission line temporary fault. The parameters of generator system model have been obtained from field wind power plant. The results show that during temporary line to ground fault through accident simulation between SEIG and transformer, could result in damage by increasing electrical torque and over speeding the rotor.

Keywords: *Fault simulation, Self-Excited Induction Generator, PSCAD/EMTDC, Transient phenomena*

1. INTRODUCTION

The increasing using of energy consumption in the world has pushed researchers to research non-conventional energy and to concentrate on a renewable energy and how to efficiency use it. In specific, modern research activities have been aimed toward the development of renewable energy in term of cost, efficiency and safety [1,2]. Wind energy is one of the renewable energy that is considered as a clean natural source. From these fact, wind energy capacity has been significantly increased for decades [3, 4]. The energy conversion from wind to electricity is performed by wind turbine, which is mainly the combination of turbine blade and electrical generator. However, wind energy is not attractive compared with other sources due to its high cost of investment, maintenance and operation (O&M) [5,6]. To make wind power competitive with other sources of energy, availability, reliability and the life of the wind turbines system are required to be improved. In order to achieve this requirement, the condition monitoring and fault diagnosis system has been integrated into wind turbine system. With this monitoring and diagnosis system, the abnormal conditions occurring inside the wind turbine will be detected and reported to the operator for early react and solve these situations.

According to the number distribution of the failures in Swedish wind power plant during year 200 - 2004 [7], the main failures relate to an electrical part, i.e. grid side (electric system) and wind turbine side (generator, sensors control system).

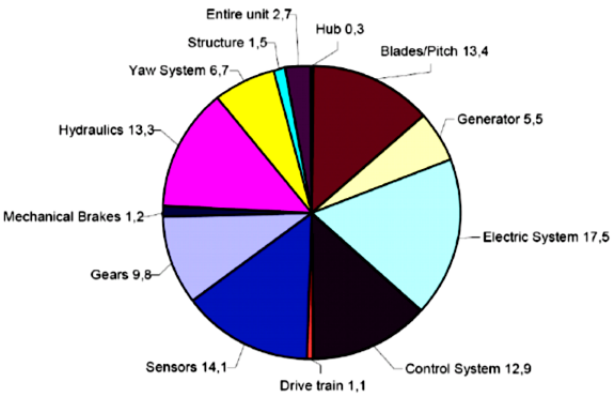

Fig. 1 *Number distribution of failure in Swedish wind power plant*

For the wind turbine side, an energy conversion system usually employ various kind of induction due to its simplicity, high reliability, low cost of maintenance and robustness [8,9,10]. Various type of induction generator have been installed to convert wind energy to electricity such as Squirrel cage type, Wound rotor type and Doubled-Fed type [24,25,26]. The speed of the prime mover can be considered as Fixed-Speed or Variable-Speed [28]. Electricity generation of an induction generator requires reactive power for excitation. This power can be taken from power grid or capacitor bank, which is called a self-excited [23, 27].

A Fixed-Speed SEIG is one kind of wind energy conversion scheme and has been considered by both academic and industrial side due to its ruggedness, brushless, low cost of maintenance, no required

J. Saijai[1] and **N. Thanomsat[1]** are with the Department of Electrical Engineering Faculty of Engineering Burapha University Chonburi, Thailand. Mail : jedsada@eng.buu.ac.th, nattapan@eng.buu.ac.th
M. Krueger[2] is with Institute of Automatic Control and Complex Systems University Duisburg-Essen Duisburg, Germany. Mail : minjia.krueger@uni-due.de
B. Plangklang[3] is with the Department of Electrical Engineering Faculty of Engineering Rajamangala University of Technology Thanyaburi Pathum thani, Thailand. Mail : boonyang.p@en.rmutt.ac.th

synchronization system and no need for DC excitation [29, 30]. Moreover, the torque of a Fixed-speed SEIG varies as a function of the rotor speed. Therefore it acts as an effective damper that reduces the magnitude of torque oscillations [22].

The typical electrical related failure in the wind turbine side includes inter-turn shot circuit in stator winding and broken rotor bar. These failures directly damage the wind turbine generator itself and when it is connected to the power grid, they will consequently affect the power stability and quality [31], [32].

In another hand for the grid side, connecting wind turbine may cause problems in power system quality and reliability, such as voltage variation and flicker. Therefore, new connecting rules are required in order to avoid negative effects on the existing electrical systems. In 2009, an overall perspective on contemporary issues like wind power plant and grid integration has been discussed and presented in [11]. Wind speed model, wind turbine model and flicker meter model have been simulated using MATLAB/Simulink software and the consequent impacts have been published in [12]. The results shown that the random fluctuation of wind speed and the inherent characteristic of wind turbine might cause severely flicker. The authors in [13] proposed the using of a detailed modeling to assess the transient stability of a grid connected wind turbine. By combining the grid connection, wind turbine flexibility and induction generator stability features, the critical clearing tine and critical speed have been mentioned. In 2008, dynamic responses of a typical fixed-speed induction generator wind turbine under the grid faults have been simulated using simulation package named Fatigue Aerodynamic and the results have been published in [14]. Meanwhile, the circuit breaker panels with dimensions suitable for wind farm application have been designed and reported in [15]. This circuit breaker panels secure a good fit of the distribution networks.

In all previous studies, possibility of the wind turbine system grid connected problem had been studied. However, an effect of grid faults to a Fixed-Speed SEIG has not been fully investigated. In this paper, a transient response of a Fixed-Speed SEIG wind energy conversion system subjected to grid faults will be simulated and analyzed using simulation software, PSCAD/EMTDC. Active and reactive power flow together with the SEIG electrical torque during the transient period will be also investigated.

2. GENERATOR DESCRIPTION AND EQUATIONS

The SEIG applied for a Fixed-Speed wind turbine connected to a grid at the point of common connection (PCC) is illustrated in Figure 2. Analytic modeling of SEIG wind turbine is well documented in the literature [16-18]. The equivalent circuit of the SEIG with the PCC is shown in Figure 3 [19].

According to the SEIG static equivalent circuit shown in Figure 2, equivalent electrical parameters are:

$$E = (I_m)(jX_m) = -I_r\left(\frac{R_r}{s} + jX_r\right) \quad (1)$$

$$I_m = I_s + I_r \quad (2)$$

$$V_s = E + I_s(R_s + jX_s) \quad (3)$$

$$P_m = 3I_r^2\left(\frac{R_r}{s}\right) \quad (4)$$

Where E is the air gap magnetic field electromotive force; I_s, I_r and I_m are stator, rotor and exciting current of SEIG, respectively; R_s and R_r are the stator and rotor resistances; X_s, X_r and X_m are the stator, rotor secondary leakage and magnetizing reactance, respectively. The parameters on the rotor side are converted to the stator side. P_m is the input generator power; s is the slip ratio, which is negative for generator. Considering the voltage equivalent and a small variation range of s in the real stable [20], it can be concluded that:

$$V_s \approx \left(\frac{I_r}{|s|X_m}\right)k_s \quad (5)$$

where:

$$k_s = \sqrt{M^2 + N^2} \quad (6)$$

$$M = -(sR_sX_r + sR_sX_m + X_sR_r + R_rX_m) \quad (7)$$

$$N = (R_sR_r - sX_rX_s - sX_mX_s - sX_rX_m) \quad (8)$$

The grid connected SEIG for a Fixed-Speed wind turbine shown in Figure 2 can be reduced to the equivalent circuit presented in Figure 3. This circuit is consequently represented with the Thévenin circuit as shown in Figure 4 where V_{in} and Z_{1th} are calculated by:

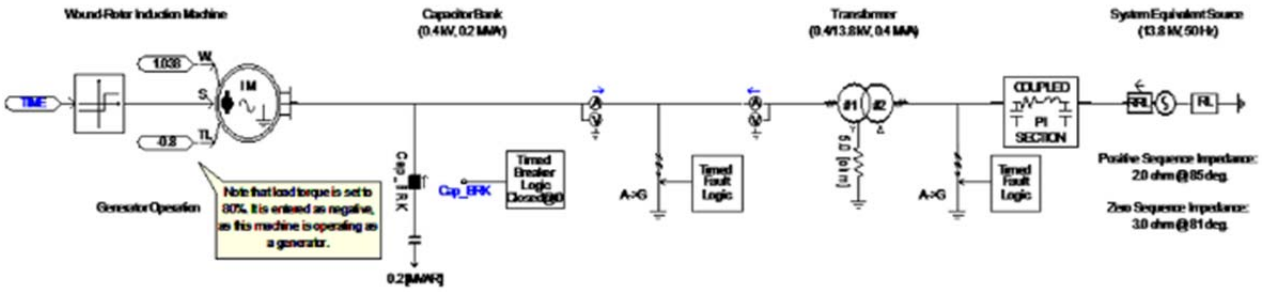

Fig. 2 *Grid connected SEIG applied for a Fixed-Speed wind turbine*

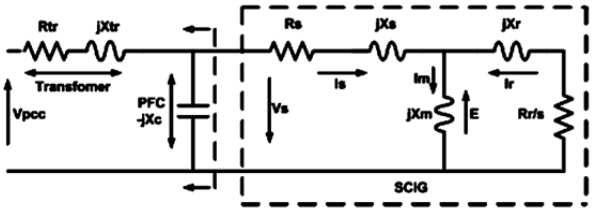

Fig. 3 *Equivalent circuit of SEIG with the PCC [19]*

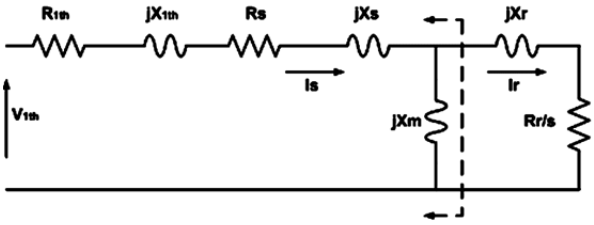

Fig. 4 *Reduced equivalent circuit of SEIG with the PCC [19]*

$$V_{1th} = \frac{V_{pcc} Z_c}{Z_{tr} + Z_C} \tag{9}$$

$$Z_{1th} = R_{1th} + jX_{1th} = \frac{Z_{tr} Z_C}{Z_{tr} + Z_C} \tag{10}$$

$$Z_C = -jX_c \tag{11}$$

$$Z_{tr} = R_{tr} + jX_{tr} \tag{12}$$

After that, the reduced circuit in Figure 4 is simplified to another Thévenin equivalent circuit. The new value of V_{th} and Z_{th} are calculated by:

$$V_{th} = \frac{V_{1th} Z_M}{Z_{1th} + Z_S + Z_M} \tag{13}$$

$$Z_{th} = R_{th} + jX_{th} = \frac{(Z_{1th} + Z_S) Z_M}{Z_{1th} + Z_S + Z_M} \tag{14}$$

$$Z_M = -jX_m \tag{15}$$

$$Z_s = R_s + jX_s \tag{16}$$

From this equivalent, the magnitude of the rotor current can be determined by:

$$I_r = \frac{V_{th}}{\sqrt{\left(R_{th} + \frac{R_r}{s}\right)^2 + \left(X_{th} + X_r\right)^2}} \tag{17}$$

and finally, the electrical torque T_e can be calculated by:

$$T_e = I_r^2 \left(\frac{R_r}{s}\right)\left(\frac{1}{\omega_s}\right) = \left(\frac{V_{th}^2}{\left(R_{th} + \frac{R_r}{s}\right)^2 + (X_{th} + X_r)^2}\right)\left(\frac{R_r}{s}\right)\left(\frac{1}{\omega_s}\right) \tag{18}$$

The electrical mechanical equilibrium equation of SEIG according to [21] is:

$$\frac{d\omega_R}{dt} = \frac{1}{2H}(T_e - T_m) \tag{19}$$

where ω_R is the rotor speed, H is the rotor inertia constant and T_m is mechanical torque.

3. MODELING AND SIMULATION BY PSCAD/EMTDC

A wound rotor induction machine, which is shown in Figure 2, is configured to operate as a generator at rated voltage 0.4 kV and rated power 0.5 MW. A Capacitor bank is connected directly to the generator terminals to supply the reactive power required to maintain its terminal voltage with rated voltage 0.4 kV and rated load 0.2 MVAR. Complete parameters of SEIG model is shown in Fig. 5.

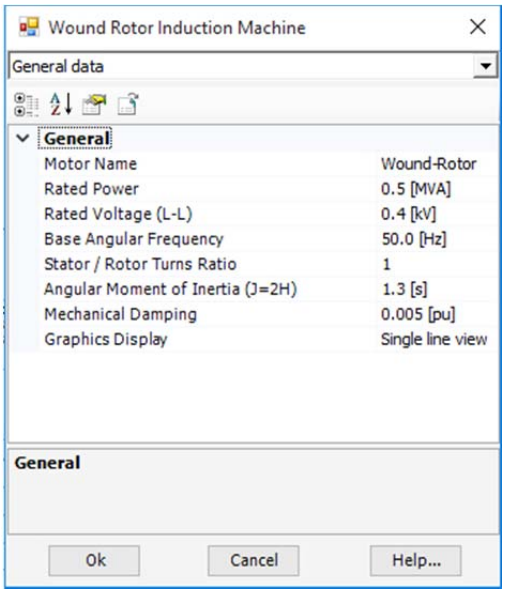

Fig. 5 *Completer parameters of SEIG model*

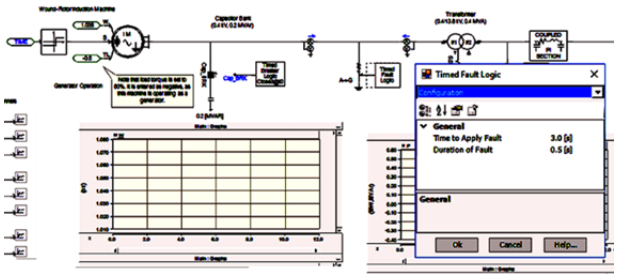

Fig. 6(a) *Fault simulation in PSCAD/EMTDC*

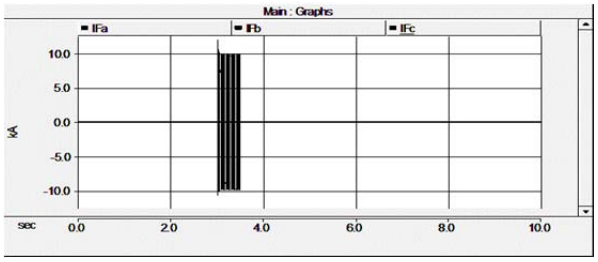

Figure 6(b). *Transient phenomenon in generator current subjected to LG fault*

Simulation of line to ground fault (LG fault), which is the most typical fault in electrical grid is performed. It is assumed that the LG fault occurs at phase A between generator and transformer terminals. The LG fault occurs at a time of 3 second and last for 0.5 second. The simulated LG fault in PSCAD/EMTDC and the transient phenomena of current are shown in Figure 6(a) and 6(b), respectively.

4. Simulation Results

According to the LG fault simulation by PSCAD/EMTDC in the previous section, the voltage waveform of the SEIG at steady state and transient period are shown in Figure 7(a) and 7(b), respectively.

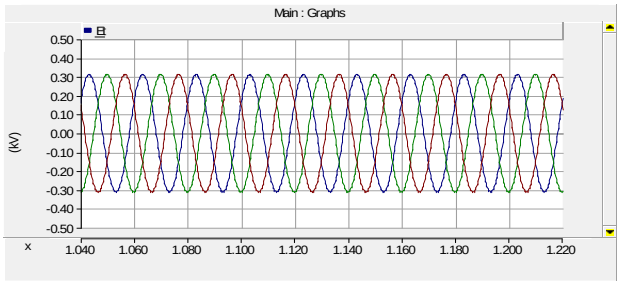

Fig. 7(a). *Voltage waveform of SEIG in steady state*

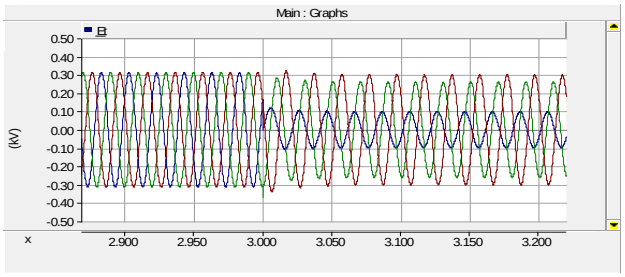

Fig. 7(b). *Voltage waveform of SEIG in transient period*

Waveforms of active and reactive power are also shown in Figure 8.

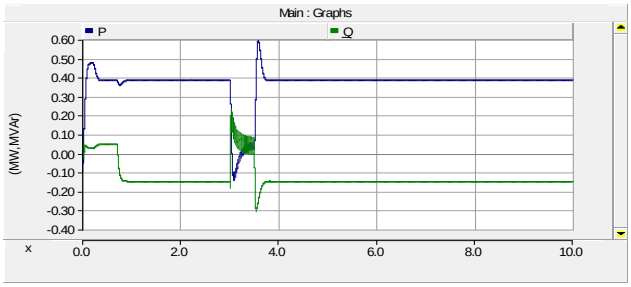

Fig. 8 *Active and reactive power of SEIG during LG fault*

Finally, the mechanical and electrical torque together with the rotor speed of SEIG during the LG faults are shown in Figure 9(a), 9(b) and 9(c), respectively.

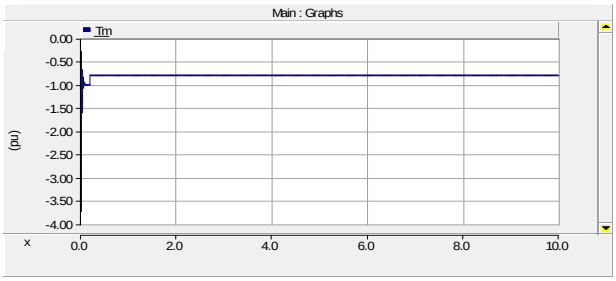

Fig. 9(a) *Mechanical torque of SEIG*

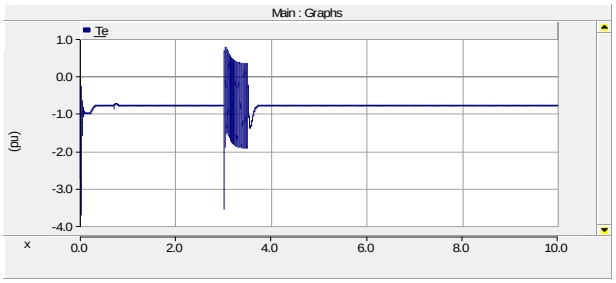

Fig. 9(b) *Electrical torque of SEIG*

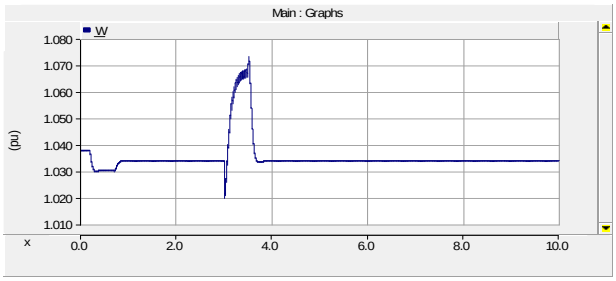

Fig. 9(c). *Rotor speed of SEIG*

According to these results, the mechanical torque T_m and electrical torque T_e are equal at -0.8 pu and the rotor speed ω_R is constant when the system reach a steady state. During the LG fault, it is clearly seen from Fig. 9(a), 9(b) and 9(c) that an electrical torque is smaller than mechanical torque. This causes the rotor of SEIG to speed up and results in electrical system unstable. The LG fault also subsequently fluctuates the active and reactive power as shown in Fig. 8.

5. Conclusion

In this paper, a SEIG as the power conversion system for the Fixed-Speed wind turbine subjected to LG fault has been simulation using the dedicated power electronics and system simulation PSCAD/EMTDC. Based on the simulation results, when an accident LG fault occurs between the SEIG and transformer terminals, the negative sequence of current and electrical torque are increased. These results the overheating and damage to SEIG. Moreover, it is also clearly seen that LG fault causes the SEIG to perform as the motor, which is an undesirable behavior of SEIG.

In the future, the fault diagnosis system for SEIG will be developed such that it has ability to detect, isolate and

distinguish the fault that occurs inside SEIG and grid fault side.

6. ACKNOWLEDGMENT

This paper is a part on the cooperation of the Thai-German S&T Cooperation: the 2nd Call of Researcher Mobility Scheme. The authors would like to thank our colleagues from Institute of Automatic Control and Complex Systems (AKS), University Duisburg – Essen, Germany who provided insight and expertise that greatly assisted of this work.

REFERENCES

[1]. Golovanov, N.; Lazaroiu, G.; Roscia, M.; Zaninelli, D. Power Quality analysis in Renewable Energy Systems Supplying Distribution Grids. Measurements 2013, 7, 6–95.

[2]. Duong, M.Q.; Ogliari, E.; Grimaccia, F.; Leva, S.; Mussetta, M. Hybrid model for hourly forecast of photovoltaic and wind power. In Proceedings of the 2013 IEEE International Conference on Fuzzy Systems (FUZZ), Hyderabad, India, 7–10 July 2013; pp. 1–6.

[3]. Kim, H; Lu, D. Wind Energy Conversion System from Electrical Perspective—A Survey. Smart Grid and Renewable Energy, Vol. 1 No. 3, 2010, pp. 119-131.

[4]. International Renewable Energy Agency. Renewable energy technologies: Cost analysis series. Report, International Renewable Energy Agency, 2012.

[5]. Joshi D. R.; Jangamshetti, S. H. A Novel Method to Estimate the O&M Costs for the Financial Planning of the Wind Power Projects Based on Wind Speed—A Case Study. In IEEE Transactions on Energy Conversion, vol. 25, no. 1, pp. 161-167, March 2010.

[6]. Qian, P.; Ma, X.; Wang, Y. Condition monitoring of wind turbines based on extreme learning machine. Automation and Computing (ICAC), 2015 21st International Conference on, Glasgow, 2015, pp. 1-6.

[7]. Amirat, Y.; Choqueuse, V.; Benbouzid, M. Wind turbines condition monitor-ing and fault diagnosis using generator current amplitude demodulation.. In Proceeding of the IEEE International Energy Conference and Exhibition (EnergyCon) 2010, Manama, Bahrain, Dec 2010, pp.310–315.

[8]. Simões, M.G.; Farret, F.A. Renewable Energy Systems: Design and Analysis with Induction Generators. CRC Press, 2004.

[9]. Sava, G.N.; Costinas, S.; Golovanov, N.; Leva, S.; Duong, M.Q. Comparison of active crowbar protection schemes for DFIGs wind turbines. In Proceedings of the 2014 IEEE 16th International Conference on Harmonics and Quality of Power (ICHQP), Bucharest, Romania, 25–28 May 2014; pp. 669–673.

[10]. Duong, M.Q.; Le, K.H.; Grimaccia, F.; Leva, S.; Mussetta, M.; Zich, R. Comparison of power quality in different grid-integrated wind turbines. In Proceedings of the 2014 IEEE 16th International Conference on Harmonics and Quality of Power (ICHQP), Bucharest, Romania, 25–28 May 2014; pp. 448–452.

[11]. Hansen A.D.; Cutululis, N.A.; Sorensen, P.; Iov, F. Grid integration impacts onwind turbine design and development. IEEE Bucharest PowerTech: Innovative Ideas Toward the Electrical Grid of the Future 2009 (Art. no. 5282043).

[12]. Linh, N.T. Power quality investigation of grid connected wind turbines. In: Proceedings of the 4th IEEE Conference on Industrial Electronics and Applications, ICIEA; 2009 p. 2218–2222. Article no. 5138593.

[13]. Fajardo, R.L; Medina, A.; Iov, F. Transient stability with grid connection and wind turbine drive-train effects. In: Proceedings of IEEE Electrical Power and Energy Conference 2009, EPEC; 2009. Article no. 5420768.

[14]. Song Z.; Xia C.; Chen, W. Analysis of wind turbine structural loads under grid fault. In Proceedings of the 11th International Conference on Electrical Machines and Systems 2008, ICEMS; 2008. p. 2277–82. Article no. 4771128.

[15]. Landsverk, H.; Granhaug, O.; Skryten, P.; Rafoss, S.E. 36 KV vacuum circuit breaker panel – the perfect switchgear for wind IET Conference Publications (550 CP); 2009.

[16]. Fernandez, L.; Garcia, C.; Saenz, J.; Jurado, F. Equivalent models of wind farms by using aggregated wind turbines and equivalent winds. Energy Convers. Manag. 2009, 50, 691–704.

[17]. Duong, M.Q.; Grimaccia, F.; Leva, S.; Mussetta, M.; Sava, G.; Costinas, S. Performance analysis of grid-connected wind turbines. UPB Sci. Bull. Ser. C 2014, 76, 169–180.

[18]. Duong, M.Q.; Grimaccia, F.; Leva, S.; Mussetta, M.; Zich, R. Improving LVRT characteristics in variable-speed wind power generation by means of fuzzy logic. In Proceedings of the 2014 IEEE International Conference on Fuzzy Systems (FUZZ-IEEE), Beijing, China, 6–11 July 2014; pp. 332–337.

[19]. Haque, M. Evaluation of power flow solutions with fixed speed wind turbine generating systems. Energy Convers. Manag. 2014, 79, 511–518.

[20]. Zhang, J.; Yin, Z.; Xiao, X.; Di, Y. Enhancement voltage stability of wind farm access to power grid by novel SVC. In Proceedings of the 4th IEEE Conference on Industrial Electronics and Applications, 2009 (ICIEA 2009), Xi'an, China, 25–27 May 2009; pp. 2262–2266.

[21]. Grilo, A.P.; Mota, A.; Mota, L.T.M.; Freitas, W. An analytical method for analysis of large-disturbancestabilityofinductiongenerators. PowerSyst. IEEETrans. 2007,22,1861–1869.

[22]. Ewais, A. M.; Ugalde-Loo, C.; Ekanayake, J. B.; Liang, J.; Jenkins, N. Influence of Fixed-Speed Induction Generator-Based Wind Turbines on Subsynchronous Resonance. Universities' Power Engineering Conference (UPEC), Proceedings of 2011 46th International, Soest, Germany, 2011, pp. 1-6.

[23]. Bansal, R. C. Three-phase self-excited induction generators: an overview. In IEEE Transactions on Energy Conversion, vol. 20, no. 2, pp. 292-299, June 2005.

[24]. Muller, S.; Deicke, M.; De Doncker, R. W. Doubly fed induction generator systems for wind turbines. In IEEE Industry Applications Magazine, vol. 8, no. 3, pp. 26-33, May/Jun 2002.

[25]. Chen, H.; Aliprantis, D. C. Analysis of Squirrel-Cage Induction Generator With Vienna Rectifier for Wind Energy Conversion System. In IEEE Transactions on Energy Conversion, vol. 26, no. 3, pp. 967-975, Sept. 2011.

[26]. Marzebali, M. H.; Kia, S. H.; Henao, H.; Capolino, G. A.; Faiz, J. Planetary Gearbox Torsional Vibration Effects on Wound-Rotor Induction Generator Electrical Signatures. In IEEE Transactions on Industry Applications, vol. 52, no. 6, pp. 4770-4780, Nov.-Dec. 2016.

[27]. Konstantopoulos, G. C.; Alexandridis, A. T. Full-Scale Modeling, Control, and Analysis of Grid-Connected Wind Turbine Induction Generators With Back-to-Back AC/DC/AC Converters. In IEEE Journal of Emerging and Selected Topics in Power Electronics, vol. 2, no. 4, pp. 739-748, Dec. 2014.

[28]. Das, D.; Haque, M. E.; Gargoom, A.; Negnevitsky, M. Control strategy for combined operation of fixed speed and variable speed wind turbines connected to grid. In 2013 Australasian Universities Power Engineering Conference (AUPEC), Hobart, TAS, 2013, pp. 1-6.

[29]. Krichen, L.; Francois, B.; Ouali, A. A fuzzy logic supervisor for active and reactive power control of a fixed speed wind energy conversion system. Electric Power Systems Research, Volume 78, Issue 3, March 2008, Pages 418-424.

[30]. Singh, B.; Murthy, S.S.; Gupta, S. Analysis and design of STATCOM-based voltage regulator for self-excited induction generators. In IEEE Trans. Energy Convers., 19 (December (4)) (2004), pp. 783–790.

[31]. Devaraj, D.; Jeevajyothi, R. Impact of wind turbine systems on power system voltage stability. In proceeding of the 2011 International Conference on Computer, Communication and Electrical Technology (ICCCET), Tamilnadu, 2011, pp. 411-416.

[32]. Chowdhury, M. A.; Shen, W. X.; Hijazin, I.; Hosseinzadeh, N.; Pota, H. R. Impact of DFIG wind turbines on transient stability of power systems — A review. In proceeding of the 2013 IEEE 8th Conference on Industrial Electronics and Applications (ICIEA), Melbourne, VIC, 2013, pp. 73-78.

Optimal Mixture Experiment Design Using Neural Network

D. Buntam,W. Permpoonsinsub and P. Surin

Manuscript received October, 2016
Revised December, 2016

ABSTRACT

Forming process is essential and necessary for manufacturing system. Mixture experiments are useful in industrial situation to find the parameters in design and development process. Artificial Neural Network (ANN) is the mathematical model to approximate and predict a nonlinear function. In this study, the objective is to simulate optimal parameters mixture experiments by the ANN. The ANN architecture is widely used that is feed-forward back propagation. There are two design methods namely, integration with mixture design and factorial design. In the integration with mixture design, the input data, pellet talcum, are trained for ANN. The target data are from factorial design. Training algorithms in the experiments, Gradient descent, Gradient descent with momentum and Levenberg Maquardt algorithms are applied to optimize components. The performance of ANN model can be indicated by mean square error (MSE) and linear regression (R). As a result, ANN can predict yield of forming process of pellet talcum.

Keywords: *artificial neural network, mixture design and mineral talcum*

1. INTRODUCTION

Mineral talcum production is the one of important process in industry. Mineral talcum is a components in cosmetic, powder paper and lime. Uttaradit province is the original resource to produce mineral Talcum in Thailand. There are many mining industry and processing factory mineral talcum in Uttardit province. For 30 year ago, the most industry is only primary processing factory which is blending and packaging to other suppliers.

D. Buntam,W. Permpoonsinsub and P. Surin are with the Faculty of Engineering Pathumwan Institute of Technology (PIT) Bangkok Thailand. Email: dussadeebuntam@gmail.com, wachirapond.pit@gmail.com and prayoon99@gmail.com

(a) Original mieral talcum (b) Mieral talcum pellet

Fig. 1 *Mineral Talcum Process*

The characteristic of mineral talcum is very small pieces of powder so it spreads during package and transportation. Not only it affects health but also it is the cause of environmental problems including carcinogens of cancer. To reduce spreading mineral talcum, the production process should be based on the environmental management standard, ISO 14000. Thus, the mineral talcum factories should develop a new process to change original mineral talcum in Fig.1 (a) to mineral talcum pellet in Fig.1 (b). According to Fig.1, mineral talcum is mixed with a few water, it is broken and isolated. In case of more water, it is flat shape. In following problems on shape of mineral talcum, the optimal mixture experiment design using ANN is applied to solve forming process of mineral talcum. ANN models are designed to predict yield forming process for reducing the defect. In this paper, the aim is to optimize the components of water and mineral talcum in forming process by artificial neural network model.

2. BACKGROUND AND LITERATURE REVIEWS

A. Literature reviews

Macleod et al. have applied ANNs and Taguchi method were used to predict hardest of cement. Taguchi methods offer potential benefits in evaluating network behavior such as the ability to examine interaction of weights within neurals a network (MACLEOD, DROR, & MAXWELL, 1999). Adroer et al. presented neural network model for predicting the honing process variables (grain size of abrasive, density of abrasive, linear speed, tangential speed and pressure) as a function of roughness parameters (Adroera, Parrab, Corralc, & Calvetca, 2015). Yadollahi et al. have investigated the optimal mixture of RSC containing lead-slag aggregate used Taguchi method and ANN. They have also predicted component of UV-protection concrete by important factor which had three variables as slum, compressive strength and gramma linear attenuation. The coefficient were considered as the quality responses

(Yadollahi, Nazemi, Zolfaghari, & Ajorloo, 2016). Sukru Ozsahin have studied an ANN model which was developed for predicting the effects of some production factors such as adhesive ratio, press pressure, time, wood density and moisture content on some physical properties of oriented strand board (OSB). The results showed that the prediction model was a useful, reliable and quite effective tool for predicting some physical properties of the OSB produced under different manufacturing conditions (Ozsahin, 2013).

B. ***Atifitual Neural Network***

A biological neural network is a series of interconnected neural and a biological process in the human brain. The sample processing elements are connected by weighted. The forming are combined from a number of the simple processing elements. The simple processing elements compute the output by a non-linear function of weight inputs **(Sarma & Sarma, 2000)**. According to Fig.2, the biological neuron are demonstrated. The signals transmitted through the cell body (soma) which are from the dendrite to the axon as an electrical impulse.

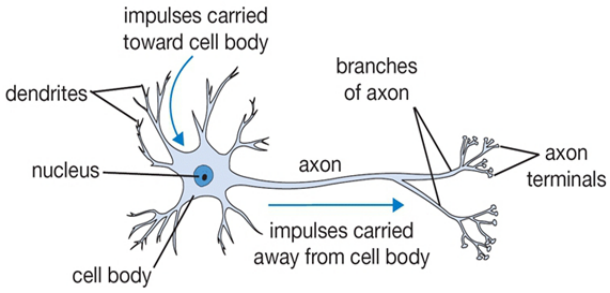

Fig. 2. *A biological neuron* (neuralpower)

1) Activation Function

In artificial neural network models, each neuron amount to its inputs, and then feeds the sum into a function. The activation function determines the neuron output. Commonly, the activation functions are also called as transfer functions. The net output of any node are computed by the activation function before feeding to the next layer. There are 3 typical types of activation functions; purelin, logsig and tansig (SIB, JONES, & SIDDARTH, 2013) as shown in equation (1), (2) and (3), respectively.

Purelin function can be defined as

$$f(n) = n \tag{1}$$

Logsig function is shown as

$$f(n) = \frac{1}{1 + e^{(-n)}} \tag{2}$$

Tansig function is derived as

$$f(n) = \frac{1 - e^{(-n)}}{1 + e^{(-n)}} \tag{3}$$

where n is the net input.

f is the activation function.

2) Architectures of Neural Networks

a) Feedforward Neural Networks

Feedforward neural networks compose of a series of layers. They are the most widely used architecture of neural networks. In feedforward neural networks, the first layer has a connection from the network input to output unit which are strictly feedforward. Consequently, each subsequent layer has a connection from the previous layer and then the final layer produces the network's output. A feedforward multilayered neural network can approximate a continuous function arbitrary well. Fig. 3 shows a single layer of neuron. It consists of one input and an output layer.

Fig. 3. Feedforward neural networks without hidden layer

Fig. 3 has the input vector, **x** and a weight vector, **w** in input layer. The net input vector, **n**, a bias vector **b** is contained. The net input vector can be deduced as Substituting equation (4) to an activation function, the output is calculated as

$$y=f(wx+b) \tag{4}$$

b) Training algolithim

In a learning network, a procedure for modifying the weights and biases of network can be referred to as training algorithm. There are three to adjust weight namely, gradient descent algorithm (GDA), gradient descent with momentum algorithm (GDMA) and Levenberg-Marquardt algorithm (LMA).

Gradient descent algorithm is based on the first-order derivative of objective error function. Let $E(\mathbf{w})$ be objective error function. To find the minima in error space, gradient vector**,** $\mathbf{g}$ of $E(\mathbf{w})$ can be defined as (Bordes, Bottou, & Gallinri, 2009)

$$\mathbf{g} = \frac{\partial E(\mathbf{w})}{\partial \mathbf{w}} \tag{5}$$

Applying the gradient descent to the weight vector, the direction is opposite the gradient vector. GDA updates the new weight vector at iteration, k as equation (6)

$$\mathbf{w}_{k+1} = \mathbf{w}_k - \alpha \mathbf{g}_k \tag{6}$$

where k is the iterative number
α is the learning rate
$\mathbf{g}_k$ is the gradient with respect to the weights.

In the iteration, weight may oscillate. If the oscillation is large then weight must be updated. Since the new weight, $\mathbf{w}_{k+1}$ depends on the past weight, $\mathbf{w}_k$ and the change ($\Delta\mathbf{w}_k$). To fulfill this requirement, $\beta\Delta\mathbf{w}_k$ is added into equation (6), it is called GDMA. $\mathbf{w}_{k+1}$ is defined as

$$\mathbf{w}_{k+1} = w_k - \alpha\mathbf{g}_k + \beta\Delta\mathbf{w}_k \quad (7)$$

where $\Delta\mathbf{w}_k$ is a weight change of the previous step
β is the momentum parameter.

Levenberg Marquardt algorithm outperforms the gradient descent and conjugate gradient methods for medium size of non-linear least squares problems (Lourakis, 2005). LMA finds the minimum of a function that is expressed as the sum of squares of non-linear real-valued function. LMA to update new weight vector can be obtained as follows

$$\mathbf{w}_{k+1} = \mathbf{w}_k - (\mathbf{J}_k^T\mathbf{J}_k + \mu\mathbf{I})^{-1}\mathbf{J}_k^T\mathbf{e}_k \quad (8)$$

where
μ is the scalar factor
k is the number of iteration
$\mathbf{J}$ is the Jacobian matrix
$\mathbf{e}$ is the vector of network errors.

C. Mixtures Design

Mixtures design is a one of factorial experimental design. It is different from other types of experiment design because the percentage of a component increase to 100%. The increasing level of constituent can balance the proportion of the mixtures. Following experiment design, ANOVA models are widely used based on factorial design. The regression analysis is mainly used, linear, quadratic and cubic response surfaces that are assumed in dependence on the mixture components. In a mixture experiment, the factors are different components of a blend to optimize components for example the tensile strength of stainless steel and the interesting factors which might be iron, copper, nickel and chromium in the alloy. Moreover, gasoline, soaps or detergents, beverages, cake mixes, soups and so on are optimized either (Rasch, Pilz, Verdooren, & Gebhardt, 2011).

3. PROPOSED METHOD

A. Mixture process

Mixture process is considered the factors that affect to talcum pellet. The components between water and mineral talcum are optimized for forming process to reduce the broken and isolated. Let input be mixtures of water and mineral talcum and output be weight of talcum pellet. The yield under two variables is defined as equation (9).

$$Yield(\%) = \frac{Output(kg)}{Input(kg)} \times 100 \quad (9)$$

B. Experimental component

In this paper, Table I shows the cases of the components of mineral talcum. The components are from the talcum process in the real factory in Uttardit province.

TABLE I. EXPERIMENT CASES OF MIXTURE DESIGN

Trial	Component (%)	
	Water	Mineral talcum
1	25	75
2	10	90
3	17.5	82.5
4	21.25	78.75
5	13.75	86.25
6	17.5	82.5

Table II shows trials, percentage of components which compose of talcum and water and percentage of each replication (Rep.) in yield. The collection data of talcum pellet process are shown as 1-5 trials. In trial 6, it replicates in a center.

TABLE II. RESULT OF YIELD FROM MIXTURE DESIGN

Trial	Component (%)		Yield (%)		
	talcum	water	Rep. 1	Rep. 2	Rep. 3
1	75	25	63.19	60.31	64.80
2	90	10	63.39	71.85	68.62
3	82.5	17.5	81.59	80.33	78.70
4	78.75	21.25	72.99	74.99	71.70
5	86.25	13.75	82.40	85.81	86.45
6	82.5	17.5	83.21	80.55	80.41

C. Design neural network model

In this paper, feedforward neural networks with backpropagation were designed to find the optimal components of mineral talcum and water. Supervised learning algorithm was applied that is GDA, GDAM and LM. Table III shows the experiment cases of ANN model for 18 models which have involved topology, transfer function and training algorithm.

TABLE III. EXPERIMENT CASES OF NEURAL NETWORK MODEL

Model	Topology	Transfer Function	Training Algorithm
1	2-5-1	purelin	traingd
2	2-5-1	purelin	traingdm
3	2-5-1	purelin	trainlm
4	2-5-1	logsig	traingd
5	2-5-1	logsig	traingdm
6	2-5-1	logsig	trainlm
7	2-5-1	tansig	traingd
8	2-5-1	tansig	traingdm
9	2-5-1	tansig	trainlm
10	2-10-1	purelin	traingd
11	2-10-1	purelin	traingdm

12	2-10-1	purelin	trainlm
13	2-10-1	logsig	traingd
14	2-10-1	logsig	traingdm
15	2-10-1	logsig	trainlm
16	2-10-1	tansig	traingd
17	2-10-1	tansig	traingdm
18	2-10-1	tansig	trainlm

TABLE IV. PARAMETERS OF NEURAL NETWORK MODEL.

Training parameter	Value
Maximum number of epochs to train	1000
Minimum value of performance function	10^{-9}
Minimum value of gradient, g	10^{-7}
Initial factor parameter, μ	0.001
Decreasing factor of μ, $\Delta^{-}\mu$	0.1
Increasing factor of μ, $\Delta^{-}\mu$	10
Maximum value of μ, max μ	10^{10}

D. Performance of neural network *model*

Mean square error (MSE) is used to measure the performance of neural network model (Prechadet & Luksiri, 2011). It can be define as

$$E_{MSE} = \frac{1}{N}\sum_{i=1}^{N}\left(Output_i - Observed_i\right)^2 \qquad (10)$$

where

$Output_i$ is the i-th network output

$Observed_i$ is the i-th target data

N is the total number of output nodes.

4. EXPEREMENTAL RESULTS

There are two topologies of neural network model were trained. In this proposed method, transfer functions, purelin, logsig and tansig, were applied to the models. Consequently, the ANN models included the training algorithms, traingd, traingdm and trainlm to adjust weights. The performance of the neural network model can be measure by MSE. The correlation between the model outputs and observed data can be represented in regression, R values. If R value of 1 means a close relationship then it 0 means a random relationship otherwise it is close to -1 which is no relationship. The experimental results are as shown in Table V.

TABLE V. *EXPERIMENT RESULT OF NEURAL NETWORK MODEL*

Model	Topology	Transfer Function	Training Algorithm	Regression (Training)	MSE
1	2-5-1	purelin	traingd	-0.258	0.0144
2	2-5-1	purelin	traingdm	0.617	0.0185
3	2-5-1	purelin	trainlm	0.455	0.0056
4	2-5-1	logsig	traingd	0.276	0.0069
5	2-5-1	logsig	traingdm	0.368	0.0057
6	2-5-1	logsig	trainlm	0.317	0.0155
7	2-5-1	tansig	traingd	-0.615	0.0101
8	2-5-1	tansig	traingdm	0.079	0.0271
9	2-5-1	tansig	trainlm	0.978	0.0007
10	2-10-1	purelin	traingd	0.413	0.0081
11	2-10-1	purelin	traingdm	0.893	0.0094
12	2-10-1	purelin	trainlm	0.491	0.0055
13	2-10-1	logsig	traingd	0.954	0.0080
14	2-10-1	logsig	traingdm	-0.432	0.0183
15	2-10-1	logsig	trainlm	0.965	0.0005
16	2-10-1	tansig	traingd	0.750	0.0061
17	2-10-1	tansig	traingdm	-0.554	0.0194
18	2-10-1	tansig	trainlm	0.882	0.0034

According to Table V, the experimental 2-5-1 topology in model number 1 to 9, was trained with traingd, traingdm and trainlm, involving transfer function that is purelin, logsig and tansig. R value of model 9 has 0.978 and MSE is 0.0007. R of model 9 are higher than other models. In addition, MSE is less than others. In model 10 to 18 based on the 2-10-1 topology, R value of model 15 is 0.965 which is higher than other models. Moreover, MSE, 0.0005, is less than others.

Figure 4 and 5 show observed yield and output yield of neural network models.

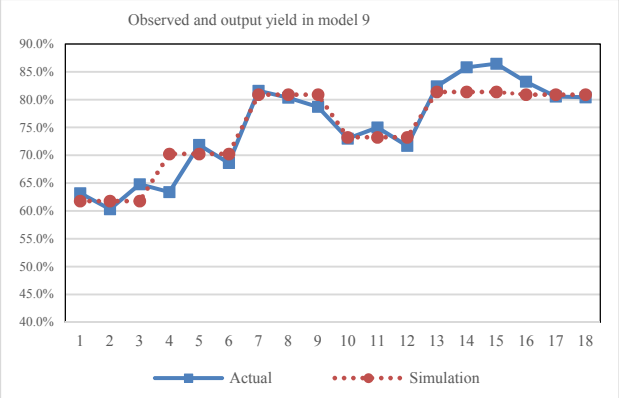

Fig. 4. *Observed and output yield in model 9*

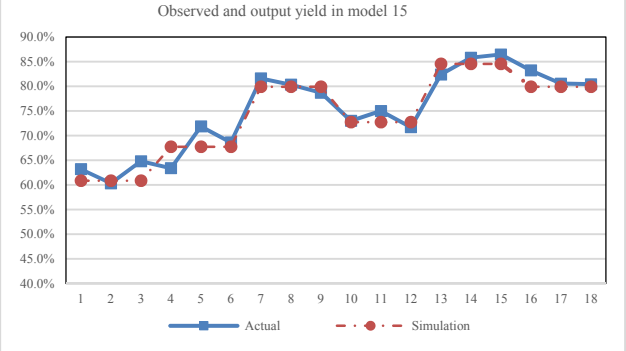

Fig. 5. *Observed and output yield in model 15*

5. CONCLUSIONS

In this paper, neural network models are applied to optimize the mineral talcum and water in mixture design. There are presented 18 models. Model 9 has 2-5-1 topology which is trained by Levenberg Maquardt algorithm and has transfer function in *tansig* function. The correlation in experimental results, model 9 and model 15 have a small difference of R value, only 0.013. It shows that model 9 has close relationship than model 15. Considering the performance of neural network models between model 9 and model 15 having a small difference MSE, however the performance of model 15 is better than mode 9. As a result, the neural network models to optimize mineral talcum components for

mixture design that is model 15. Implementing the neural network model, the model 9 and model 15 can provide the optimal components for mineral talcum process that produce the mineral talcum pellet with machine in Uttaradit province. It will increase accuracy and productivity. Moreover, it helps production plan and defines standard of mixture.

REFERENCES

[1]. C. Macleod, G. Dror and G. Maxwell, "Training Artificial Neural Networks Using Taguchi Methods," Artificical Interigence Review, pp. 177-184, 1999.

[2]. M. . S. Adroera, X. . L. Parrab, I. B. Corralc and J. . V. Calvetca, "Indirect model for roughness in rough honing processes based onartificial neural networks," *Precision Engineering,* pp. 1-9, 2015.

[3]. A. Yadollahi, E. Nazemi, A. Zolfaghari and A. M. Ajorloo, "Application of artificial neural network for predicting the optimal," Progress in Nuclear Energy, vol. 89, pp. 69-77, 2016.

[4]. S. Ozsahin, "Optimization of process parameters in oriented strand board," *Springer-Verlag Berlin Heidelberg,* vol. 71, p. 769–777, 2013.

[5]. D. J. Sarma and S. C. Sarma, "Neural Networks and their Applications in Industry," *Bulletin of Information Technology,* vol. 20, pp. 29-36, 2000.

[6]. neuralpower, "Integreat Electricity Demand and Price Forecasting," [Online]. Available: http://www.neuralpower.com/technology. [Accessed 7 October 2016].

[7]. P. Sib, S. A. Jones and P. Siddarth, "Analysis Of Different Activation Functions Using Back Propagation Neutral Networks," *Journal of Theoretical and Applied Information Technology,* vol. 47, no. 3, pp. 1264-1268, 2013.

[8]. A. Bordes, L. Bottou and P. Gallinri, "SGD-QN: Careful Quasi-Newton Stochastic Gradient Descent," *Journal of Machine Learning Research,* vol. 10, pp. 1737-1754, 2009.

[9]. M. . I. A. Lourakis, "A Brief Description of the Levenberg-Marquardt Algorithm Implemened," *Institute of Computer Science,* pp. 1-5, 2005.

[10]. D. Rasch, J. Pilz, . R. Verdooren and A. Gebhardt, "Optimal Experimental Design with R," *Journal of Statistical Software,* vol. 43, 2011.

[11]. S. Prechadet and C. Luksiri, "Prediction of Silicon wafer Lapping Time by Artificial Neural etwork," *Engineering Journal Kasetsart,* vol. 77, pp. 1-11, 2011.

Automatic Amplifier Gain Setting for Hearing Test Applications

K. Meesawat

Manuscript received August, 2016
Revised December, 2016

ABSTRACT

Hearing test applications for smart phones become more popular recently. They could be used for clinical screening purpose. But because of a vast variety of the smart phone hardware, their accuracies have been questioned. This article presents a design of an automatic amplifier gain setting for the hearing test application. The hearing test application shall consist of two stages namely the calibration stage, and the hearing assessment stage. This work relates only to the calibration stage. During the calibration stage, the device reads the reference level of the test signal, then calculate and set the required gain to its amplifier thus the headphones will produce the reference sound level. The device consists of a peak detector circuit, a microcontroller, a digital potentiometer, and an amplifier. The device works as expected, but the results shows that the set gain is precise but not accurate. The causes of inaccuracies are from the components tolerances, the low voltage power supply, and the operational amplifier headroom. However, the device can reduce the sound pressure dislocation from approximately 20 dB SPL to 3.5 dB SPL at worst and 1.5 dB in average.

Keywords: *Hearing test, smart phone, gain control*

1. INTRODUCTION

Hearing is a vital human perception. Hearing loss could affect one's life quality in various ways, such as learning/working opportunity, personal relationship, and especially, life safety. Untreated hearing loss might lead to other health problems, e.g. depression, social isolation, and fatigue [1]. The first step of the hearing loss treatment is the hearing assessment or the hearing test. Because of the standard hearing assessment using the clinical audiometry is a time-consuming process, using the smart phone applications or Apps is a good alternative for self-assessment hearing test. Noted that, these smart phone applications shall not replace the standard audiometry conducted by professional audiologists. Rather, they can be useful for the initial screening [2] which is defined as a pass/fail procedure to identify individuals who require further assessment [3]. The screening process can reduce the number of patients in the audiometry queue.

However, the accuracies of the applications have been questioned [4] .From electrical point of view, the sources of inaccuracy are different audio output levels and output impedances among smart phone models, and different sensitivities and input impedances among headphones used .

A possible solution is inserting a device between the smart phone audio output and the used headphone .that adjusts its gain thus its output reaches the necessary level This device receives the headphone sensitivity from users, reads the output level from the smart phone during the calibration stage, calculates the necessary gain, and adjusts the amplifier gain accordingly. With a less hardware dependent output signal level, the hearing test smart phone application will be more reliable.

2. LABORATORY SUREWAY

A laboratory survey on output level and output impedance has been conducted .It was possible to acquired only 4 smart phone models in this survey .The survey objective was only to demonstrate the variety of the smart phone hardware configurations .An application called "Frequency Sound Generator"[1] has been used to generate a set of test signals .The test configuration is shown in Fig .1 .The software generated a pure tone with its maximum level at the frequency of 250, 500, 1000, 2000, and 4000 Hz, respectively .All volume settings were set to their maximum .Each model was tested twice . The audio output port was loaded with R_L = 100 ohms and with R_L =220 ohms .The voltages across R_L were measured. Noted that the voltages across R_L did not vary with frequency.

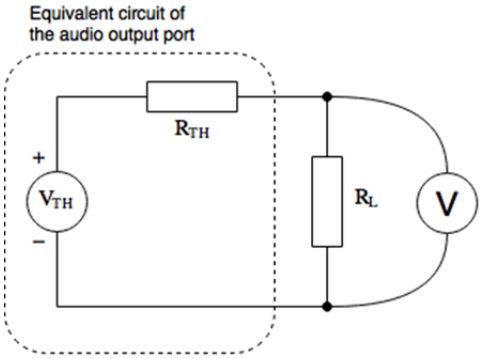

Fig .1 *Audio output port test configuration*

K. Meesawat is with the Department of Electrical Engineering, Faculty of Engineering, Khon Kaen University, Thailand, Mail: mkittiphong@kku.ac.th

Table 1 shows that measured voltages across R_L under both conditions .By solving the linear equation systems, the parameters of the Thévenin's equivalent circuits of the smart phone audio output ports are tabulated in Table 2. This shows that the output level and output impedance of different smart phone models are diverse. The actual brand names and models were omitted to avoid legal issue.

Table 1 Audio output level of the tested smart phones

Model	V_{RL} @ R_L=100 Ω	V_{RL} @ R_L=220 Ω
A	0.619 V_{RMS}	0.735 V_{RMS}
B	0.700 V_{RMS}	0.810 V_{RMS}
C	1.02 V_{RMS}	1.04 V_{RMS}
D	0.257 V_{RMS}	0.294 V_{RMS}

Table 2 V_{TH} and R_{TH} of the audio output port of the tested smart phones

Model	V_{TH}	R_{TH}
A	0.873 V_{RMS}	41 Ω
B	0.930 V_{RMS}	33 Ω
C	1.05 V_{RMS}	3.2 Ω
D	0.334 V_{RMS}	30 Ω

A market survey on headphone sensitivity and impedance has also been conducted .The sensitivities and the impedances of 4 different headphone models from the survey are presented in

Table **3**. The actual brand names and models of the headphones were also omitted here for the same reason.

Table 3 Sensitivity and impedance of headphones

Model	Sensitivity (dB SPL/mW)	Impedance (Ohm)
1	96	34
2	98	24
3	100	35
4	105	16

To clarify the situation, let us compare the following 2 scenarios .In the first scenario, the user uses the smart phone A with the headphone 1 .In the second scenario, the user uses the smart phone C with the headphone 4. It can be calculated that the scenarios will produce the sound pressure level of 102.6 dB SPL and 121.8 dB SPL . The difference from these scenarios is almost 20 dB .This hardware combination is not known beforehand to the programmer thus it is not possible to control the sound level exposed to the user.

3. DESIGN AND IMPLEMENTATION

3.1 System design

The operations of the device can be described as follows. Assume that the full-scale audio signal refers to a sound level of 110 dB SPL. At first, the user enters the sensitivity of the selected headphone into the device via its user interface. After that, during the calibration period, the application shall send the full-scale signal to the audio port. The device reads the signal level using a peak detector circuit, and calculate the necessary gain from the full-scale signal level and the headphone sensitivity using a microcontroller, so that the headphone will produce a sound level of 110 dB SPL. Then, the device adjusts its amplifier gain to the target value. Hereafter, the device keeps its gain constant along the assessment period.

Fig. ***2*** shows the block diagram of the device.

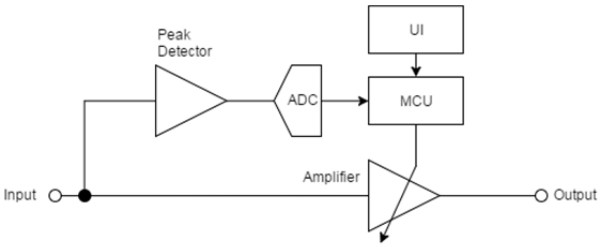

Fig. 2 *Block diagram of the automatic gain adjustment device.*

3.2 Circuit implementation

The schematic of the circuit is shown in Fig. 3. For the sake of simplicity, the microcontroller platform is omitted. There are 3 main components in the circuit, namely peak detector, amplifier, and microcontroller and its peripherals. These components are described in the following sections.

3.2.1 Virtual ground

For the user's convenience, the circuit shall be used with a single rail power supply. But the circuit utilizes a few Op Amps which require a dual rail power supply, thus a virtual ground is needed. The Op Amp U1 gives a virtual ground node. The virtual ground level is read by the microcontroller ADC (A2) and is used as a reference value.

3.2.2 Peak detector

The peak detector employed in this circuit is a simple precision diode using an Op Amp U2. Even though it has been criticized that the circuit may not work properly at high frequency [5], it is good enough because of the device will work within audio frequency. The resistor R3 acts as a load seen by the smart phone. The output of the peak detector is fed to the microcontroller ADC (A1).

3.2.3 Amplifier

Based on hardware information available in Table 2 and

Table **3**, the minimum and the maximum device gain for the smart phone-headphone combinations thus

the sound pressure level of the headphone output reaches 110 dB SPL are approximately 0.2 and 3. U3 is for an inverting amplifier.

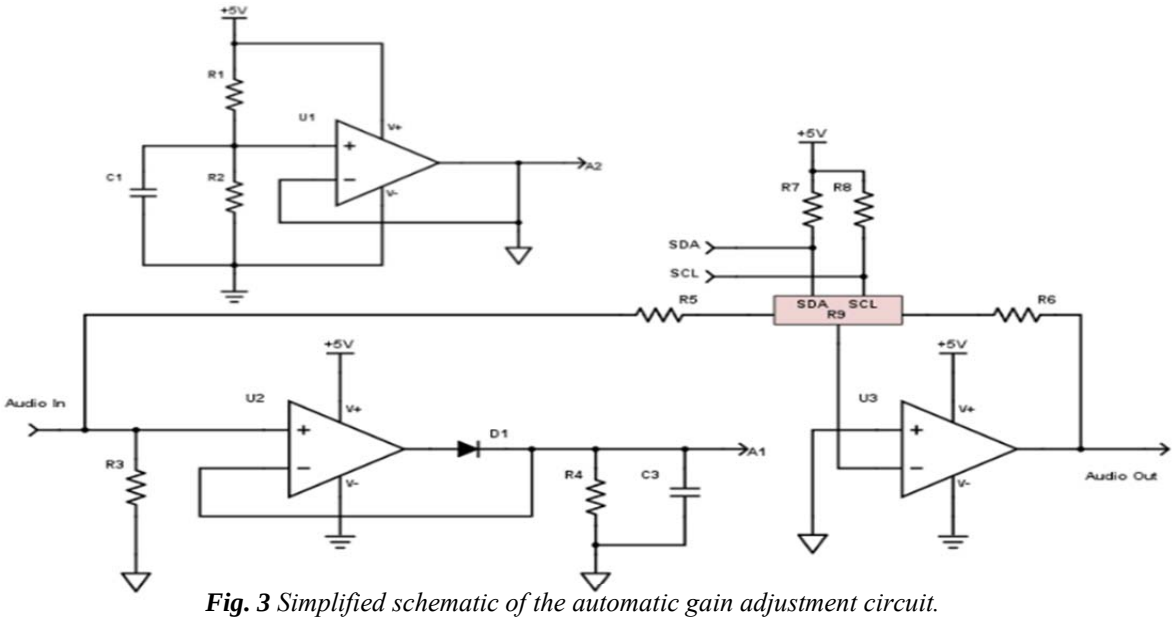

Fig. 3 *Simplified schematic of the automatic gain adjustment circuit.*

The gain of the inverting amplifier is designated by a digital potentiometer (R_D). The minimum and the maximum gain of the amplifier are set by R_5 and R_6. The magnitude of the device gain ($|A_v|$) can be expressed by Eq (1).

$$|A_v| = \frac{R_6 + kR_D}{R_5 + (1-k)R_D} \tag{1}$$

where k is the proportion of 1.0 of the digital potentiometer. The value k = 1.0 happens when the wiper arm of the potentiometer is located at the lower end of the potentiometer thus the resistance from the upper end to the wiper arm is 100%, and the resistance from the lower end to the wiper arm us 0% of the end to end value. With R_5 = 4.23 kΩ, R_6 = 3.03 kΩ, and R_D = 10 kΩ, the gains when k = 0.0 and k = 1.0 are 0.213 and 3.08, respectively. For any desired gain between 0.21 and 3.08, the proportion k can be determined by Eq (2). Engineers could use different resistance values if the range of implemented smartphone and the maximum SPL in the assessment differ.

$$k = \frac{A(R_A + R_D) - R_B}{(A+1)R_D} \tag{2}$$

The R_D is controlled by the microcontroller through the two-wire interface (TWI).

3.2.4 Microcontroller

The platform of the microcontroller used was Arduino UNO R3 for the sake of rapid prototyping .The microcontroller receives the sensitivity of the headphones via a user interface using the Arduino LCD keypad shield.

The module consists of a HD44780 compatible liquid crystal display (LCD) driver that works in 4-bit mode and 5 push button switches. The circuit configuration of the switches is shown in Fig. 4. Different button pushed can be detected via different voltage which is connected to the microcontroller ADC (A0). This keeps the number of the occupied pin low. Users adjust the headphone sensitivity and impedance by changing the digits on the display using UP, DOWN, LEFT, and RIGHT buttons. The SELECT button is pressed when the user satisfies the entered numbers.

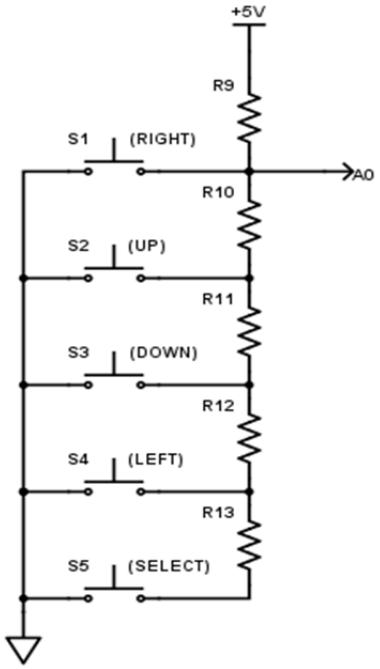

Fig. 4 *Switches configuration*

The microcontroller reads the peak of the signal from the peak detector circuit described in section 3.2.2 using its built-in 10-bit ADC. The read values are offset with the potential level of the virtual ground from section 3.2.1. After that, the averaged values of the peak values are used for the further calculations.

The target gain and the proportion k are then calculated. The microcontroller set the value of R_D through its TWI interface. Finally, the value of R_D is fixed hereafter for the rest of the hearing test procedure. Fig .5 depicts the flowchart of the program.

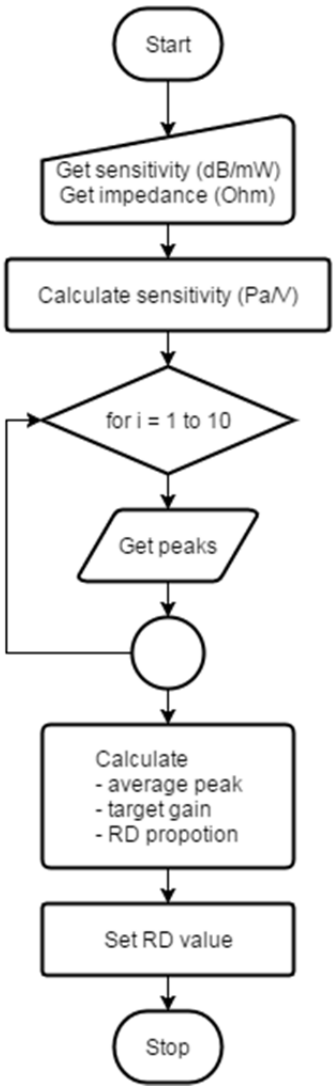

Fig .5 *Flowchart of the automatic gain adjustment program.*

4. EXPERIMENT AND RESULTS

An experiment was setup to visualize the device's performance .The device was fed by a 1 kHz sinusoidal signal with its amplitude varied from 0.2 V to 1.5 V .The detected peaks, and the actual gains were recorded. The detected peaks were the peak value read by the microcontroller, and the actual gains were the voltage gain measured directly from the amplifier .These procedures were repeated for 4 headphones specifications which are listed in Table 3, Experimental results are shown in table 4. Table 5 presents the sound pressure level produced by the listed headphones if they were used with this automatic gain adjustment device when the target sound pressure level was set to 110 dB SPL .The average error of the sound pressure levels was 1.5 dB. It was not possible to measure the actual sound pressure levels of the headphones in our laboratory because it requires a precision microphone and a standard ear simulator as described in [6] which are too expensive.

Table 4 Detected peaks, calculated gains and actual gains of the device

V_{in}	Detected Peak	Actual gain Headphone no.			
(V)	(V)	1	2	3	4
0.2	0.28	3.08	2.18	2.08	0.79
0.3	0.39	2.38	1.57	1.51	0.56
0.4	0.51	1.84	1.19	1.22	0.44
0.5	0.62	1.49	0.99	0.96	0.36
0.6	0.74	1.25	0.85	0.84	0.30
0.7	0.86	1.07	0.72	0.71	0.26
0.8	0.94	1.00	0.65	0.62	0.23
0.9	1.08	0.85	0.58	0.55	0.21
1.0	1.18	0.80	0.52	0.49	0.21
1.1	1.26	0.75	0.49	0.46	0.21
1.2	1.29	0.73	0.48	0.46	0.21
1.3	1.32	0.72	0.47	0.45	0.21
1.4	1.32	0.71	0.46	0.45	0.21
1.5	1.34	0.70	0.46	0.44	0.21

Table 5 Calculated sound pressure level of each headphone

V_{in}	Cal. Sound pressure level (dB SPL) Headphone no.			
(V)	1	2	3	4
0.2	106.5	107.0	106.9	106.9
0.3	107.8	107.7	107.7	107.5
0.4	108.0	107.8	108.3	107.9
0.5	108.1	108.1	108.2	108.1
0.6	108.2	108.3	108.6	108.1
0.7	108.2	108.2	108.5	108.2
0.8	108.7	108.5	108.5	108.3
0.9	108.4	108.6	108.5	108.5
1.0	108.7	108.5	108.4	109.4
1.1	109.0	108.8	108.6	110.2
1.2	109.5	109.4	109.4	111.0
1.3	110.1	109.9	109.9	111.7
1.4	110.6	110.4	110.5	112.3
1.5	111.1	111.0	111.0	112.9

5. DISCUSSION

Table 4 shows that there was some error in the detected peaks .A source of error was the output offset of the detector circuit .It can be deducted that the circuit non-linearity was also a source of error because the recorded

offsets were not constant along the table .Finally, at V_{in} > 1.2 V, the peaks detected were almost constant around 1.32 V .It was an evidence that another source of errors was the output saturation caused by the Op Amp headroom.

Table 5 reveals that the calculated sound pressure levels were dislocated .The maximum error was 3.5 dB . Obviously, one source of errors was the errors in the peak detected described above .Other possible causes are the tolerance of the components values, and the quantization error of the digital potentiometer. Some of the errors could be reduced by using circuit techniques such as described in [7] with a cost of stability control.

6. CONCLUSION

This article presents a design and development of a simple automatic gain setting circuit to be used with the hearing test application for smart phone .The circuit employs a peak detector, a microcontroller, a LCD and keypads module, a digital potentiometer, and an amplifier .The device works as expected but with some uncertainty in measured gains thus the calculated sound pressure levels of the headphones were dislocated.

Even though there were dislocations in the calculated sound pressure levels, but the level difference as described in the section was reduced from almost 20 dB to 3.5 dB at worst, and to 1.5 dB in average .Better circuit design techniques and lower headroom Op Amps could improve the performance of the device, but with a cost of expense, component count, power consumption, and probably, the difficulties to control the circuit stability. Alternatively, a signal path from the amplifier output could be fed back to the remaining microcontroller ADC thus a feedback control system can be established.

REFERENCES

[1] A. Tonkin, “Hearing loss treatment,” Healthy Hearing, published on 15 Oct 2015, Retrieved 19 June 2016, from http://www.healthyhearing.com/help/hearing-loss/treatment.

[2] J. C Wang, S. Zupancic, C. Ray, J. Cordero, and J. C. Demke, “Hearing Test App Useful for Initial Screening, Original Research Shows,” Hearing J., vol. 67, issue 10, pp. 32 – 35, Oct, 2014.

[3] D. A. DeBonis, and C. L. Donohue, *Survey of audiology*: Fundamentals for audiologists and health professionals, Pearson, 2004.

[4] R. Nast, “Hearing Health-Care Apps for Mobile Devices: An Update,” Audiology Today, vol. 27, no. 2, pp. 22 – 28, Mar/Apr 2015.

[5] D. Ducu, “Op amp rectifiers, peak detectors and clamps,” Microchip Technology Inc., Appl. Note AN1353, 2011.

[6] S. Jønsson, A. Matthisson, and C. Borg, “Improving Telephone Handset Performance,” Brüel & Kjær, Appl. Note BO0455, 1997.

[7] Audio gain control using digital potentiometers, Maxim Integrated, Tutorial AN1828, 2002.

Analysis of Energy Consumption and Behavior of Elevator in a Complex Residential Building

S. Marsong and B. Plangklang

Manuscript received October, 2016
Revised December, 2016

ABSTRACT

Elevator is currently a common used electric appliance in most midrise and high rise building, Energy consumption behavior of Elevator is crucial to be investigated in order that the collected data can be a useful guideline for future energy conservation. In this paper, the author investigated a selected elevator in a building in Thailand. The sample is the apartment residential building of elevators which were installed and operated. The sample was categorized based on elevator type and building type. The obtained data was compiled as load profile. The analysis result ranged by different sessions of day demonstrated the elevator using behaviors. The factor value indicated that elevator can be load factor impacting the overall energy consumption. This information as guideline is worthy for future energy conservation by using of EERU.

Keywords: *EERU; Energy; Traffic pattern.*

1. INTRODUCTION

Research about the amount of energy consumed in the buildings demonstrates that the energy consumed by the elevators constitute between 5 and 25% of the total energy consumption of the building [1]. In operation, lift control systems adapt to changing demands based on their designers' understanding of passenger traffic patterns.

Control strategies appropriate to the current traffic pattern (e.g. up peak, down peak algorithms) can improve performance significantly [2]. Thus, it becomes highly important to accurately estimate the energy consumption highly important to accurately estimate the energy consumption of the elevators and to analyze, for the ones to be built or to be restored. In this study, elevator traffic analysis of an existing building is performed, and running time energy consumption of the elevator is monitored. The energy consumption varies depending on the building characteristics, level of density of people [3].

The first of samples residential building was selected, Overall energy consumption of this elevator system was summarized. Energy usage data was extracted from the elevator data communication system with elevator diagnostics tool for propose of monitoring elevators energy usage for a continuous limited period. For better understanding the elevators energy consumption, the recorded data was analyzed to identify the elevators energy quality to see how energy consumption varied in 1-day and 1-week cycle. The analysis result for elevator energy consumption quality was instrumental in respect of the power generation management so that the energy users can maximize the effectiveness of elevator usage.

S. Marsong and B Plangklang are with the Department of Electrical Engineering, Faculty of Engineering, Rajamangala University of Technology Thanyaburi, Thailand. Mail: supapradit_m@mail.rmutt.ac.th, boonyang.p@en.rmutt.ac.th

Fig. 1 *Unixx Pattaya illustrations*

PROPERTY NAME: Unixx South Pattaya
DEVELOPER: Raimon Land Unixx Co., Ltd.
PROPERTY TYPE: Freehold Condominium
TOWERS: Single tower with 2 wings, 45 and 45 stores
TOTAL LAND AREA: 7-0-16 Rai (11,000 sq.m.)
TOTAL NUMBER OF UNITS: 1,207 units (approx.)
TYPES OF UNITS: Studio / 1-bedroom / 2-bedroom

2. THEORY AND IMPLEMENTATION

A. Traffic analysis

Applicable codes and Standards have taken in to account. Passenger traffic have been define in several type such as [4] [10].

1. *Incoming Traffic: Commercial Buildings (Offices)*
2. *Two-Way Traffic: institutional buildings (School, Hospital)*

3. *Outgoing Traffic: Residential Building (Apartment).*
   a) *Waiting time definition Round Trip Time: – Time from the moment car starts up to the next time it starts up.*
   b) *Interval: (Time between elevators) – Up-Peak round trip time divided by number of lifts in the group.*
   c) *Performance Factors .*

Quality Factor => Waiting Time
Quantity Factor=> Handling Capacity

d) Estimated Travel Time (T1)

$$T1 = 2*H / \varsigma$$

Where T1: Total Return Travel Time (s)
H: Travel Height (m)
V: Rated Speed (m/s)

e) Estimated Waste Time (T2)

$$T2 = (A\pi + 1) * \varsigma / \Psi$$

Where: T2 (s): Acceleration and Deceleration time
AP: Probable stoppage of the car it is function of the population and rated load
V (m/s): Rated Speed (m/s2):
Acceleration = deceleration Jerk (m/s3) is excluded in the manual calculation

f) Round Trip Time: Up Travel Cycle

- Worst Case: Arrival upon lift leaving
- Starting/Acceleration
- Running on rated speed
- Deceleration/stopping
- Door Opening
- Exit of the Passengers
- Door Closing
- Starting/Acceleration
- Similar Process
- Exit of the last passenger

g) Estimated Door Time (T4)

$$T3 = K1 * (AP + 1) \quad (3)$$

Where – T3 (s): Total Door closing and opening time
K1 (s): is the time of door opening and closing including waiting time. It is a function of the door type and size
AP: Probable stoppage of the car it is a function of the population and rated load

h) Estimated Passenger Time (T4)

Hospital (Two-way)

- HC: 12%
- Interval: 30 to 50 sec
- Inefficiency: 5%
- Classrooms:
- HC: 25 to 40%
- Interval: 40 to 50 sec
- Inefficiency: 0%

i) Additional Considerations

- Highest Reversal Floor
- Up-Peak with down traffic
- Restaurants on the top floor (noon traffic)
- Parking areas in Basements

j) Handling Capacity

Handling Capacity is: The percentage of population an elevator group can transport in five minutes [10].

$$HC = N * CLF * PC * 300/ RRT \quad (4)$$

Where
N: number of lifts in the same group
(1) CLF: Car Loading Factor
PC (passengers): Rated Load
RRT (s): Round Trip Time per lift 300 s (5 minutes)

Table 6 Recommended Car Characteristic

(2) ***Type of Building***	***Capacity (Kg)***	***Door width (cm)***
Average Office Building	1600	120 (CO)
Large Prestigious Office Building	1800	120 (CO)
Hotel Building (5*)	1600	120
Prestigious Large Apartment Building	1150	110
Hospitals	2200	140
Schools/Universities	2750	150

k) Load Factor

Average to maximum wattage ratio for load in time session examined [6].

$$Peak\ power\ of\ load = \frac{Average\ power\ of\ load}{Load\ Factor} \quad (5)$$

l) Annual Usage Hour

Average to maximum wattage ratio for load in time session examined.

$$\text{h/yr} = \frac{Used\ hours\ in\ consider\ time}{Total\ hours\ in\ consider\ time} \times Total\ hours\ of\ year \quad (6)$$

m) Annual Usage Unit

Annual usage hour is referred to as number of use hours for load or electric appliance in 1-year period (h/yr)

$$\frac{kWh}{yr} = \sum(Average\ power\ [kW]\ x\ Hours\ /\ day)\ x\ Days\ /\ year \quad (7)$$

b. Building selection

Residential building 45 stories total number of units 1200 were selected for observation of their elevator

energy consumption. The Elevators and building characteristic are shown on table 2.

Table 7 *Elevator Data*

Residential Building	***units***
No.of Elevators (units)	4
Total Bldg Heigh (m)	136.5
Average Floor Heigh (m)	3.41
Total Population (per)	50
Number of floor (Floor)	45
Speeed (m/sec)	3.5
Capacity (kg)	1350
Door Open Time(S)	1.8
Door Close Time(S)	2.9
Car area m^2	3

3. DATA COLLECTION AND TOOLS

The elevator traffic data and the important of information such as running direction, passenger loads in percentage, trip measurements

a. Tool Connection

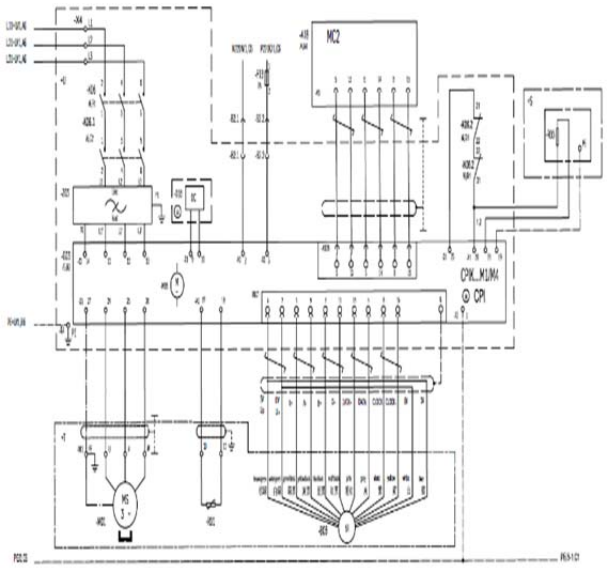

Fig. 2 *Drive Module and communication bus*

Fig.2 is show main block diagram of the elevator main in power drive and how it connected to communication system TCM-MC2 where elevator traffic data was collected from this modules.

b. CAN-Bus data connection

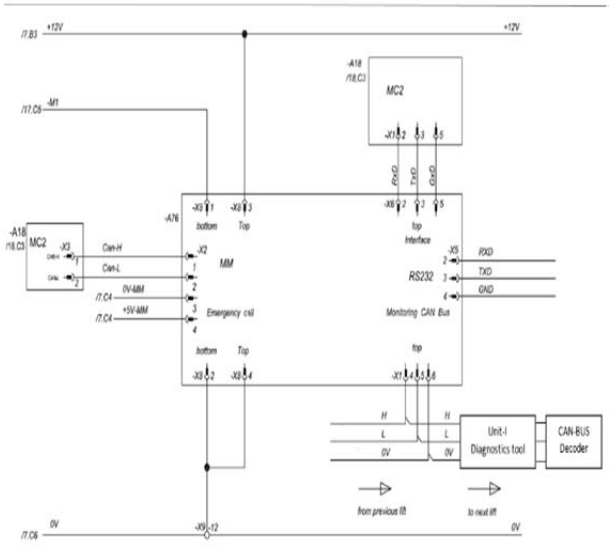

Fig. 3 *CAN-Bus*

Fig.3 is show can-bus diagram of the elevator which are connected to communication system although other elevator in the same group controller from can- bus data where we can connect the diagnose tools for data acquisitions.

c. Unit-I Diagnose tools

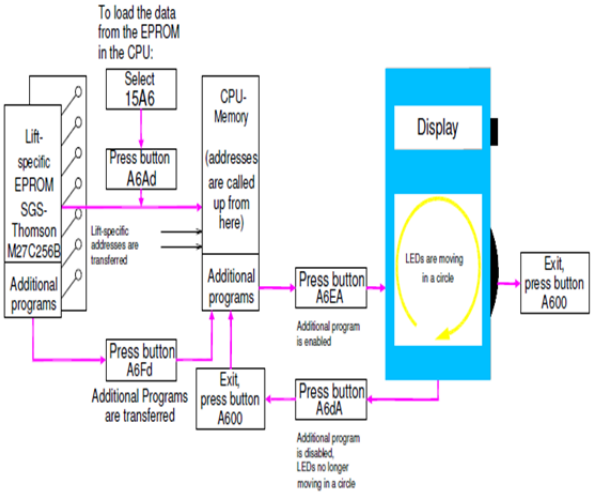

Fig. 4 *Diagnose tools*

Fig.4 is show connection diagram of diagnostics tool to an EPROM on the main controller which are maintain configuration and parameter of the elevator. Keys operating parameter are setting from unit-I tools.

d. Load-weighing device LMS1

Light emitting diodes	LED +5V LED RST	lights with proper voltage supply with +5V DC lights up approx. 1 s with a RESET.
Measuring	MP1: GND:	indicates voltage applied to A/D converter frame

(The measuring points are loadable with a digital multimeter)

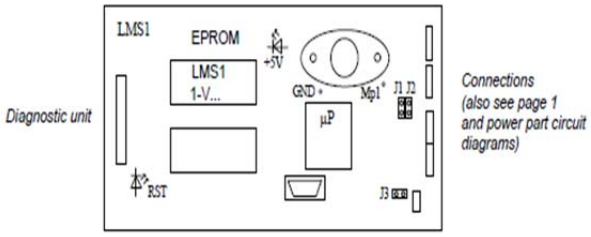

Fig. 5 *LMS1 Layout*

Fig. 5 is show the Plug in diagnostic unit and select with program selector and operate button address 1500 Plug CAN bus into plug X4. Activate matching resistor through jumper J3, if the load weighing Device LMS1 is the last data station in the bus system. Connect the load-weighing device LMS1 to the voltage supply. Light-emitting diode RST will light up intermittently during switching on.

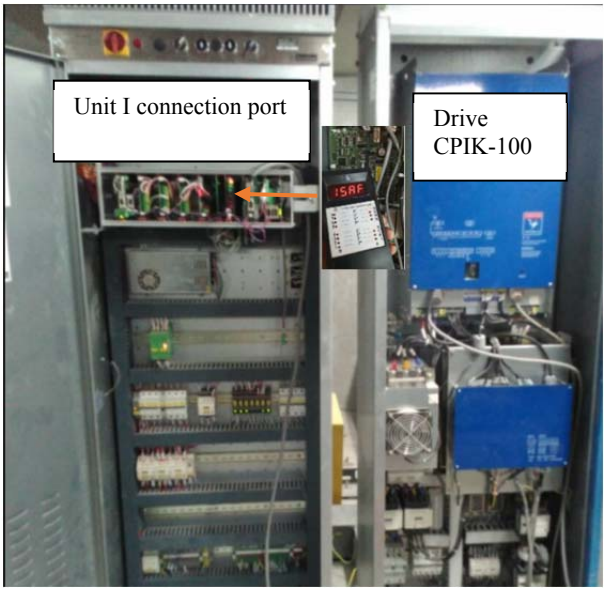

Fig. 6 *Tools connection*

Fig.6 is show connection of the unit-I to main controller and keep it inside the controller while recording the elevator traffic is in process 24hrs limited recording time is provided.

4. ANALYSIS

Load profile represents in line graph showing the overall building power demand of elevator usage, which data was derived from the internal memories and its internal measurement devices that wattage was read every 5 minute for the duration of 24 Hrs. of the sample building (residential). Continuous period in daily load curve as shown in Fig. 6 to Fig. 11

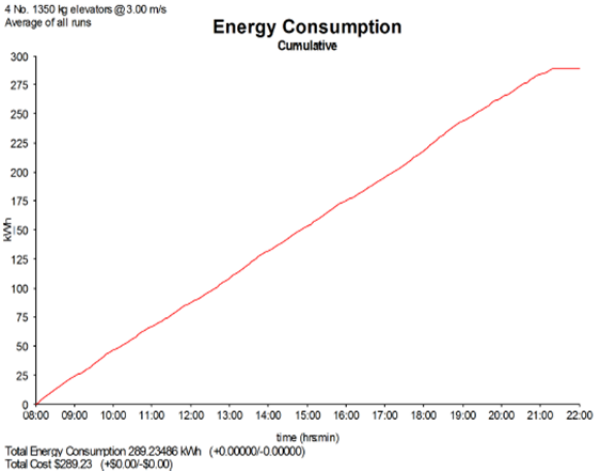

Fig. 7 *Accumulative Energy Consumption*

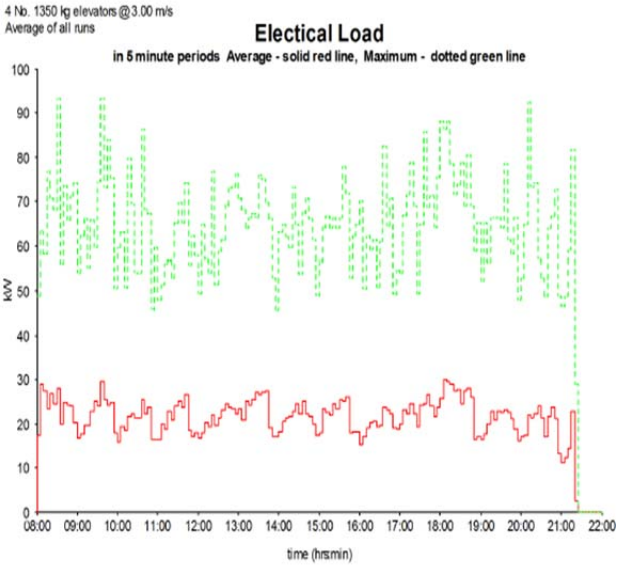

Fig. 8 *Average 5 Mins Electrical Load*

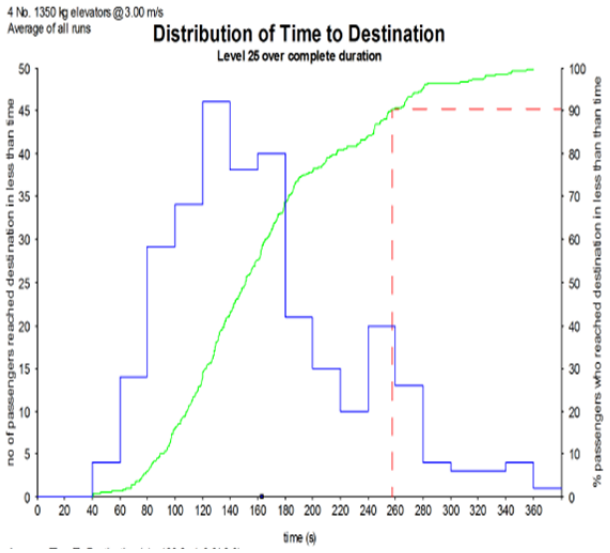

Fig. 9 *Distribution of Time to destination*

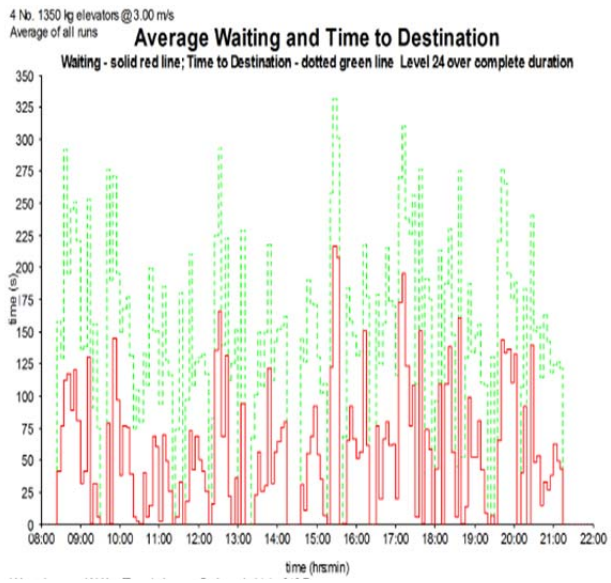

Fig. 10 *Average waiting time to Destination*

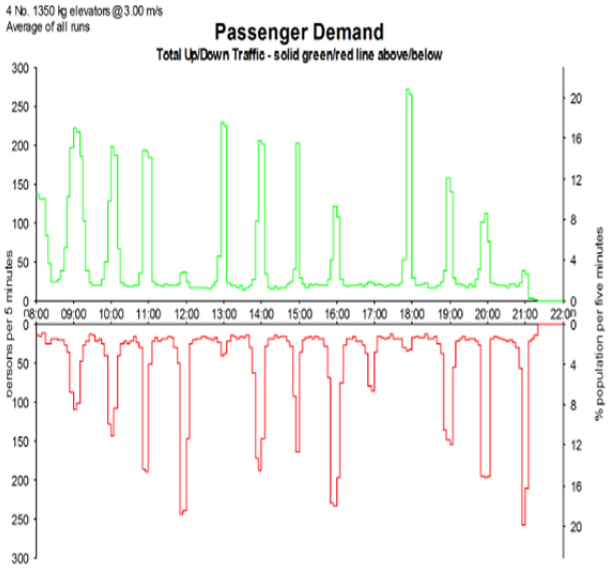

Fig. 11 *Total Up & Down Traffic*

4. CONCLUSION

The energy of the up-peak pattern is more important than other traffic patterns, because more energy is consumed during up-peak. Up-peak energy scheduling has a great significance for multi-elevator system efficient operation, and offers useful guidance to optimal scheduling under other traffic pattern in building. From the building sample is an outgoing traffic.

More energy is consumed under up-peak pattern than other traffic patterns because of the numerous upwards passengers.

This is due to the fact that the elevators go down empty during the up-peak traffic, the worst type of traffic, and that requires the counterweight to be pulled upwards resulting in energy consumption.

REFERENCES

[1]. H.M. Sachs, Opportunities for Elevator Energy Efficiency Improvements, American Council for an Energy-Efficient Economy (ACEEE), Washington, DC, 2005, April.

[2]. J. Liu, F. Qiao, L. Chang, The hybrid predictive model of elevator system for energy consumption Proceedings of the 2010 International Conference on Modeling, Identification and Control, Okayama, Japan, 2010, 17-19 Jul

[3]. A.D. Almeida, S. Hirzel, C. Patreo, J. Fong, E. Dutschke, Energy-efficient elevators and escalators in europe: An analysis of energy fficiency potentials and policy measures, Energy and Buildings 47 (2012) 151–158.

[4]. H. Hakala, M.L. Siikonen, T. Tyni, J. Ylinen Energy-Efficient Elevators for Tall Buildings 6th World Congress on Tall Buildings and Urban Habitat (2001, February/March)

[5]. C. Patrao, L. Rivet, J. Fong, A. Almedia Energy efficient elevators and escalators ECEEE (2009), pp. 803–813

[6]. Analysis of Energy Consumption and Behavior of Television in Resident Houses in Thailand, Boonyang Plangklanga *, Rak Skunpongb Procedia Engineering 8 (2011) 115–11920, December 2010

[7]. Performance analysis of an elevator system during up-peak

[8]. C.K. Chu, C.K.Y. Lin, S.S. Lam Hospital lift system simulator: a performance evaluator-predictor European Journal of Operational Research, 146 (2003), pp. 156–180

[9]. H.T. Duru, R. Demiröz Modern Energy Efficient Gearless Drive Elevator Systems Elevator Symposium, Izmir, Turkey (2009) 21-23 May

[10]. The Vertical Transport Handbook Edition 4th

Nonintrusive Load Monitoring (NILM) with Low Sampling Rate in Embedded System

S. Biansoongnern and B. Plangklang

Manuscript received October, 2016
Revised December, 2016

ABSTRACT

A Nonintrusive load monitoring (NILM) system is an energy demand monitoring and load identification system that only uses one instrument installed at main power distribution board. In this paper authors have used low sampling rate of monitored data to detect any change of power signal that obtained a 1 Hz sampling rate of active power from energy meter that read though RS485 with RTU Modbus protocol. Using 5 points of difference equation of steady-state real power to find event detection and using active and reactive power signatures to disaggregation. This paper point to five appliances including air conditioner television refrigerator rice cooker and electric iron. The results showed that the proposed system can disaggregation energy in accuracy 89.2% from total consumes of energy.

Keywords: *DC fault protection, fault analysis, MTDC grid, offshore wind farm.*

1. INTRODUCTION

In an electricity system of household, to identify status and to know the energy consumption of appliances there are usually voltage sensor and current sensor installed in each load that called intrusive load monitoring system [1[,[2]. A nonintrusive load monitoring (NILM) system is load identification system that only uses one instrument installed at main power distribution board. The system is better than traditional intrusive monitoring systems because the measuring of power consumption without having to install any instrument directly to appliances that mean to reduce the cost of sensors and installations. Significant savings in energy consumption can be achieved by improved energy management and real-time information on appliances in buildings [3]. Real-time energy consumption on appliances can be used to plan to improve efficiency of load such as cleaning air conditioner or defrost refrigerators. A continuous feedback on load power draw can lead to significant energy saving. One of the classification of NLIM is sampling rate that they rely on: very low sampling rate (1 h - 15 min), low sampling rate (1 min - 1 s) and high sampling rate (< 1 s) methods. Very low sampling rate methods are to get data from Automatic Meter Reading (AMR) that complies with 15, 30 and 60 minutes [4],[5]. Low sampling rate methods are to get data from smart meter with port communication that obtained data at a 1 Hz [6],[7]. High sampling rate data allows NILM algorithms to use more complex features including transients, current harmonics and voltage-current trajectory that get data from special meter [8]. The system uses a single energy meter of main point to obtain a 1 Hz sampling rate of active power that read though RS485 with RTU Modbus protocol. Using steady-state real power and reactive power (PQ) signatures to disaggregation. Fig.1 shows an electricity system of household with NILM embedded system that only uses one instrument installed at main power distribution board. The user interface can read all information from cloud by internet and direct read from NILM embedded system.

S. **Biansoongnern and B. Plangklang are** are with the Department of Electrical Engineering, Faculty of Engineering, Rajamangala University of Technology Thanyaburi, Thailand. Mail: boonyang.p@en.rmutt.ac.th

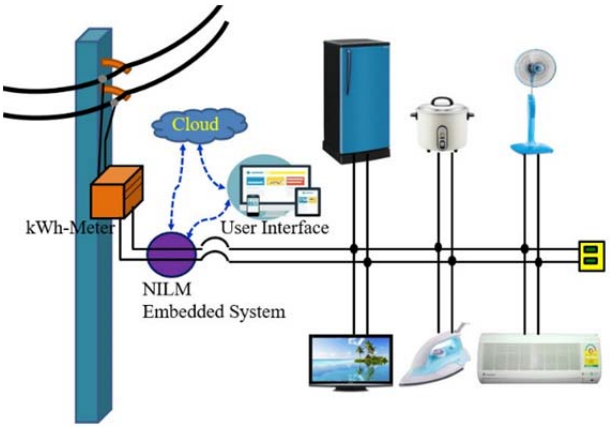

Fig. 1 *Electricity System of Household with NILM*

2. NONINTRUSIVE LOAD MONITORING

The main idea of nonintrusive load monitoring is to obtain appliance-specific information non-intrusively. The information is collected at the main input, and then disaggregated to obtain operational time and power draw information. Fig.2 shows an example of an aggregated power signal and the corresponding NILM solution [7]. The main signal consists with television fan and refrigerator signal. In this illustration, the reconstructed operational time of television is from 5:56 AM to about 8:40 AM with the power draw is about 58 W, fan is from 5:25 AM to about 8:50 AM with the power draw is about 46 W and refrigerator is on and off all day with the power draw is about 72 W. In this example, the appliances are modeled as on/off load that consume constant active power at a single steady state.

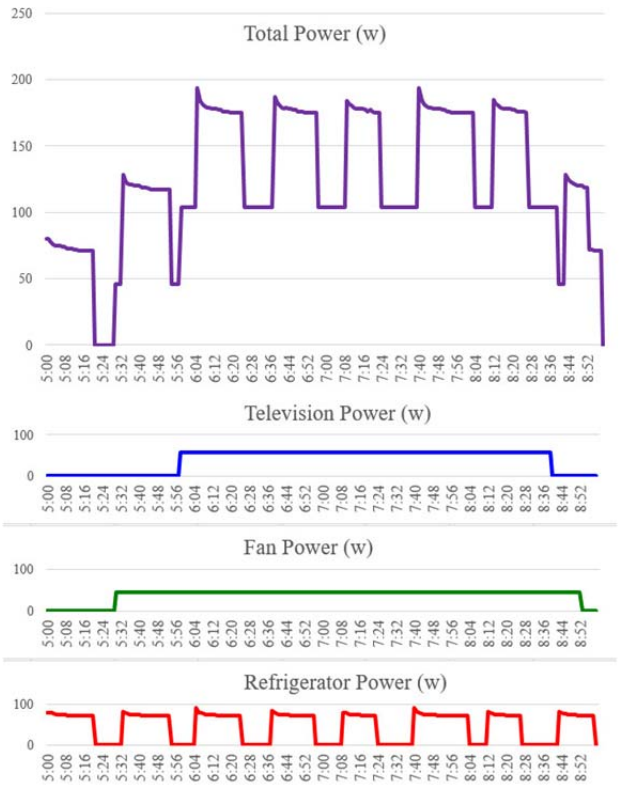

Fig. 2 *NILM Classified an Input Signal into Individual Appliances*

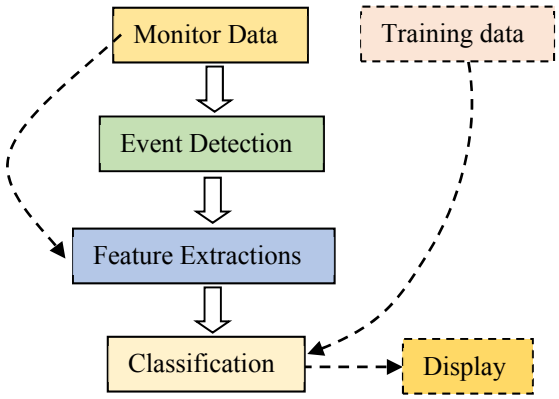

Fig. 3*. The Elements of NILM System*

NILM system elements can be divided into four main parts: monitor data, event detection, feature extractions and classification [9] and two minor: training data and display shown as Fig.3 [10]:

- Monitor Data: This part is hardware that used to measure and record data from instrument such as AMR smart meter.
- Event Detection: Detection part is software that used to detects the change of electricity data such as active power (P) and record time steps that indicates that this is a significant changes.
- Feature Extractions: Feature extractions is extraction some features out of those timestamps that read from main signal.
- Classification: Classification part is software that acts as disaggregation or grouped the electrical equipment used training data to classifier with timestamps.
- Display part is presentation of power consumption of electrical devices.

Training data is data set to classifier group of data into individual appliances.

3. DESIGN OF SYSTEM

The system used a single point of power meter as shown in Fig.4 and Fig.5. This system consists of energy meter, microcontroller with EEPROM, WIFI module and RTC. Test system can be divided into four parts as follows:

- Monitor Data. Using power meter model RP-96EN that can be installed in single phase system in option RS485 with RTU Modbus protocol. Microcontroller obtained active power reactive power and voltage sampling rate at a 1 Hz from power meter and save data to memory of microcontroller.
- Event Detection. Event detection used 5 points of differencing of active power to detect any change of data. Differencing is part of different equation. If the 5 points of active power are less different than the threshold mean all loads in a steady state. If the data are more different than the threshold means either a change of load that can be expressed as in equation (1).

$$y(m) = \sum_{n=m}^{m+4} \sum_{k=m,k>n}^{m+4} (|x(n) - x(n-k)| < \text{threshold}) \quad (1)$$

when y(m) is status of load of sequent m, if y(m) = 0 that mean loads are steady state and if y > 0 that mean loads are changing. x(n) is sampling input data of sequent n.

- Feature Extractions. When the data are steady state in two close range saves a change of real power (ΔP) add reactive power (ΔQ). This part program in embedded system. It can be mathematically expressed as equation (2)

$$\Delta P = P_{t2} - P_{t1}$$
$$\Delta Q = Q_{t2} - Q_{t1} \quad (2)$$

where ΔP, ΔQ are a change of active and reactive power, P_{t1} is the steady-state active power at time t_1 and P_{t2} is the steady-state active power at time t_2.

- Classification. Using steady-state real power and reactive power (PQ) signatures to data disaggregation. This article interest air conditioner television refrigerator rice cooker and electric iron. The transition of steady-state active power are mapped to a space of P-Q. Used binary calculation to determine status of appliances from the best of distance index. It can be mathematically expressed as equation (3)

$$I_k = \sqrt{(\Delta P - sP_k)^2 + (\Delta Q - sQ_k)^2} \qquad (3)$$

where ΔP is a change of active power, ΔQ is a change of reactive power, sP_k is the sum of active power at index k, sQ_k is the sum of reactive power at index k and I_k is distance of power at index k.

- Display. The Internet of Things (IoT) devices can be used to monitor and control the electrical and mechanical systems. ThingSpeak [11] is the internet of things application platform that selected to use in this paper. User can read data from data base of ThingSpeak.

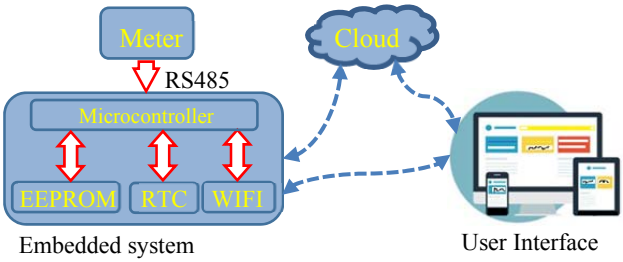

***Fig.4**. Diagram of Test System.*

-

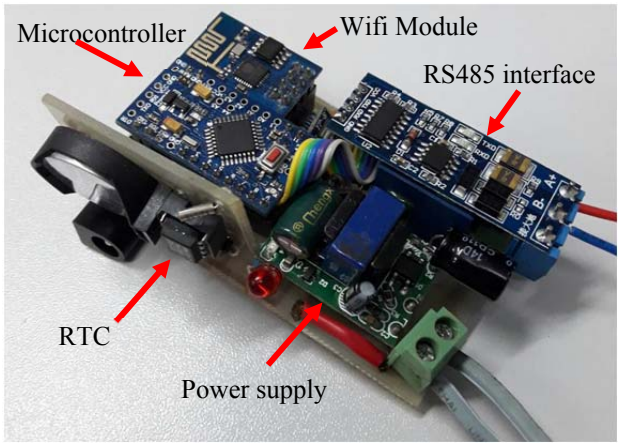

***Fig.5**. NILM Embedded Module*

4. RESULTS

This result was test on October 1-31, 2015. The NILM embedded system has been installed in household and meters has been installed in five loads to compare with NILM algorithm as shown in Fig.6. Fig.7 and Fig.8 are display of energy per month in pie graph and gauge charts on ThingSpeak platform of the IoT that user can read data from this platform via internet.

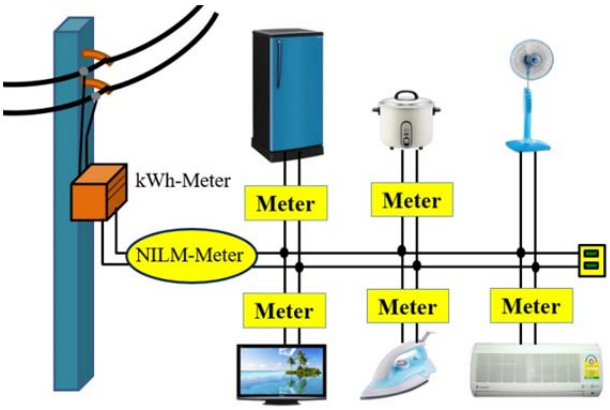

***Fig.6**. Test System*

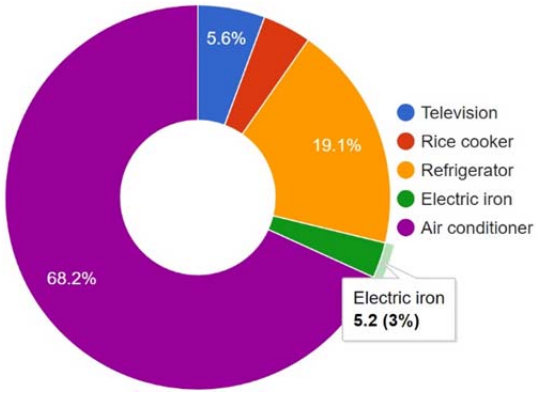

***Fig.7.** Energy ratio from NILM on ThingSpeak platform*

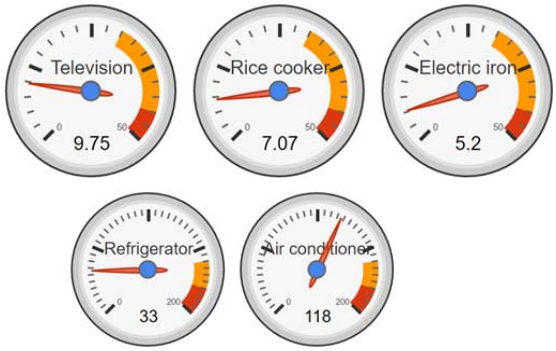

***Fig.8.** Energy gauge from NILM on ThingSpeak platform*

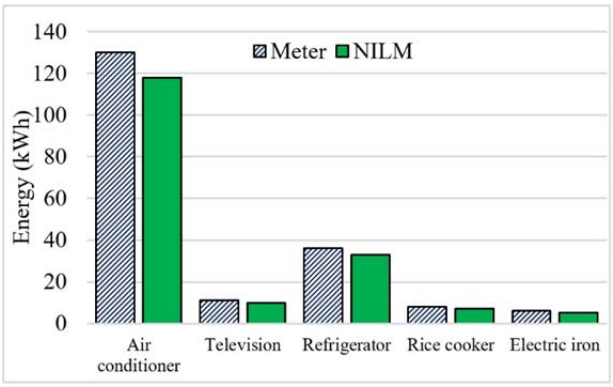

***Fig.9.** Disaggregation of Energy*

Fig.9 shows result of energy profile of loads. The results showed that the proposed system can disaggregation energy of loads in accuracy 89.2% from total consumes energy.

5. CONCLUSION

The paper proposed a design and construction of measuring system to measure the power consumption of loads in household for energy conservation without having to install any instrument directly to appliances. From the results, the system can disaggregate energy of appliances that including air conditioner television refrigerator rice cooker and electric iron from total energy. Test system can disaggregation energy in accuracy 89.2% from total consumes of energy.

REFERENCES

[1] G. W. Hart, "Nonintrusive appliance load monitoring," in Proc. IEEE, vol. 80, no. 12, pp. 1870–1891, Dec. 1992

[2] Hsueh-Hsien Chang, Po-Ching Chien, Lung-Shu Lin, and Nanming Chen, "Feature Extraction of Non-Intrusive Load-Monitoring System Using Genetic Algorithm in Smart Meters,"Eighth IEEE International Conference on e-Business Engineering, pp. 299–304, 2011.

[3] Darby S. The effectiveness of feedback on Energy Consumption. A review for DEFRA of the literature on metering, billing and direct displays, Institute University of Oxford, 2006.

[4] C. Beckel, L. Sadamori, and S. Santini. Automatic socio-economic classi_cation of households using electricity consumption data. In Proceedings of the 4th International Conference on Future Energy Systems (ACM e-Energy '13). Berkeley, CA, USA. ACM, May 2013.

[5] J. M. Abreu, F. Camara Pereira, and P. Ferrao. Using pattern recognition to identify habitual behavior in residential electricity consumption. Energy and buildings, 2012.

[6] J. Z. Kolter and M. J. Johnson. REDD: A public data set for energy disaggregation research. In Workshop on Data Mining Applications in Sustainability (SIGKDD), San Diego, CA, 2011.

[7] S. Biansoongnern and B. Plangklang. Nonintrusive Load Monitoring (NILM) Using an Artificial Neural Network in Embedded System with Low Sampling Rate, in ECTI-CON 2016, Chiang Mai, Thailand. 2016.

[8] S. Gupta, M. S. Reynolds, and S. N. Patel. Electrisense: Single-point sensing using EMI for electrical event detection and classi_cation in the home. In Proceedings of the 12th ACM international conference on Ubiquitous computing, 2010.

[9] Ahmed Zoha et al., "Non-Intrusive Load Monitoring Approaches for Disaggregated Energy Sensing: A Survey," in Sensor 2012.

[10] Mario Bergés, NILM in the era of IoT, the European Non-Intrusive Load Monitoring (NILM) workshop July 2015, London, 2015.

[11] Information on https://thingspeak.com

Performance Test of a Combined Windmill and Wind-turbine Blades Wind Machine

B. Prasartkaew and N. Phuangpornpitak

Manuscript received October, 2016
Revised December, 2016

ABSTRACT

This research aims to design, fabricate and investigate on the performance of a combined windmill and windturbine blades (CWTB) wind machine. As they work on different principles, the wind-turbine works on the principles of lift and drag forces, while the conventional windmill works on the law of conservation of momentum, therefore they serve different purposes and have different advantages. In this research these two kinds of blades were combined to get the new type of windmill with the hypothesis that, for low wind speed location like Thailand, CWTB can be operated at wider range of wind speed with wider range of power output and has the stronger structure. The proposed CWTB has 3 windmill blades and 3 wind-turbine blades with 1.3-m diameter. All blade tips were fixed with outer ring equipped with static brake pads, for reinforcing its structure and protecting the collapse from blade crashing the tower due to strong wind or storm. The test results of the proposed CWTB, in the low speed wind tunnel, demonstrate that at fixed wind speed of 3 m/s, it could start to rotate when the windmill blade angle was adjusted to be 22 degree. The results of performance test using dynamometer show that the maximum torque of 2.94 N-m with the speed of 53 rpm was obtained. The maximum mechanical power of 16.3 kW was achieved. It can be summarized that the proposed WTM can be operated at low wind speed as the average wind speed of Thailand.

Keywords: *low wind speed, wind turbine, windmill, hybrid.*

1. INTRODUCTION

Presently, two major issues which substantially affect on all lives on the earth are the energy crisis and environment problems. Literatures reveal that these serious problems attributed to the combustion of fossil-energy based systems in all energy user sectors [1]. Almost all energy used in Thailand is imported from many countries. In 2015, more than 75% of all energy was fossil based energy [2] and the energy usage trend was continuously increased. To address this issue, exploration of alternative fuel and renewable energy based fuel should be intently promoted. Therefore, one of the best ways to simultaneously address these serious problems is replacing the conventional fossil-energy based systems with the renewableenergy based systems.

Wind energy plays an important role as the promising renewable energy in many countries worldwide. Wind speed are proposed to feasibility assess the potential of wind energy utilization for any location. In the central region of Thailand, which has a high demand for energy in all sectors. The annual mean wind speed is in the low range of 3 to 5 m/s [3].

There are two types of wind machine which extract energy from an air flow and convert it into useful works, windmill and wind-turbine. Where the former is usually used for water pumping and the latter is used for electricity generation. Asshown in Fig. 1, they work on the different principles.

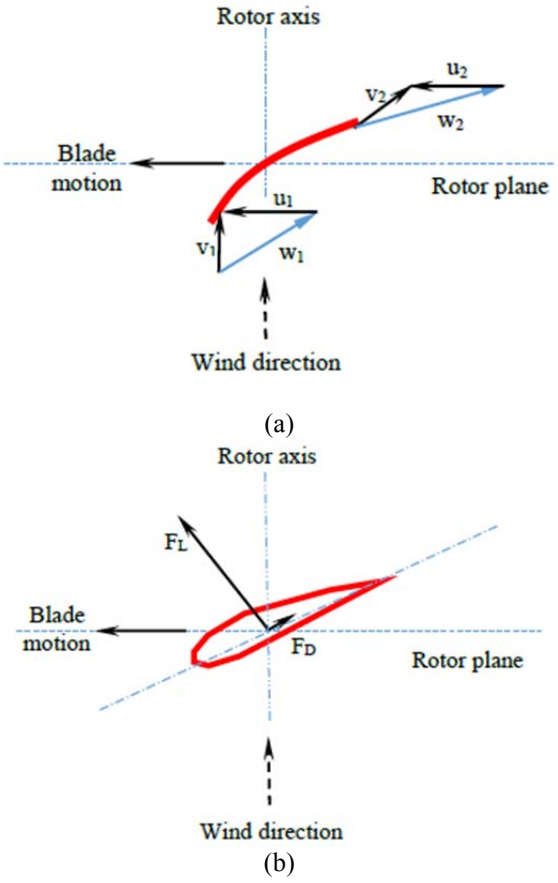

Fig. 1. *Working principles of (a) windmill and (b) wind-turbine*

B. Prasartkaew is with the Faculty of Engineering, Rajamangala University of Technology Thanyaburi, Thailand. Mail: boonrit.p@en.rmutt.ac.th
N. Phuangpornpitak is with the Faculty of Science and Engineering, Kasetsart University Chalermphrakiat Sakonnakhon Province Campus Sakonnakhon, 47000, Thailand E-mail: napaporn.ph@ku.ac.th

Consider the conventional windmill, it works on the law of conservation of momentum as shown in Fig. 1(a), Idealized flow through a windmill: absolute velocity (v), relative velocity (w) and blade velocity (u) at the inlet and exit of the windmill blade section. On the other hand, the wind-turbine works on the principles of lift force (F_L) and drag force (F_D) as shown in Fig. 1(b). Owing to their working principles and structure, herefore they serve different purposes as aforesaid and have different advantages. In the general small wind turbines (usually 1.5 to 3.5m in diameter) require a minimum wind speed of 4 meters per second [4]. Actually, windmill require lower wind speed than wind-turbine. Almost all wind turbines are traditional horizontal axis wind turbines (HAWT) [5,6]. There are many sources of risk for the wind machine failure, many cases of turbine failure were caused by high speed wind or storm. Regarding the safety and endurance of wind machine protecting the collapse from blade crashing or hitting the tower due to strong wind or storm. For a large size wind turbines, to prevent such an accident, they must have two independent fail-safe brake mechanism and to stop the blade revolution. This research aims at to design, fabricate and investigate on the performance of a combined windmill and wind-turbine blades (CWTB) machine for mechanical power generation purpose. In this research these two kinds of blades were combined to get the new type of windmill with the hypothesis that, for low wind speed location like Thailand, CWTB can be operated at wider range of wind speed with wider range of power output and has the stronger structure. In addition, with the stronger structure and a new simple efficient brake system, the proposed wind machine will has more enduring than the conventional one due to it will never collapse because the blade hitting the tower. The objective of this paper is to present the new concept of the proposed wind machine and demonstrate the performance test results.

2. EXPERIMENTAL SET-UP AND METHOD

A. Wind Machine Used in this Study

The proposed wind machine was fabricated and setup for the experimental study Table 1 shows the specification of the CWTB.

TABLE 1. The Specification Of The Proposed Combined Windmill And Wind-Turbine Blades (CWTB) Wind Machi

No.	Item	Specification	Unit
1	Rotor diameter	D = 1.3	m
2	Rotor height	H = 1.5	m
3	Swept area of the rotor	A = 1.33	m^2
4	Outer ring width	R_w = 0.153	m
5	Wind turbine blade length	L_{WT} = 0.55	m
6	Wind-turbine blade width	W_{WT} = 9.5	m
7	Windmill blade profile	as shown in Fig. 3	

The proposed CWTB, as shown in Fig. 2 and 3, has 3 windmill blades and 3 wind-turbine blades with 1.3 -m diameter and. All blade tips were fixed with outer ring equipped with static brake pads (as shown in Fig.3), for reinforcing its structure and protecting the collapse from blade crashing the tower due to strong wind or storm.

(a)

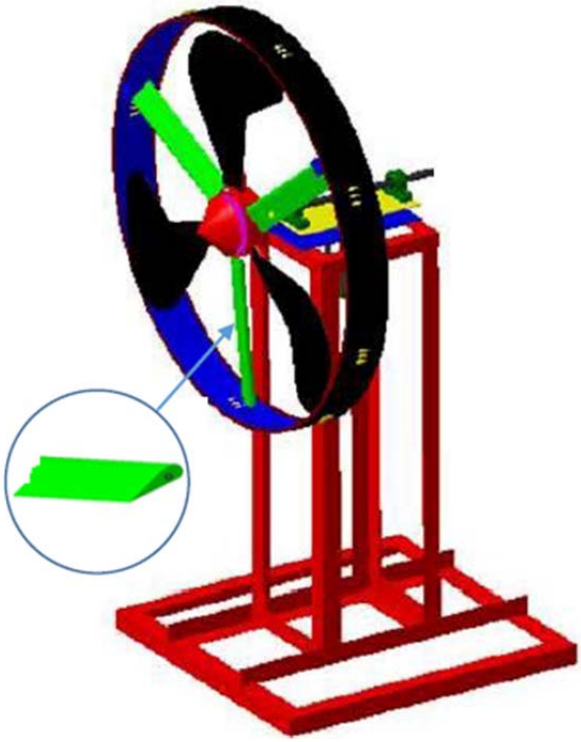

(b)

Fig. 2. *The proposed CWTB used in this study*

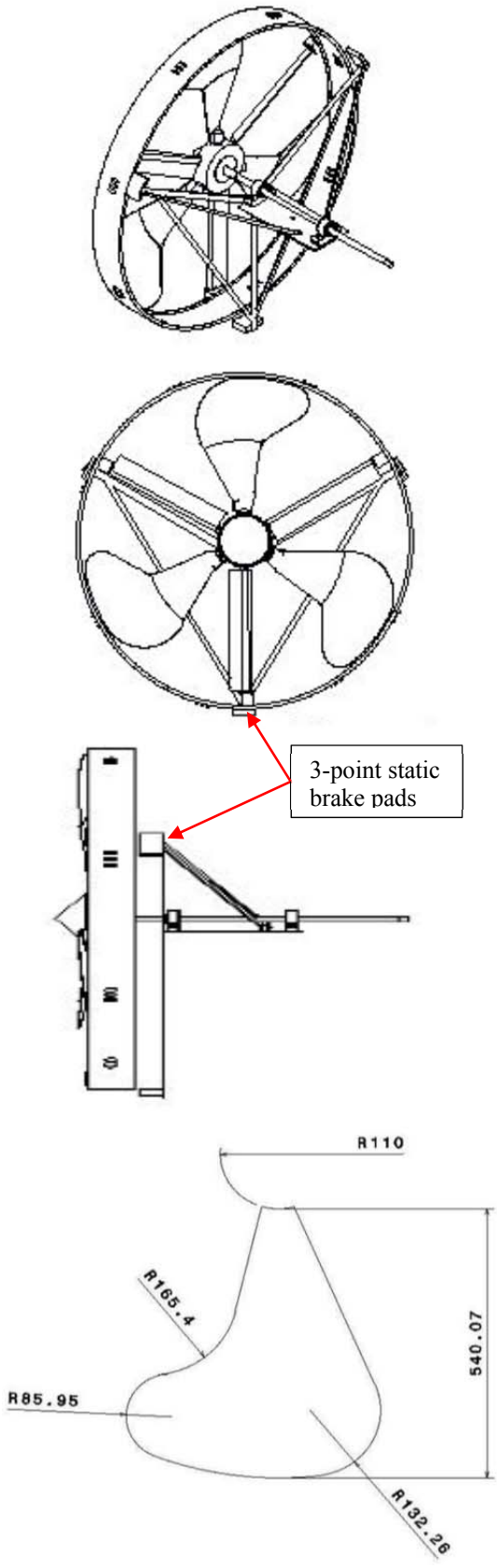

Fig. 3. *The proposed CWTB drawing*

B. Low-wind-speed Wind Tunnel

This research also fabricated a low-cost low-wind-speed wind tunnel (as shown in Fig. 4) for testing the proposed CWTB. This wind tunnel was designed with the design criteria that a) it can be used for a 2-m diameter wind turbine, b) the wind speed in the range of 1 to 5 m/s can be generated and c) it will be fabricated using the materials available in the local markets. The main components comprise of; 1) 5 set of simple 3-propeller fans, 2) a 3.7-kW electrical motor, 5) adjustable 4-speed gear box and 6) honey-comb air flow straightener. With this gear box, the fan speeds of 119, 200, 304 and 423 rpm can be operated and the wind speed of 1.4, 2.3, 3.5 and 5.2 m/s, respectively, was generated (when the CWTB was at the test section). Before the test, the wind speed along with the tunnel radius at the test section was measured; it was found that the wind speed on the cross section area at the test section was uniform.

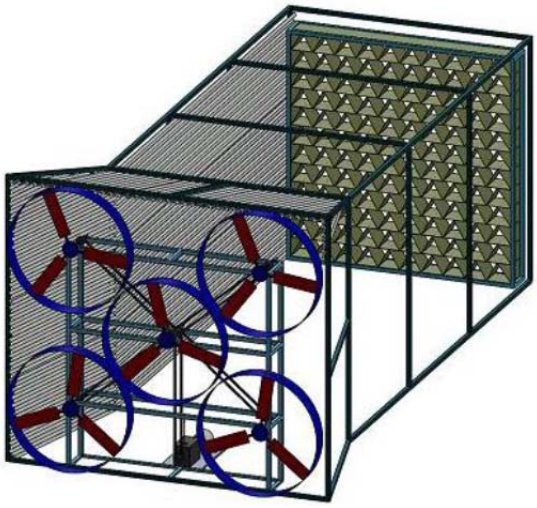

(a)

(b)

Fig. 4. a) *Low-wind-speed wind tunnel and b) The CWTB testing in the wind tunnel*

C. Instrumentations

As aforementioned in the last section that this CWTB wind machine was proposed for the mechanical work tusk. Therefore the important performance index of this machine is mechanical shaft-work output. The layout of experimental setup is shown in Fig. 5. The experimental CWTB were installed in the upper part of the lattice support of 1.5m height. All of instrumentation adjustments were done outside the tunnel and the output data were also monitored and recorded outside the tunnel via online camera. The important instrumentations used in this study is shown in Fig. 6, consist of: a) a small brake dynamometer (Radius of dynamometer rotor = 0.15m), b) tachometer, c) loadcell sensor and monitor and d) anemometer. A small brake dynamometer was connected with the main shaft of CWTB through a rubber coupling. The brake load can be adjusted outside the tunnel via an adjusting rod. A load-cell was used for measure the dynamometer brake force and the measured data can be read outside the tunnel via a digital monitor.

D. Power Calculations

As aforesaid that the independent variable is the mechanical power output generated by the proposed system. There are not only wind speed that affects on this parameter but some of design parameters, e.g.: the physical properties and features of blade and blade pitch angle, also affect on it. Especially for low wind speed location like Thailand and mechanical work task like water pumping for agriculture, the minimum wind speed required for wind machine should be taken into the consideration. Then, in this study, the appropriate blade pitch angle was figured out with the constraint that this machine must be operated as a 'low-wind-speed windmill' with the acceptable power output.

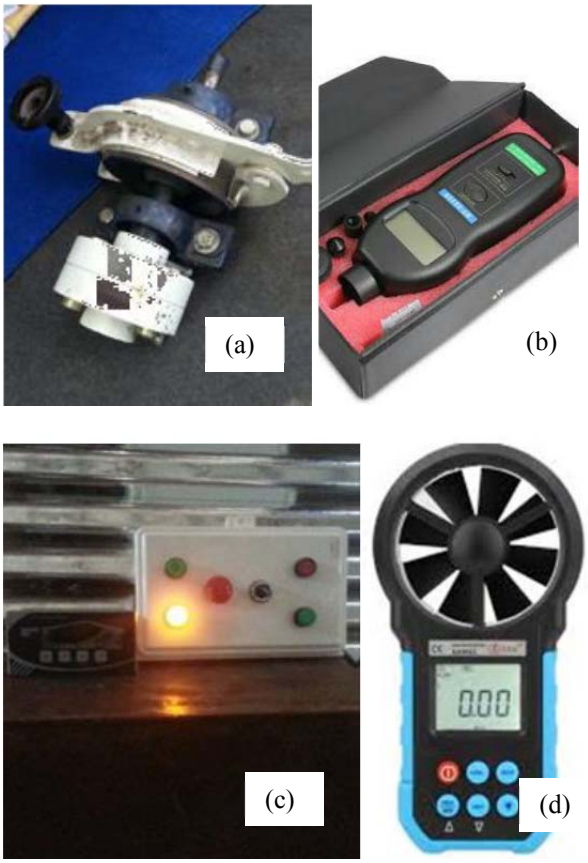

Fig. 6. *The instrumentation used in this study*

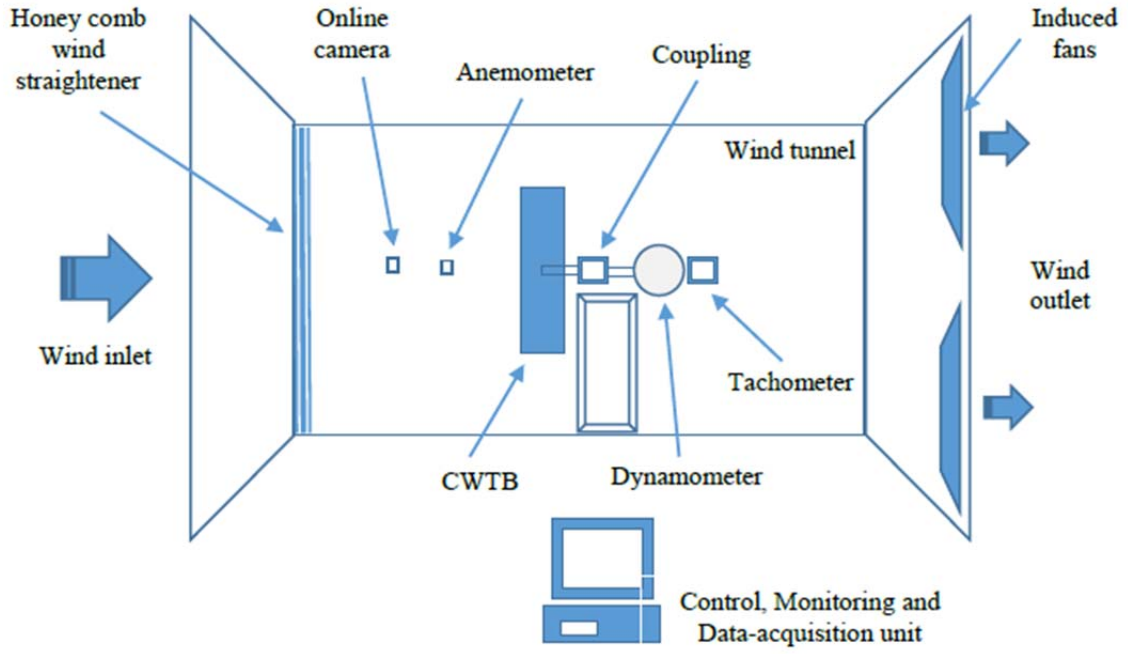

Fig. 5 *Schematic diagram of the experimental setup*

3. PEFROMANCE CALCULATION

A. Torque

Torque of engine was calculated as:

$$T = FR \quad (1)$$

where,

T = Torque (N.m)

F = Tangent force on dynamometer rotor (N)

R = Radius of dynamometer rotor (m)

B. Brake power

Brake power of engine was calculated as:

$$P_b = 2\pi TN / 60 \quad (2)$$

where,

P_b = Brake power (kW)

T = Torque of engine (N.m)

N = Speed of engine (rpm)

C. Theoretical wind turbine power

Theoretically the wind-machine power can be calculated from the wind flow into the swept area using equation [7]:

$$P_{th} = \frac{1}{2}\rho A v^3 c_p \quad (3)$$

where,

Pth = Theoretical wind power (kW)

P = Air density (1.23 kg/m3)

A = Swept area (1.33 m2)

v = Wind speed, m/sec

C_p= Power Coefficient,(maximum value is 1)

4. EXPERIMENTAL RESULTS AND CONSIDERATIONS

As aforesaid that blade pitch angle is one of the most important parameter that substantially affects on the performance of wind machine. In this test, the blade pitch angle was adjusted in many degrees, only some results were shown in this paper. Figure 6 to 8 show the influences of windmill blade pitch angle at 10, 15 and 22 degree, respectively. Where the torque and power output were calculated using equation (1) and (2), respectively. In Fig. 6(c), 7(c) and 8(c), as the maximum value that can be used for identifying the wind machine efficiency, the theoretical wind power at the wind speed of 2.3, 3.5 and 5.2 with the value of 9.95, 35.07 and 115.01 W, respectively.

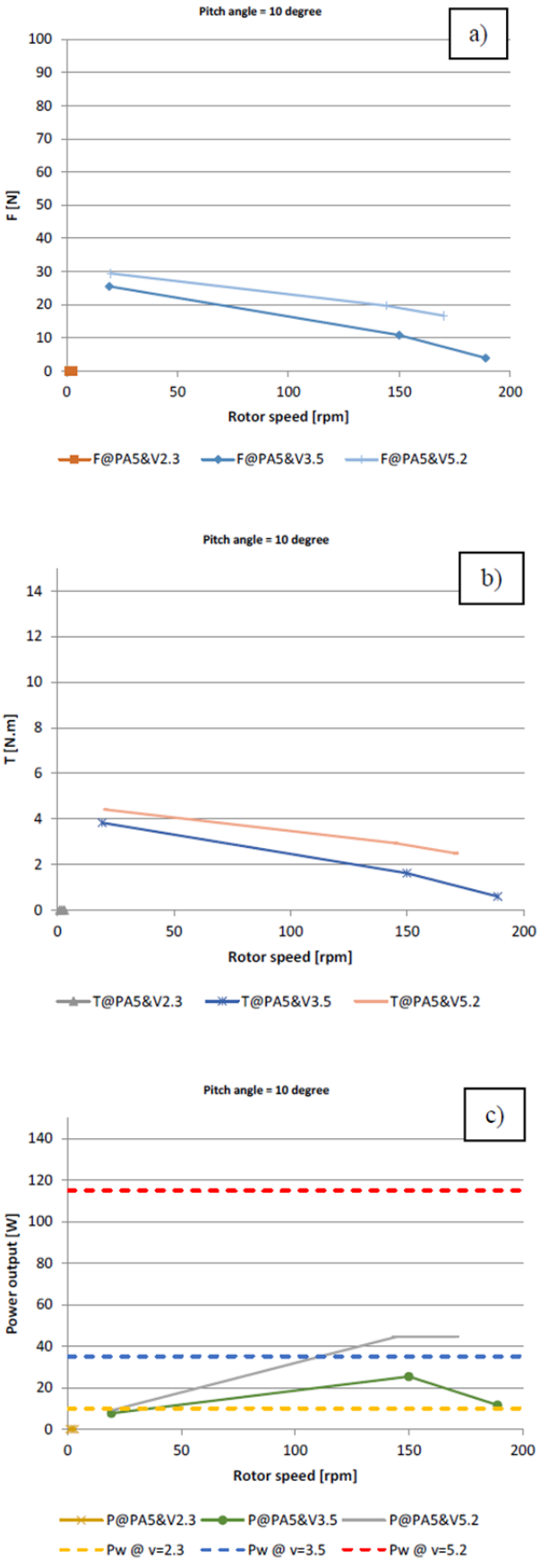

Fig. 6 *Measured data: a) Force on load cell b) Torque and c) Power output, at blade pitch angle of 10 degree*

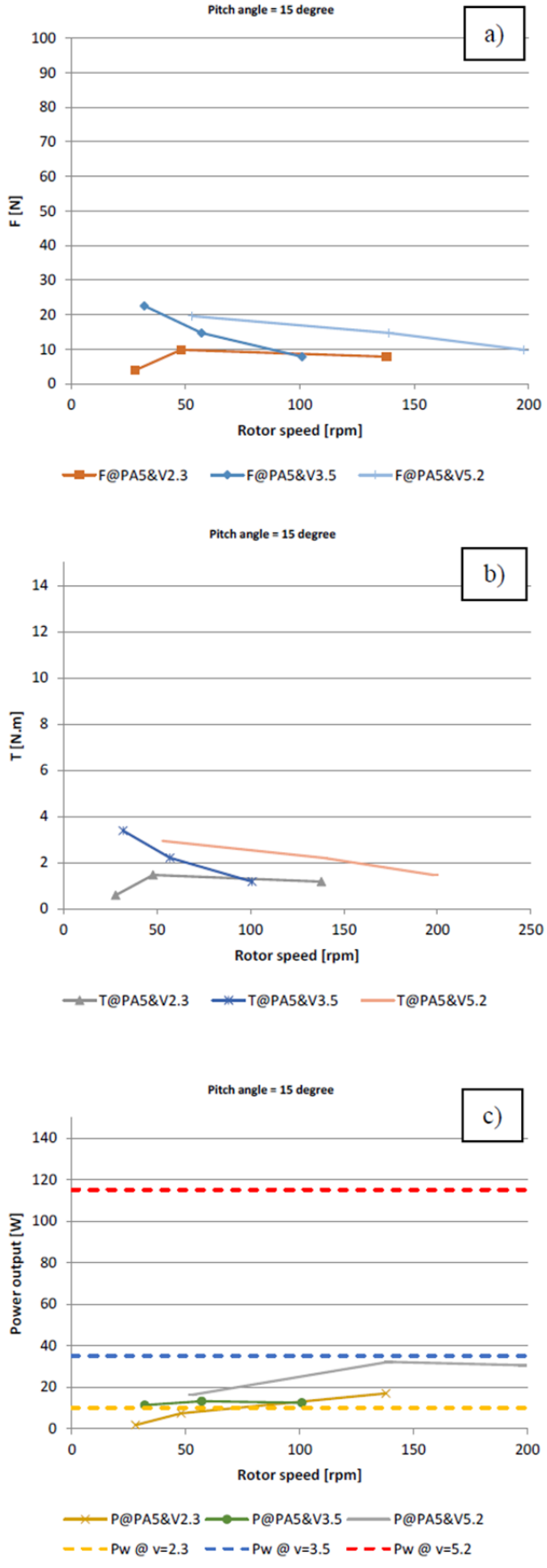

Fig. 7 *Measured data: a) Force on load cell b) Torque and c) Power output, at blade pitch angle of 15 degree*

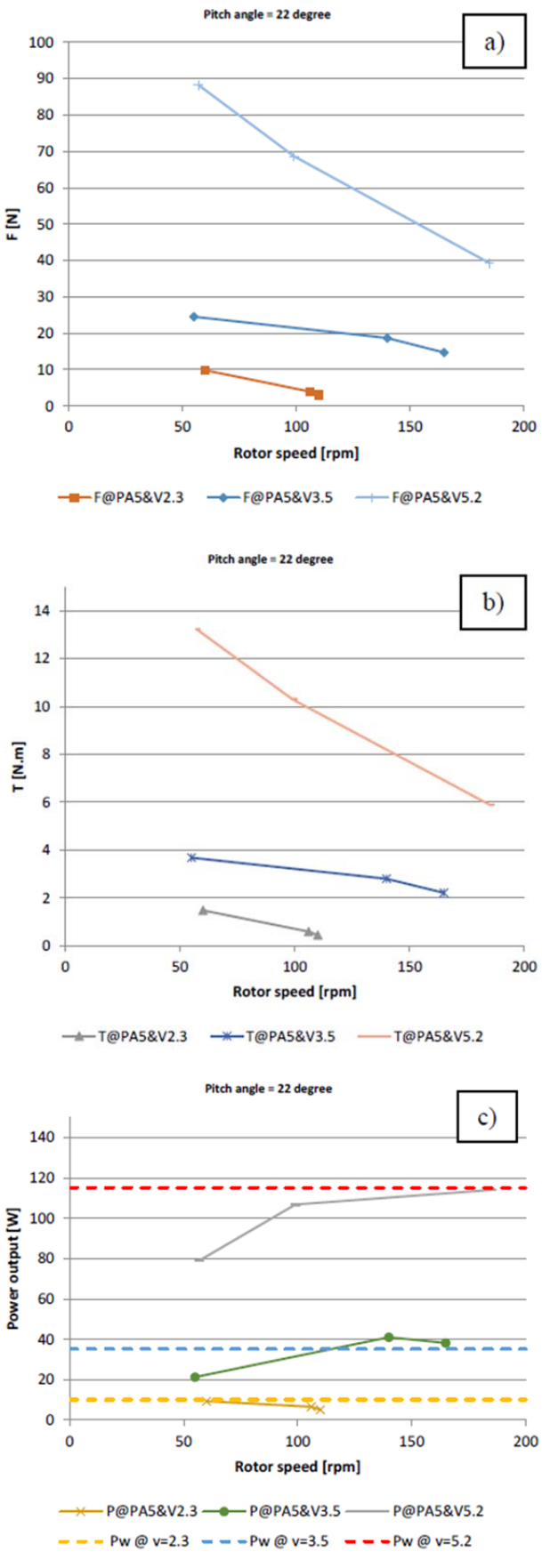

Fig. 8 *Measured data: a) Force on load cell b) Torque and c) Power output, at blade pitch angle of 22 degree*

The experimental results reveal that, at a very low wind speed of 1.4 m/s, the proposed wind machine could not be started for any blade pitch angle. At low wind speed of 2.3 m/s, the proposed wind machine was started when the blade pitch angle was adjusted to be 15 degree. As shown in Fig. 8, the experimental results demonstrate that the proposed wind machine will outperform when the best blade pitch angle of 22 degree. It can be seen that, for low wind speed level (3-5 m/s), the proposed wind machine can generates the mechanical power output very close to the wind power input and have a good trend for higher wind speed, as shown in Fig. 8(c).

5. CONCLUSIONS

The new concept of wind machine was proposed. It has the hybrid blades between windmill and wind-turbine blades, called 'CWTB'. It was proposed for operated under low wind speed condition and has the stronger structure. In addition, CWTB has a new concept of efficient brake for wind machine system then the CWTB will has more enduring than the conventional one owing to it will never collapse because the blade hitting the tower. A 1.3m diameter CWTB was design, fabricated and tested. The test was done inside the constructed 3m low wind speed wind-tunnel. The experimental results demonstrate that CWTB will outperform when the best blade pitch angle of 22 degree. It was found that the power output generated from CWTB is very close to the wind flow power input for low wind speed level and have a good trend for higher wind speed. It can be concluded that the proposed CWTB is promising for the further development as a high efficiency enduring wind machine.

6. ACKNOWLEDGMENT

The authors express their sincere thanks to the Rajamangala University of Technology Thanyaburi (RMUTT) for providing the financial support for his research and publications.

REFERENCES

[1] Boonrit Prasartkaew and S. Kumar, Experimental Study on the Performance of a Solar-Biomass Hybrid Air-Conditioning System. Renewable Energy, Volume 57, September 2013, pp. 86-93.

[2] Thailand Energy Situation 2015 Report, Department of Alternative Energy Development and Efficiency (DEDE), 2016.

[3] Pham Quan and Thananchai Leephakpreeda, Assessment of wind energy potential for selecting wind turbines: An application to Thailand, Sustainable Energy Technologies and Assessments, Volume 11, September 2015, Pages 17–26.

[4] Small Wind Turbine Purchasing Guide. Canadian Wind Energy Association. p. 6. Retrieved 1 March 2016.

[5] Gipe, Paul. Wind energy basics: a guide to home- and community-scale wind energy systems. Chelsea Green Publishing, 2009.

[6] John K. Kaldellis and D. Zafirakis, The wind energy (r)evolution: A short review of a long history, Renewable Energy 36 (2011) 1887-1901.

IEET Editorial Office

EEAAT - Electrical Engineering Academic Association (Thailand)
Room 409, F-Building
140 Cheum-Sampan Rd.
Nong Chok, Bangkok, Thailand 10530
Tel: +662-988-3655 ext 2216 Fax: +662-988-4026

www.journal.eeaat.or.th